Title
Defining the basic principles that govern systemic immune responses in cancer

Author
Allen, Breanna Marie

Publication Date
2020

Peer reviewed|Thesis/dissertation

Defining the basic principles that govern systemic immune responses in cancer

by
Breanna Allen

DISSERTATION
Submitted in partial satisfaction of the requirements for degree of
DOCTOR OF PHILOSOPHY

in

Biomedical Sciences

in the

GRADUATE DIVISION
of the
UNIVERSITY OF CALIFORNIA, SAN FRANCISCO

Approved:

DocuSigned by:
Mary Helen Barcellos-Hoff
32BFD8BC2D194BA...

Mary Helen Barcellos-Hoff
Chair

DocuSigned by:
Lewis Lanier

Lewis Lanier

DocuSigned by:
K. Mark Ansel

K. Mark Ansel

DocuSigned by:
Lawrence Fong

Lawrence Fong

DocuSigned by:
Matthew Spitzer
4793AE6232BE479...

Matthew Spitzer
Committee Members

This dissertation is dedicated to my grandmother,

Ruby Clarissa Allen-Branché

And to my parents,

Trevor M. A. Allen Sr. and Jeannie M. Allen

ACKNOWLEDGEMENTS

First and foremost, I want to thank my inspiration in medicine, my grandmother Ruby who passed away from Alzheimer's after a life dedicated to healing and education. I have always looked up to her poise matched with intelligence, a dominance that was self-assured and not intrusive. She also loved to dance, and I know this achievement is definitely sparking the joy jig. Thank you to my parents, who have always believed in, supported and actively advocated for me. They instilled in me confidence in my own abilities and the importance of both self-discipline and compassion. I would not have achieved this much without that foundation.

Thank you to the family I choose, the incredible humans in my life that constantly build me up while also low-key saving the world. My best friend, soul sister and partner in crime, Taylor Elizabeth Kinney. My decade long friends-turned-family, Lauryann Jiang Hammond, Kyle Moore, and Lennon Chimbumu. My salsa dancing, singing, consulting and graduate experience mentors, Dr. Keyla Badillo, Dr. Fidel Hernandez, and Dr. Andre Esteva. And to the many members of our crazy loving community. Of course, I am grateful for the cuddles and healthy distraction by my feline fur-child, Stella.

The BMS program as a whole has beautifully shaped my experience, so a big thank you to program manager Demian Sainz, the entire BMS office, and my incredible 2016 BMS cohort.

I'd like to thank my scientific collaborators and mentors who helped at the bench side, in shaping ideas, and motivating through failures. I could not have asked for a better scientific partner than Kamir Hiam-Galvez, who's curiosity and eclectic interests have made my thesis experience both engaging and amusing. My Spitzer labmates as a whole for cultivating a culture of collaboration and camaraderie. My thesis committee for the insightful advice in both my science and career, Dr. Lewis Lanier, Dr. Mary Helen Barcellos-Hoff, Dr. Lawrence Fong, and Dr. Mark

Ansel. Each member has gone above and beyond to support me, and I will be forever grateful to have them in my corner. My scientific mentors who helped prepare me for graduate school, Dr. Donald McDonald and Dr. Minah Kim. And to the entire UCSF and ImmunoX communities for cultivating my own scientific mind, and also providing the resources and commitment to drive change for equity and representation in science.

Finally, I'd like to thank my thesis mentor and role model, Dr. Matthew Spitzer. Words cannot accurately express my gratitude to have spent the last 4 years working with Matt. He is of course a brilliant mind with incredible insight in teasing apart systems biology. But more than ability, Matt is the kind of leader that draws the very best from his people. He cares deeply about his team and invests in each of us as humans, not just scientists. I would not have made it through my personal PhD experience without his support. Thank you Matt, for carving opportunity when I saw none. Thank you for being my advocate and champion. I hold immense respect and admiration for you, and I hope to become a leader who is just as kind, thoughtful, and influential.

CONTRIBUTIONS

This dissertation was performed under the supervision of Dr. Matthew Spitzer, PhD. Additional guidance was provided by thesis committee members Dr. Lewis Lanier, PhD, Dr. Mary Helen Barcellos-Hoff, PhD, Dr. Lawrence Fong, MD, PhD, and Dr. Mark Ansel, PhD.

Chapter 1 contains excerpts from a review in preparation: Hiam-Galvez, K.J, Allen, B.M., and Spitzer, M.H. Systemic Immune Responses in Cancer and Therapy. *Nature Medicine.* (2020).

Author contributions: Conceptualization, writing, & editing, all authors; Supervision, M.H.S.

Chapter 2 is reprinted as it appears in: Allen, B.M., Hiam, K.J., Burnett, C.E., Venida, A., DeBarge, R., Tenvooren, I., Marquez, D.M., Cho, N., Carmi, Y., and Spitzer, M.H. Systemic dysfunction and plasticity of the immune macroenvironment in cancer models. *Nature Medicine.* 26, 1125–1134 (2020). https://doi.org/10.1038/s41591-020-0892-6

Author Contributions:

Conceptualization, B.M.A, K.J.H., Y.C., and M.H.S.; Experimental Methodology, B.M.A, K.J.H., C.E.B., A.V., R.D., I.T., D.M.M., N.W.C., Y.C., and M.H.S.; Computational Methodology, B.M.A, and M.H.S.; Investigation, all authors; Writing – Original Draft, B.M.A.; Writing – Review & Editing, all authors; Funding Acquisition, M.H.S.; Supervision, M.H.S.

Acknowledgements:

We thank the UCSF Flow Cytometry Core and Stanley Tamaki for CyTOF maintenance, Drs. Mary Helen Barcellos-Hoff, Ross Levine, Hideho Okada, Edgar Engleman and Jeffrey Bluestone for cell lines, transgenic mice and reagents. We thank Drs. Lewis Lanier, Zena Werb, Mary Helen Barcellos-Hoff, and Lawrence Fong for insightful feedback. This work was supported

by NIH grants DP5OD023056 and P50CA097257 (UCSF Brain Tumor SPORE Developmental Research Program), funds from the UCSF Program for Breakthrough Biomedical Research, and investigator funding from the Parker Institute for Cancer Immunotherapy to M.H.S., and by NIH grant S10OD018040, which enabled procurement of the mass cytometer used in this study.

This study makes use of data generated by NOWAC. A full list of investigators who contributed to the generation of the data is available from http://site.uit.no/nowac/. Funding for the project was provided by the European Research Council grant ERC-2008-AdG 232997. The NOWAC group is not responsible for the analysis or interpretation of the data presented.

Chapter 3 is reprinted as a manuscript in preparation: Allen, B.M., Tenvooren, I., Marquez, D.M., Hiam-Galvez, K.J and Spitzer, M.H. The immune macroenvironment in cancer dictates responses to PD-L1 and CD40 immunotherapies (2020).

Author contributions:

Conceptualization, B.M.A, and M.H.S.; Experimental Methodology, B.M.A, I.T., D.M.M., and K.J.H.; Computational Methodology, B.M.A, and M.H.S.; Investigation, B.M.A, and M.H.S; Writing – B.M.A.; Writing – Review & Editing, B.M.A, and M.H.S; Funding Acquisition, M.H.S.; Supervision, M.H.S.

Acknowledgements:

We thank the UCSF Flow Cytometry Core and Stanley Tamaki for CyTOF maintenance. We thank Dr. Jane Grogan and Genentech for the MC38 cell line, antibody reagents, and feedback on the experimental design. We thank Drs. Lewis Lanier, Mary Helen Barcellos-Hoff, Mark Ansel, and Lawrence Fong for insightful feedback. This work was supported by Genentech, and by NIH grant S10OD018040, which enabled procurement of the mass cytometer used in this study.

Defining the Basic Principles that Govern Systemic Immune Responses in Cancer

Breanna M. Allen

Abstract

Capitalizing on natural immune response capabilities to eradicate cancer holds great promise, but patient reach remains limited due to an incomplete understanding of how to effectively reorient immune responses to reject cancer. We are learning that effective therapeutics drive new systemic immune responses rather than relying on reinvigoration. The present body of work builds a systemic understanding of cancer immunology by defining both local and peripheral immune consequences of tumor development across a wide range of tumor models. This immune macroenvironment in cancer is universally disrupted by tumor burden, with distinct changes across cancer contexts impacted by both cancer cell type and anatomical location. Importantly, tumor disruption of the immune macroenvironment causes functional deficits in *de novo* adaptive immune responses to secondary immune challenges. Successful surgical tumor resection reverses the majority of changes in systemic immunity and restores functional capacity. PD-L1 checkpoint blockade or CD40 agonism immunotherapies can reorient systemic immune responses, but the preexisting immune macroenvironment influences their efficacy and immunological impact. PD-L1 blockade succeeds in cancer settings with preexisting peripheral immune engagement, while CD40 agonism is sufficient to trigger new systemic immune responses that overcome tumor immune evasion. Thus, the immune macroenvironment is a critical, yet underappreciated, differentiator in cancer that can be used to rationally select immunotherapies across patients.

TABLE OF CONTENTS

LIST OF FIGURES

CHAPTER 2

CHAPTER 3

LIST OF TABLES

CHAPTER 2

CHAPTER 3

Chapter 1 Introduction

1.1 Overview

The goal of this thesis was to address a fundamental gap in the field of cancer immunology by asking how cancer reorients the systemic, not just local, immune landscape. The importance of this investigation has been demonstrated in very recent discoveries that: 1) peripheral immunity is essential to productive antitumor immune responses, 2) successful immunotherapies drive new T cell priming and tumor infiltration, and 3) conventional dendritic cells are the pivotal players in orchestrating productive immune responses by immunotherapy. This supports the theory that intentionally driving *de novo* systemic anti-tumor immune responses may be essential to extending currently limited immunotherapeutic efficacy, especially in patients lacking a strong preexisting immune response. But before we can deploy intervention strategies to this end, we must first understand how cancer burden itself may alter systemic immune integrity.

The aims of this thesis were as follows:

1) Determine the consequences of tumor development on systemic immune organization and functional capacity, described in chapter 2.
2) Determine how the altered systemic immune landscape in cancer impacts efficacy and immune responses triggered by PD-L1 blockade or CD40 agonism immunotherapies, described in chapter 3.

1.2 Perturbations to the Immune System during Cancer Development

Cancer development from initial malignant transformation relies on evading a variety of immunosurveillance mechanisms[1,2]. Successful malignant outgrowth not only disengages both innate and adaptive immune arms, but also actually recruits and re-polarizes immune subsets within the tumor microenvironment toward pro-tumorigenic functions. Referred to as tumor-associated macrophages (TAMs), altered myeloid cells in the tumor contribute to angiogenesis, promote cancer cell proliferation and survival, remodel the stroma to exclude cytotoxic immune cells and support malignant dissemination, and engage a variety of immunosuppressive mechanisms to impede adaptive immune responses[3–8]. Local immune remodeling away from tumor-killing and toward tumor support has been extensively characterized, and more recently our understanding has expanded to appreciate the wide heterogeneity in infiltrating immune types and cell states[9,10]. Furthermore, the constant pressure of potential immune eradication also selects for cancer cells with less and less immunogenicity, referred to as immunoediting[11–13].

We are just beginning to appreciate that these tumor-induced alterations for self-preservation extend beyond the tumor microenvironment (TME) into peripheral immune development and function. Various studies have described peripheral disruptions in the development and abundance of specific immune cell types in cancer, with myeloid and neutrophil expansion being the most well-described. Malignancy triggers an early hematopoietic skewing of stem cells in the bone marrow toward the myeloid linages, via cytokines including G-CSF[14,15]. This results in the systemic expansion of a heterogenous pool of immature and immunosuppressive monocytes and neutrophils, often referred to as myeloid-derived suppressor cells, which feed into TAM populations in the TME but also accumulate in peripheral tissues[16–19]. This systemic accumulation of immature immune cells also extends into the dendritic cell compartment.

Conventional dendritic cells (cDCs) are the main antigen-presenters during adaptive immune responses and are instrumental in priming antigen-specific T cell responses to eradicate malignant cells. The cDC compartment is dramatically dysregulated in patients with many cancer types, where abrogated developmental programs in the bone marrow culminate in reduced systemic abundance and maturation[20–27]. These studies show that cDCs in the peripheral blood and tumor draining lymph nodes (dLNs) lack appropriate maturation markers and are less functionally competent in response to classic stimuli, including the toll-like receptor 3 agonist poly (I:C)[21,23]. This fundamental breakdown in systemic antigen-presenting capacity is thought to be a key contributor to cancer outgrowth, with cDC dysfunction developing in the earliest stages of carcinogenesis[26]. Compromised antigen-presenting cell (APC) capacity is complimented by systemic lymphopenia in some cancer patients[28], including a significantly reduced T cell receptor (TCR) repertoire compared to healthy individuals[29]. These studies together tell a story of a fundamentally compromised immune system, which bares direct consequences to the efficacy of attempted immune interventions.

The interplay of the entire system ultimately determines whether the appropriate effector cells are activated, recruited, and supported until complete pathogenic clearance. This process fails during cancer development, and still fails in the majority of cancer patients treated with available immunotherapies. The field lacks a thorough and holistic investigation into how different cancer types disrupt systemic immunity, and how altered composition and functional abilities impact the tumor-burdened immune system's overall capacity for generating new adaptive responses.

1.3 Alterations to Systemic Immunity by Conventional Cancer Therapies

Conventional therapeutic strategies in cancer, including chemotherapy, radiation, and

surgery, perturb the global immune landscape. Understanding these systemic immune consequences is important in design strategies that augment rather than impede antitumor immune responses, which can include optimal timing, dosing, or agent combinations.

1.3.1 Chemotherapy and radiation remodel circulating immune populations.

Chemotherapy and radiation are designed to target cancer cells by compromising cellular integrity during division; however, these agents can also induce a variety of pro-tumorigenic remodeling of immunity that impede overall treatment efficacy. Immune consequences of conventional cancer therapies was reviewed in Shaked *et al.* 2019, and includes expansion of immunosuppressive myeloid cells via elevated pro-inflammatory cytokines, such as IL-6, IL-8, and GM-CSF, and B cell release of systemic extracellular vesicles that impede anti-tumor cytotoxic immune functions[30]. One counterstrategy is to pair these therapies with agents that block immunosuppressive phenotypes, such as inhibiting CSF1R or CCR2. Chemotherapeutic cytotoxicity also leads to general lymphodepletion, and while $CD8^+$ T cells fully recover within a year, an abnormal bias of $CD4^+$ T cell memory toward inflammatory effectors persists for years in breast cancer patients[31]. Selecting agents that mitigate specific immune abnormalities would be optimal for generating the strongest antitumor effect.

The immune impact of chemo- and radiotherapy depends highly on context, making it challenging but imperative to understand how each cytotoxic therapy may compromise immune function across cancer settings. In non-small cell lung cancer, standard fractionated radiotherapy but not chemotherapy leads to myeloid cell expansion, reduced APC function, and impaired T cell responses[32]. Similar immune impacts were observed after combination chemo- and radiotherapy in cervical cancer patients[33]. Neoadjuvant chemotherapy prior to surgical resection is a strategy often used in breast cancer, but patients show disparate immune effects depending on cancer stage

and therapeutic agent. In non-metastatic breast cancer patients, doxorubicin and cyclophosphamide chemotherapy led to elevated systemic granulocytic myeloid derived suppressor cells (MDSCs) and no changes in monocytic MDSCs[34]. However, in metastatic breast cancer patients treated with FEC (5-fluorouracil [5-FU], epirubicin, cyclophosphamide) or docetaxel chemotherapies, monocytic MDSCs were dramatically reduced in six out of ten patients[35]. In Her2 receptor positive ($Her2^+$) breast cancer patients specifically, a recent study suggests that higher circulating IL-10 and classical monocytes associates with reduced pathological complete responses after chemotherapy[36]. Future work is needed to parse how disease type and stage affect the immune consequences of cytotoxic therapies.

When demonstrably effective, chemotherapy augments systemic antitumor immunity in conjunction with disrupting cancer cell division. Recent work showed that effective responses to pre-surgical neoadjuvant chemotherapy in triple-negative breast cancer (TNBC) induces the recruitment of new T cell clones to the tumor microenvironment, rather than expanding those already present[37]. Importantly, different subtypes of breast cancer showed differential immune responses to this therapeutic strategy, reflected in the functionality of peripheral $CD8^+$ T cells. Estrogen receptor positive (ER^+) patients had a drop or stasis in the polyfunctionality of circulating $PD1^+$ $CD8^+$ T cells, measured by cytokine production after TCR stimulation. Estrogen and Her2 receptor positive (ER^+Her2^+) patients showed a complete loss of functionality in this subset. TNBC patients, conversely, showed elevated $PD1^+$ $CD8^+$ T cells with high functionality, producing effector cytokines including granzyme B, IFNγ and TNFα, and evidence of clonal expansion. Ultimately, tumor-infiltrating T cells were only prognostic for overall survival in TNBC. They also found that a cytolytic, but exhausted, $CD8^+$ T cell signature in the blood of TNBC patients following chemotherapy was evident of ongoing disease, and predictive of recurrence or metastasis

post-surgery.

With the advent of immunotherapy, our strategies are shifting toward using toxic therapeutic agents to augment anti-tumor immunity via disrupting the tumor stroma or releasing tumor antigens for new adaptive immune activation[38–40].

1.3.2 Tumor resection can disrupt immunological control of metastasis.

We are gaining a deeper understanding of the impact of surgical tumor resection on the systemic immune state and immunological control of dormant metastases. Surgical acceleration of metastasis has been documented in several cancer types, where previously controlled micro-metastases regained aggressive proliferation following resection of the primary tumor[41]. Several recent studies implicate myeloid immune cell remodeling induced by systemic wound healing programs. Resection, or wounding independent of primary tumor removal, triggers healing programs that elevate circulating IL-6, G-CSF, and CCL2 and ultimately drive myeloid subsets toward immunosuppressive states[42]. While resection massively reduces systemic MDSCs in the 4T1 breast cancer model, functional immunosuppressive granulocytic MDSCs can persist in the spleen, blood, primary tumor dLNs, and the lung for 2 weeks[43]. Persistent immunosuppressive myeloid cells were shown to support pro-tumorigenic niches in the lungs in both breast cancer and osteosarcoma models[43,44]. Depleting myeloid subsets can prevent post-surgical metastases, including adjuvant gemcitabine chemotherapeutic depletion of granulocytic MDSCs, or gefitinib, a receptor interacting protein kinase 2 inhibitor that promotes inflammatory macrophage states. Appropriate pairing of conventional therapies with immune modulation can be a powerful tool to dislodge cancer but should be based on and reactive to the systemic immune context.

1.4 Systemic Immune Responses in Cancer Immunotherapy

Cancer immunotherapy has radically expanded our toolkit against cancer, with current FDA approval of 7 checkpoint inhibitors (CPIs) across 19 different cancer types, in addition to chimeric antigen receptor T-cell (CAR-T cell) and bispecific T-cell engager (BiTE) therapies, and vaccines. Using the immune system to kill cancer centered around the notion of de-restricting cytotoxic effectors within the tumor microenvironment, but appreciation is growing in the field for the fundamentally systemic nature of effective antitumor immunity. Recent studies demonstrate that CPIs, including blockade of the PD-1/PD-L1 axis, rely on systemic immune mechanisms during effective antitumor responses. Moreover, adaptive immune responses that include new T cell priming by cDCs, referred to as *de novo* responses, are required to achieve therapeutic impact.

1.4.1 Intact peripheral immunity is critical to immunotherapeutic efficacy.

Intact peripheral immune function, communication and trafficking are required for CPI efficacy. Disruption of peripheral immune integrity by systemic chemotherapy can impede therapeutic benefit by PD-1 blockade, causing systemic lymphodepletion and abrogating long-term immune memory[45]. Local chemotherapy spares peripheral immunity, collaborating with PD-1 blockade to induce DC infiltration into the tumor and clonal expansion of antigen-specific effector T cells. Further evidence of continuous systemic reliance, blockade of lymphocyte egress from lymphoid organs or surgical resection of tumor dLNs abrogates immunotherapeutic efficacy[46,47]. The eradication of systemic disease also heavily relies on global immune responses. Strong adaptive immune responses confer peripheral memory, where the transfer of T cells from secondary lymphoid organs (including the spleen, lymph node, and blood) after productive antitumor responses is sufficient to protect naïve animals[48]. This same study showed that systemic

PD-L1 blockade can break tolerance of distant tumors when paired with local therapeutic delivery at one site.

It is clear that inhibiting the PD-1/PD-L1 axis extends beyond removing local immunosuppressive cues, and recent work has clarified key peripheral immune cells driving responses in these settings. First, therapeutic benefit of checkpoint inhibition is only observed in models with intact host PD-1/PD-L1 expression, and is less dependent on cancer cell expression of PD-L1[49–51]. The main non-tumor expressors of PD-L1 are antigen-presenting cells, including macrophages but most highly on cDCs. In melanoma patients, intratumoral macrophage and cDC PD-L1 expression levels correlate with clinical complete responses to anti-PD-L1 and anti-CTLA-4 combination therapy. Moreover, several groups have recently demonstrated that DCs are the critical mediator of PD-L1 blockade efficacy[52,53]. Targeted depletion of PD-L1 in cDCs, but not macrophages, greatly reduced $CD8^+$ T cell responses and tumor shrinkage with PD-L1 blockade in the subcutaneous MC38 cancer model[52]. The critical location for this interaction appears to be the dLNs. Tumor specific PD-1^+ T cells in the dLN showed high co-localization with PD-L1 expressing cDCs. Low-dose selective targeting of PD-L1 engagement in the dLNs was sufficient to induce effective anti-tumor responses in two syngeneic models, albeit to a lesser extent than systemic PD-L1 blockade[53]. Interactions between PD-$L1^+$ cDCs and PD-1^+ T cells in dLNs is also indicative of disease dissemination status in melanoma patients. Frequent dLN PD-1/PD-L1-interactions observed in metastatic melanoma patients were predictive of early disseminated disease recurrence in non-metastatic patients[53]. Augmenting T cell effector and memory development in the dLN via mitochondrial activation further improves PD-1 blockade efficacy[54], highlighting the need to optimize systemic immune engagement for tumor eradication.

1.4.2 Effective immunotherapies drive *de novo* immune responses.

Productive antitumor responses ultimately necessitate functional effector T cells within the TME to mediate cancer cell killing. However, recent studies revealed that intratumoral T cells acquire terminally exhausted states over time rendering them incapable of reinvigoration. Preclinical and patient assessments of $CD8^+$ T cell epigenetic landscapes showed that intratumoral T cells undergo massive chromatin remodeling locking in dysfunctional states, with lost ability to produce TNFα and IFNγ[55]. This process was biphasic in preclinical models, where early T cell remodeling was reversible upon removal from the tumor context, but a second wave of epigenetic remodeling led to irrecoverable dysfunction marked by CD101 and CD38 co-expression. Additional studies have identified the TOX transcription factor as a critical regulator in exhaustion transcriptional and epigenetic reprograming in response to chronic T cell stimulation[56,57]. Microenvironmental stressors in the TME complement chronic stimulation and checkpoint receptor signaling to drive T cell dysfunction. A study recently showed that metabolic challenges within the tumor cause T cells to accumulate structurally damaged mitochondria with high reactive oxygen species and overall compromised membrane potential[58]. Importantly, mitochondrial dysregulation was sufficient to induce epigenetic reprogramming toward terminal dysfunction and was not observed in peripheral T cells from the spleen or dLN. Clinical responses to CPIs associate with the presence of a second, stem-like $CD8^+$ T cell state with reduced co-inhibitory molecules and elevated memory, activation, and cell survival transcriptional and epigenetic programs[59]. These productive intratumoral $CD8^+$ T cells can be identified by expression of transcription factor TCF-1, important for for WNT signaling in stem cell-like memory programs, and notable lack of CD39 and TIM3. Thus, immunotherapies rely on the quality of effector $CD8^+$ T cells within the TME, but persistence in this toxic microenvironment rapidly drives dysfunction.

To overcome local immune dysfunction, effective immunotherapies drive *de novo* peripheral immune responses culminating in new effector T cell infiltration. Several reports have now shown that PD-1 and PD-L1 blockade drive novel T cell clones into the tumor that were not present locally prior to therapy[60,6162]. In basal cell carcinoma, 68% of all intratumoral clones after PD-1 blockade were novel, 84% of which displayed exhaustion markers indicative of high activation and represented novel TCR specificity groups suggesting new antigen targets. Further, 35.5% of these novel clones were also detected in the blood, whereas only 11.8% were detected in circulation pre-treatment. Non-functionally exhausted clones in the tumor were more likely to be blood-associated and expanded compared to non-blood associated clones after treatment. Correlation between blood and tumor clones was also demonstrated in metastatic melanoma, renal, lung, and colon cancers[61,62]. Cell-intrinsic CD28 signaling in $CD8^+$ T cells is critical in PD-1 blockade efficacy[63], providing necessary costimulation in naïve T cell priming. Impressively, in classical Hodgkin lymphoma, the peripheral T cell clonal diversity at baseline was associated with PD-1 blockade efficacy, illustrating how individual systemic immune contexts dictate the impact of immunotherapeutic intervention[29]. This signature was complimented by greater expansion of singleton clones in the blood in patients with complete response, likely representing peripheral T cells that had not encountered antigen pre-treatment. This cancer context was more reliant on $CD4^+$ T cells, with expanded $CD4^+$ T cell TCR diversity, and concordant associations with circulating B cell abundance and a novel innate effector population capable of antibody-dependent cellular cytotoxicity. Together, these results strongly support not only the involvement of peripheral immunity in renewed antitumor responses, but also *de novo* priming of additional naïve T cell subsets rather than the classically held theory of reinvigorating existing responses.

Intentional strategies for driving *de novo* immune responses are gaining traction in clinical

trials, including stimulation of DC activity through agonistic CD40 antibodies[64,65]. The field has demonstrated that checkpoint blockade relies on derestricting cDCs to allow for effective T cell priming, but this strategy fails in cases where there is a poor or absent preexisting activation of APCs. Pancreatic cancer is resistant to CPI, but preclinical models demonstrate that combination with CD40 agonism can produce complete tumor regression and extend survival independent of TLR, STING, or IFNAR signaling[66]. Efficacy was dependent on host Batf3 and CD40, as well as effector $CD4^+$and $CD8^+$ T cells that were massively expanded in the blood and dLN. An early clinical trial in metastatic pancreatic cancer patients shows over a 50% objective response rate to the combination of CD40 agonism with PD-1 blockade and gemcitabine and nab-paclitaxel chemotherapy[67]. CD40 activation is just one strategy to intentionally drive *de novo* antitumor immune responses, particularly critical in converting immunologically "cold" tumor contexts into "hot" immune involvement.

As the field moves towards a systemic perspective on antitumor immune responses, comprehensive examinations of the tumor-burdened systemic immune state become essential. To that end, the present body of work investigates changes in systemic immune organization and function in cancer, and the direct consequence on mechanisms and efficacies of immunotherapies. The working hypothesis is that successful immunotherapies drive new T cell priming by cDCs in the dLNs leading to activated T cell accumulation in the periphery, infiltration into the tumor, and eventual tumor eradication. Checkpoint blockade achieves this by removing a negative signal between cDCs and naïve T cells, promoting interaction, while CD40 agonism massively increases cDC activation and thereby total priming capacity. We hope that these studies will ultimately lead to therapeutic strategies that drive *de novo* antitumor immune responses based on the present systemic immune state in each patient.

Chapter 2 Systemic dysfunction and plasticity of the immune macroenvironment in cancer models

Breanna M. Allen[1,2,6], Kamir J. Hiam[1,2,6], Cassandra E. Burnett[1,2], Anthony Venida[1,3], Rachel DeBarge[1,2], Iliana Tenvooren[2], Diana M. Marquez[2], Nam Woo Cho[2,4], Yaron Carmi[5], and Matthew H. Spitzer[1,2]*

[1]Graduate Program in Biomedical Sciences, University of California, San Francisco, San Francisco, CA, USA

[2]Departments of Otolaryngology and Microbiology & Immunology, Helen Diller Family Comprehensive Cancer Center, Parker Institute for Cancer Immunotherapy, Chan Zuckerberg Biohub, University of California, San Francisco, San Francisco, CA, USA

[3]Department of Anatomy, University of California, San Francisco, San Francisco, CA, USA

[4]Department of Radiation Oncology, University of California San Francisco, San Francisco, CA, USA

[5]Department of Pathology, Sackler School of Medicine, Tel Aviv University, Tel Aviv, Israel.

[6]Co-First Author

*Corresponding author

2.1 Abstract

Our understanding of the factors governing immune responses in cancer remains incomplete, limiting patient benefit. Here, we use mass cytometry to define the systemic immune landscape in response to tumor development across five tissues in eight mouse tumor models. Systemic immunity was dramatically altered across models and time, with consistent findings in the peripheral blood of breast cancer patients. Changes in peripheral tissues differed from those in the tumor microenvironment. Mice with tumor-experienced immune systems mounted dampened responses to orthogonal challenges, including reduced T cell activation during viral or bacterial infection. Antigen-presenting cells (APCs) mounted weaker responses in this context, while promoting APC activation rescued T cell activity. Systemic immune changes were reversed with surgical tumor resection, and many were prevented by IL-1 or G-CSF blockade, revealing remarkable plasticity in the systemic immune state. These results demonstrate that tumor development dynamically reshapes the composition and function of the immune macroenvironment.

2.2 Introduction

Immunotherapy has rapidly expanded our toolkit against cancer, but a broader understanding of factors governing immune responses in cancer is required to extend clinical efficacy to all patients. Intratumoral $CD8^+$ T cells have been the main focus of cancer immunotherapies, yet recent studies demonstrate that cytotoxic T cells within the TME are irreversibly dysfunctional[55]. Several studies have shown that a systemic anti-tumor immune response is essential for immunotherapeutic efficacy[45,46,50,54,60,68–70]. However, we lack a comprehensive definition of how cancer development impacts the systemic immune state.

Several lines of evidence suggest that systemic immune perturbations occur with cancer. Peripheral granulocytic and monocytic expansion and impaired differentiation accompany tumor progression[14,71,72] along with a reduction in conventional dendritic cells[20]. Systemic effects on lymphocytes remain poorly understood. Most studies have explored anti-tumor immune responses at a single, static time point, leaving the dynamicity of the immune system during cancer development an open question. Prior immune experiences can impact responses to new stimuli by shifting basal cytokine levels, innate immune activation states, and cellular composition[73–75]. While many immunotherapies and vaccines seek to elicit new immune responses in cancer patients, it remains uncertain how tumor burden impacts these processes. It is also unclear whether there are lasting immune impacts after successful primary tumor clearance, though studies have associated tumor resection with a reduction in myeloid-derived suppressor cells[76,77]. Defining the functional capacity and stability of the tumor-experienced immune macroenvironment is critical for improving immunotherapies.

We used high content single-cell analysis and corresponding analytical methods to characterize the systemic immune landscape across eight commonly used mouse tumor models. These data,

which are publicly available, provide a rich resource. While each tumor has unique immunological consequences, we found that three distinct breast cancer models converged on similar systemic changes. Tumors drove dynamic shifts in the organization and functional capacity of immune cells across the organism, culminating in attenuated responses to new immune challenges, while tumor resection was sufficient to revert the systemic immune landscape. These findings have implications for how and when we apply immunomodulatory agents in cancer, emphasizing the importance of strategies that are informed by preexisting alterations in the immune macroenvironment.

2.3 Results

2.3.1 Systemic immune organization is altered across multiple tumor types

We began by examining the TME across several common mouse tumor models, including genetically-engineered and transplantable syngeneic models across different mouse strains with different mutational loads, metastatic potential, variability and latency in tumor growth[78–81]. We characterized well-established, but pre-terminal tumor stages to reflect the patient populations most often treated with immunotherapies, but also to avoid the confounding impact of end-of-life processes. We utilized mass cytometry to quantify the abundance and activity state of immune cell subsets in the tumor as well as the blood, spleen, bone marrow and tumor-draining lymph nodes (dLNs) (Table 2.1and Figure 2.1).

The immune composition of the TME was distinct between models, varying in the degree of immune infiltration and diversity (Figure 2.2a and Figure 2.3). The predominant immune cell types were tumor-associated macrophages and other CD11b^{high} myeloid subsets, particularly in the transplantable MC38 colorectal cancer and SB28 glioblastoma models, with relatively fewer

adaptive immune cells as reported in many human tumors[82]. Both transplantable LMP pancreatic cancer and genetically induced Braf˙Pten melanoma models showed extensive eosinophil infiltration. B16-F10 syngeneic melanoma and three models of breast cancer (transplantable cell lines 4T1 and AT3 and autochthonous MMTV-PyMT) showed less relative abundance but greater diversity in local immune cells, including B, T, and NK cell infiltration (Figure 2.2a and Figure 2.3a). Unique immune profiles were apparent across tumor types (Figure 2.2b and Figure 2.3g).

We next asked whether these tumor models also resulted in altered systemic immune states. The immune compositions of the tumor dLN, bone marrow, blood, and spleen were indeed altered, with nuance in the extent of alteration and immune cell types affected (Figure 2.2c and Figure 2.3g). There was striking concordance among different models of the same tumor type (breast cancer and melanoma), shifting together across principal components. Surprisingly, SB28 glioblastoma extensively altered systemic immunity despite localization in the brain. Reporter protein expression was not responsible for systemic immune remodeling, as both the AT3 parental cell line and a derivative expressing GFP and luciferase exhibited strongly correlated systemic alterations (Figure 2.3h, $r = 0.9$, $p = 2.2e\text{-}16$). Systemic alterations also occurred in mice both with and without metastases (Figure 2.4a-e) and were tightly correlated with primary tumor size in the MMTV-PyMT model ($r = 0.8527$, $p < 0.0001$). While the majority of systemic immune remodeling could be explained by primary tumor size (78.4%), the residual values were correlated with both lung and lymph node metastases ($r = 0.5794$, $p = 0.0207$ for lung, and $r = 0.5882$, $p = 0.0185$ for lymph node). Compositional alterations in these peripheral sites did not correspond with the local immune infiltrate. Thus, tumor burden drives distinct changes in peripheral immune organization, dependent on the identity of the tumor.

We next performed Statistical Scaffold Analysis[46,83] to interrogate the impact of tumor

burden in a more detailed manner, focusing initially on the spleen as a secondary lymphoid organ distal from the tumor (Figure 2.2d and Figure 2.3b-f, Methods). All models exhibited expansions in the splenic myeloid compartment, which was dominant in some, such as the three breast cancer models (Figure 2.2d and

Table 2.2) but less dramatic in others, such as the two melanoma models (Figure 2.3e-f). Splenic remodeling in breast cancer was specifically characterized by increases in frequencies of neutrophils, eosinophils, and monocytes and reductions in B and T cells (Figure 2.2d). Consistency was observed across breast cancer models, which span three mouse strain backgrounds (BALB/c for 4T1, C57BL/6 for AT3, and FVB/N for MMTV-PyMT), orthotopic and autochthonous models, and a range of metastatic potential (AT3 – weakly metastatic, MMTV-PyMT – moderately metastatic, 4T1 – highly metastatic). Consistency despite model differences argues for a tumor and/or site-specific bias in systemic immune responses. Gene expression analysis of whole blood from untreated breast cancer patients and matched controls from the Norwegian Women and Cancer Study also demonstrated a marked shift in the immune state (PC1 Wilcoxon rank-sum p-value = 5.0×10^{-12}, PC2 p-value = 1.6×10^{-6}) (Figure 2.2e). Cellular enrichment analysis demonstrated increased neutrophils and decreased Th1 and $CD8^+$ T cells (Figure 2.2f). Altogether, these data suggest that tumor burden broadly disrupts immune macroenvironments, providing context to inform therapeutic manipulations designed to activate local versus systemic responses.

2.3.2 Tumor growth drives non-linear changes in immune cell frequencies over time

Tumors develop gradually, yet tumors are sampled at one developmental point in the clinic to provide prognostic information related to the immune response. We explored the dynamics of global immune remodeling during breast tumor growth, beginning with the predictable orthotopic

4T1 model before confirming results in an unrelated spontaneous model (MMTV-PyMT). Absolute cell counts of tumor-infiltrating leukocytes positively correlated with tumor size, supporting a progressive immune response (Figure 2.4f, $r = 0.6$, $p = 0.0256$). Absolute spleen cell counts also increased, but cell frequencies as a percent of total leukocytes were comparable to absolute numbers per milligram of spleen (Figure 2.4g). Deep profiling of both the tumor and splenic immune compositions by mass cytometry revealed nonparametric correlations in individual cluster frequencies with time (Figure 2.5a-b), demonstrating at the single cell level that immune changes are indeed progressive. PCA of immune cell frequencies showed progressive changes across tissues over tumor growth in both 4T1 (Figure 2.5c-d) and MMTV-PyMT tumors (Figure 2.4h). Importantly, the immune profile within the TME remained distinct from those observed in peripheral sites. The dLN immune composition was unique, while the spleen, blood, and bone marrow were more coordinated. Neutrophil expansion in the spleen and bone marrow, culminating in elevated circulation in blood, but lack of accumulation within the lymph node or tumor, is one feature contributing to these unique profiles (Figure 2.5d).

Progressive systemic immune responses to tumor burden were not strictly linear. The magnitude of change was non-uniform between each time point as evident by the PCA (Figure 2.5c and Figure 2.4h). While some population changes were relatively continuous, such as increasing neutrophils or decreasing $CD4^+$ T cells, many others were dynamic, like $CD8^+$ T cells and Tregs, which reciprocally expanded and contracted at distinct times in the tumor and dLN (Figure 2.5d). In the spleen, myeloid expansion began by day 7 and continued to day 14, preceding the progressive decline in the T and B cells that began by day 14 (Figure 2.4i). The lymph node also changed most dramatically by day 14 (Figure 2.6a), while changes in blood were more continuous (Figure 2.6b). The bone marrow and tumor contained less mature and clearly defined

cell types, with many more inter-cluster connections and individualized patterns of change over tumor growth (Figure 2.6c-d). These data demonstrate that the tumor immune response is a highly dynamic process.

2.3.3 Immune cell states are dynamically altered across immune organs with tumor growth

To understand the extent of systemic impacts on T cells, we leveraged unsupervised cell clustering to identify changes in T cell subsets, cell states, and potential cross-organ coordination of responses during tumor growth. Indeed, the T cell compartment was dramatically reorganized over both 4T1 and MMTV-PyMT tumor development (Figure 2.7a, Figure 2.8a-b). Tissues contained both unique and shared T cell subsets shifting with tumor growth (Figure 2.7b-c, Figure 2.8c-e). Blood and spleen profiles were more similar, dominated by $CD4^+$ T cells. In contrast, the tumor T cell pool had more shared subsets with the bone marrow, including an increasing double negative population and a decreasing NKT cell population (Figure 2.7c).

Demonstrating the breadth of immune reorganization in cancer, all T cell clusters changed in abundance across multiple tissues between early and late disease time points (Figure 2.7d). Of particular interest, tumor-infiltrating $CD103^+$ Tregs, described as potent suppressors of effector T cells[84], were abundant at day 7 but decreased with tumor progression (Figure 2.7e). This Treg subset expanded in the dLN, suggesting that distal suppressive mechanisms may support local changes to maintain a tumor-promoting systemic state. Anti-correlated changes extended to conventional $CD4^+$ T cells, where $CD44^+$ $CD90^{high}$ activated $CD4^+$ T cells decreased in the tumor but expanded in the lymph node (Figure 2.7f). The spleen showed the greatest change in $CD44^+$ $CD27^+$ memory $CD4^+$ T cells, which decreased with disease progression (Figure 2.7g). The blood showed increases of activated $CD44^+$ $CD4^+$ T cells expressing the CD31 adhesion receptor, which

can promote T cell survival in settings of inflammation (Figure 2.7h)[85]. $CD44^+$ $CD8^+$ T cells expanding in the lymph node expressed Ly6C (Figure 2.7j), which can support lymph node homing of central memory T cells[86]. $CD8^+$ T cells generally expanded in the tumor, but the most dominant cluster expressed high levels of PD-1 and CD69 previously associated with T cell dysfunction (Figure 2.7i)[87,88]. To explore the extent of dysfunction, we interrogated intratumoral and splenic T cells for their expression of CD101 and CD38, two markers recently identified as evidence of permanent T cell dysfunction[55]. Late-stage tumor burden led to accumulation of $CD38^+CD101^+$ $CD8^+$ T cells in the tumor as expected; however, this phenotype did not emerge in the spleen (Figure 2.7k), suggesting that $CD8^+$ T cells are altered differently in the TME and periphery. Similar changes in T cell composition were observed in the MMTV-PyMT model (Figure 2.8c-h).

A similar pan-organ clustering analysis for the mononuclear phagocyte subsets, including macrophages and dendritic cells (Figure 2.9), revealed correlated and anti-correlated systemic changes in cell states with tumor progression. As expected, the tumor-infiltrating subsets were distinct from peripheral subsets and expressed high levels of PD-L1.

We specifically interrogated protein expression dynamics of PD-1 and PD-L1 , the most commonly manipulated immune checkpoints by cancer immunotherapies to facilitate T cell responses[89]. While expression of these molecules is used clinically for patient stratification, it remains unclear whether they are expressed consistently or modulated dynamically over time. We indeed found dynamic PD-1 and PD-L1 expression on infiltrating immune cells ($CD45^+$) and non-immune cells ($CD45^-$ $CD31^-$) in the TME and in the periphery of both 4T1 and AT3 breast cancer models (Figure 2.10a- c). In fact, while the overall amount of PD-L1 expression was significantly less in the blood compared to the tumor, median leukocyte signal intensity was positively correlated between these tissues (Figure 2.10d, $r = 0.7487$, $p = 0.001$). Both PD-1 and PD-L1 were

promiscuously expressed across immune cell types, particularly within the TME (Figure 2.10e). The most prominent cells expressing PD-L1 in the periphery were non-classical monocytes[90] and cDCs, while PD-1 was abundantly expressed on T cells, neutrophils, and eosinophils. Dynamicity in PD-1 and PD-L1 expression suggests the potential for differential sensitivity to checkpoint blockade over the course of tumor development.

Changes in cellular proliferation or death rates are potential mechanisms contributing to immune composition alterations. We discovered that immune proliferation fluctuated systemically in a pattern unique to each site but was coordinated across all immune subsets within that site (Figure 2.11a-d). Changes in Ki67 and cleaved caspase-3 expression corresponded poorly with clusters that were increasing or decreasing in frequency in the spleen (Figure 2.11e). Thus, while tumor burden systemically alters proliferation and death, these processes alone likely do not account for the systemic immune alterations observed.

2.3.4 *De novo* T cell responses are impaired by pre-existing malignancy

Having established that tumor development drives an altered immune macroenvironment, we next examined whether immune responses to new challenges were affected. Type 1 immune responses are associated with strong cellular immunity and are generally thought to provide optimal anti-tumor immunity. To understand how type 1 immune responses might take place in the context of cancer, we challenged healthy or AT3 tumor-bearing mice with two well-described pathogens that induce potent type 1 immunity, lymphocytic choriomeningitis virus (LCMV), and *Listeria monocytogenes (Lm)*[91,92]. Tumor-burdened mice still cleared the pathogens from the spleen (Figure 2.12a-b), consistent with the lack of complete immunosuppression in solid tumor patients. However, the cellular immune response to infection was dramatically altered. The

differentiation of effector CD8$^+$ T cells, the magnitude of CD8$^+$ T cell proliferation, and expression of the cytolytic mediator granzyme B were all significantly impaired in tumor-bearing mice after infection (Figure 2.12c-e and Figure 2.13a). These results demonstrate an unappreciated impairment of new cellular immune responses in the context of cancer.

We previously found that CD8 T cells with markers of terminal dysfunction were only observed in the TME and not in the spleen (Figure 2.7k). Consistent with this hypothesis, splenic CD8 T cells harvested from either control or tumor-burdened animals were equally capable of producing the key effector cytokines IFNγ, TNFα, and IL-2 *in vitro* (Figure 2.13b). To test their functionality after infection, CD8 T cells from OT-I transgenic mice expressing a T cell receptor specific for ovalbumin (SIINFEKL) were isolated from control or tumor-bearing mice and transferred into recipient mice, which were infected with *Lm*-expressing ovalbumin (*Lm*-OVA). AT3 tumors still drove systemic changes in TCR transgenic mice (Figure 2.13c). OT-I CD8$^+$ T cells from control and tumor-bearing mice proliferated equivalently in control recipients at day 7 post-infection, the peak of the CD8$^+$ T cell response[91–93] (Figure 2.14a). However, when OT-I T cells were transferred into tumor-bearing recipients prior to infection, they expanded poorly, failed to induce T-bet expression associated with differentiation into effector cells, and expressed higher levels of PD-1 (Figure 2.14b). Similar results were also observed when polyclonal CD8$^+$ T cells from control or tumor-burdened mice were competitively transferred (Figure 2.14c). We found that antigen-specific central memory, effector memory, and short-lived effector CD8$^+$ T cells were less abundant in tumor-bearing mice at day 10 as well, suggesting that defects extend beyond peak proliferation and represent a fundamental impairment of *de novo* CD8$^+$T cell responses (Figure 2.14d). Together, these results demonstrate that cell extrinsic mechanisms suppress systemic T cell function in the tumor context.

Since tumor experienced $CD8^+$ T cells in the periphery were not dysfunctional, we hypothesized that impaired APC activity earlier during infection contributes to decreased peripheral $CD8^+$T cell activation. Dendritic cells (DCs) play a key role in orchestrating $CD8^+$T cell responses to *Lm*[94], and evidence suggests that circulating DCs in breast cancer patients have reduced antigen presentation capacity[95]. Therefore, we quantified costimulatory molecule expression on splenic DCs 2 days post-infection. DCs from AT3 tumor-bearing animals expressed lower levels of key costimulatory molecules CD80 and CD86 and the activation marker CD83 when compared to tumor-free controls (Figure 2.14e and Figure 2.13d). DCs from tumor-bearing mice also exhibited suboptimal activation at day 7 of infection, expressing lower levels of CD80, the adhesion molecule CD54 (ICAM-1), and PD-L1 (Figure 2.13e). This result suggests that the PD-1/PD-L1 axis does not cause the T cell response impairment and indicates that alternative strategies are likely required to induce new systemic T cell activity. We therefore sought to pharmacologically boost APC activation as a plausible strategy for achieving this goal. Anti-CD40 treatment drives potent and systemic APC activation as shown by elevated CD86 and PD-L1 on splenic DCs (Figure 2.14f and Figure 2.13f). In the context of infection, anti-CD40 treatment rescued $CD8^+$ T cell proliferation in tumor-burdened animals 7 days post infection (Figure 2.14g). We also observed significantly higher levels of activation markers CD80, CD54 and PD-L1 on DCs after treatment (Figure 2.13e), consistent with enhanced APC stimulation. In contrast, high doses of IL-12 or treatment with anti-CTLA-4 failed to rescue T cell proliferation (Figure 2.14g and Figure 2.13g), suggesting that T cell targeted interventions alone are not sufficient. These experiments demonstrate that APCs fail to drive optimal new T cell responses in the context of tumor burden.

2.3.5 Tumor resection reverses changes in systemic immune organization and responsiveness

Given that defects in T cell activity were reversed after removal from a tumor-burdened context, we asked whether tumor clearance was sufficient to revert changes in systemic immunity. We surgically resected tumors when systemic changes were evident across sites and allowed mice to recover from surgery for 14 days to mitigate immune confounders from wound healing. We carefully tracked both local recurrence and metastatic outgrowth by bioluminescent imaging. Successful tumor resection reversed changes in systemic immunity in the AT3 and 4T1 breast cancer and the MC38 colorectal cancer models (Figure 2.15a). Splenic immune cluster frequencies and proliferative behavior became comparable to control animals (Figure 2.15b and c, and Figure 2.16a-c). Successful resection restored compositional changes in spleen immune frequencies and T cell clusters; however, local recurrence in the AT3 model and overt lung metastasis in the 4T1 model led to intermediate phenotypes in the systemic immune state (Figure 2.15d and e, and Figure 2.16d and f-g). Local recurrence induced changes in the spleen comparable to primary tumors, but the composition of T cells was less dramatically altered. Lung metastasis induced more moderate changes, suggesting that systemic immune perturbations are not primarily the consequence of disseminated metastases. Finally, we interrogated DC and T cell responses 7 days after *Lm*-OVA infection and observed higher CD86 and PD-L1 expression on DCs in successfully resected mice (Figure 2.16h), and both T cell proliferation and granzyme B production were restored (Figure 2.15f-g). Local recurrence mitigated this rescue. Thus, changes in the immune macroenvironment, unlike those of T cells in the TME, are highly dependent on ongoing tumor burden and are reversible upon effective tumor clearance.

Finally, we investigated circulating cytokine levels to define potential mediators of tumor-driven systemic immune remodeling. We reasoned that candidate factors would be elevated in the

serum of AT3 tumor-burdened mice, reduced in successfully resected animals, and elevated again with local recurrence, or vice versa. We found that levels of the inflammatory cytokines IL-1α and G-CSF followed this pattern (Figure 2.16i). Notably, recent studies have implicated G-CSF as a driver of myeloid-derived suppressor cell and neutrophil expansion in preclinical models and cancer patients[14,96,97]. While IL-1β has been shown to promote tumor development locally in the TME, the role of IL-1α is less well understood, though it is elevated human breast cancers[98–100]. Consistent with the hypothesis that tumor-secreted factors contribute to systemic immune remodeling, G-CSF and IL-1α, but not IL-1β, were produced by AT3 cancer cells *in vitro* (Figure 2.16j). We next treated mice with IL-1 and G-CSF blocking antibodies starting 5 days after tumor initiation, prior to most systemic immune changes. We also investigated the potential systemic impacts of TGFβ, a pleiotropic cytokine known to play key roles in shaping the TME, including immune cell exclusion and immunosuppression[101,102]. Both IL-1 and G-CSF blockade significantly abrogated systemic immune remodeling while TGFβ blockade had no effect (Figure 2.15h and Figure 2.16e). IL-1 and G-CSF blockade reduced splenic neutrophils and less mature $CD11b^+$ myeloid cells (Figure 2.15i). Notably, IL-1 blockade also significantly reduced circulating levels of G-CSF, suggesting that IL-1 may act upstream to promote G-CSF production (Figure 2.16k), consistent with *in vitro* data from human tumor cell lines[103]. IL-1 blockade was additionally sufficient to reduce tumor effects on the splenic T cell composition, preventing the observed reductions in naïve and central memory $CD8^+$ T cells (Figure 2.15j-k). Thus, circulating IL-1α and G-CSF are critical mediators of tumor-driven systemic immune remodeling in this context.

2.4 Discussion

This study constructs a comprehensive landscape of the immune macroenvironment in cancer, revealing a systemic immune context to consider when targeting immune behavior therapeutically. Strong pre-existing T cell activity is associated with clinical benefit from currently available immunotherapies, but many cancer patients likely require the priming of new antitumor immune responses. However, the ability of a tumor-burdened immune system to establish new responses is poorly defined[104–106]. Cancer patients are more susceptible to opportunistic infections and mount less effective responses to vaccines[107,108], though the relative contributions of tumor driven systemic disruption and cytotoxic cancer therapies are debated. Here, we show that systemic immunity is disrupted to varying degrees across tumor types. Systemic immune alterations in breast cancer impair new immune responses, even to highly immunogenic pathogens that do not share tumor antigens. This challenges the idea that T cell dysfunction in cancer is limited to tumor-specific T cells experiencing chronic antigen exposure. Our data reveal impairment in the initial coordination of a T cell response by APCs, impacting T cell proliferation and differentiation. Impaired type 1 immune responses represent a fundamental, but previously unappreciated, obstacle for effective immunotherapy. These results, alongside promising clinical results of CD40 agonism in pancreatic cancer[67], strongly support combinatorial therapeutic strategies that include APC activation.

This work further reveals remarkable plasticity in the systemic immune state, as successful tumor resection largely reverted systemic immune disruptions. Influenced by physiological context, immunotherapies may have different consequences when applied pre- or post-operatively. These studies show that the immune macroenviornment in cancer is highly manipulatable, warranting further studies in cancer patients. Prior studies have connected systemic changes with

relapse in breast cancer patients, showing altered immune gene signatures in uninvolved lymph nodes and blood of patients with metastatic versus non-metastatic disease[109] and that circulating CD45RA^{-}Foxp3^{high} Tregs predict future relapse[110]. In breast tumor models, we show that the primary tumor is a primary driver of systemic immune reorganization, but that lung and lymph node metastasis are also associated with additional subtle changes. Future work to understand systemic immune alterations across cancer patients could inform prognosis and optimal therapy.

Our study lays the foundation for detailed studies of specific tumor macroenvironments to match our detailed understanding of tumor microenvironments in mouse tumor models and patients. Building a complete understanding of systems-level immunity in cancer should further our ability to drive effective and rationally-designed anti-tumor immune responses in all cancer patients.

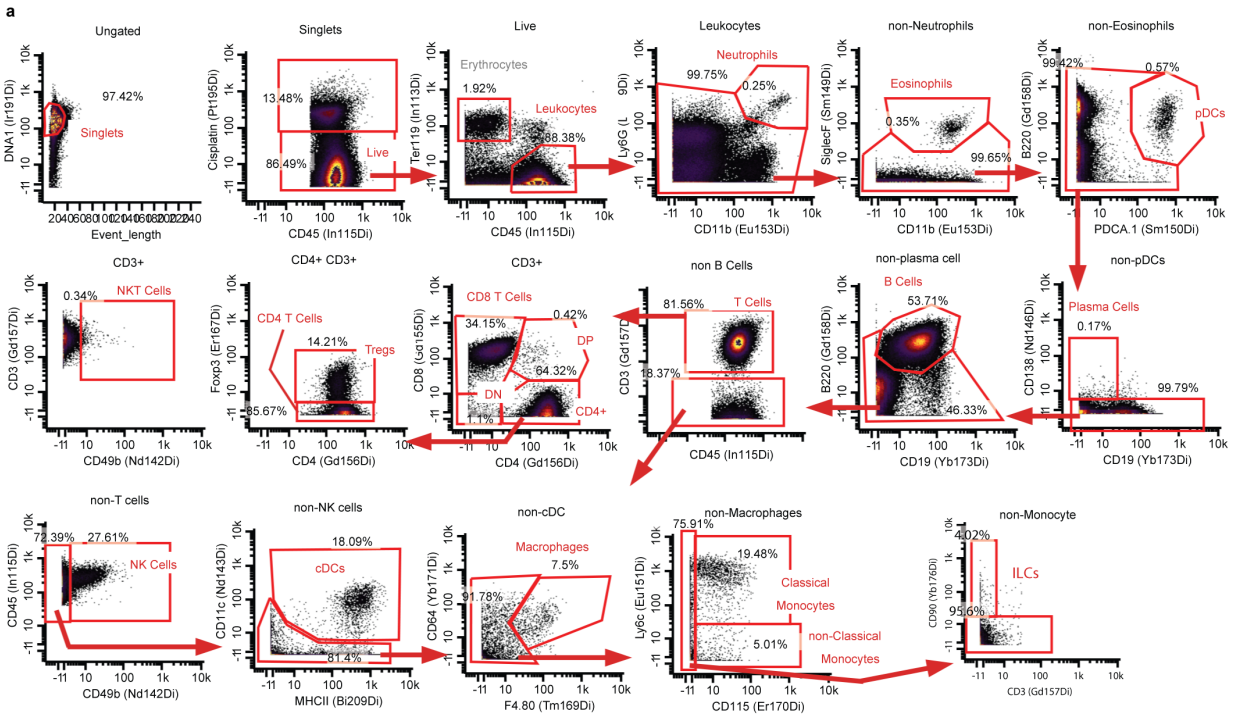

Figure 2.1: Main mass cytometry gating strategy

a, Main gating strategy for identifying major immune cell populations from mass cytometry datasets.

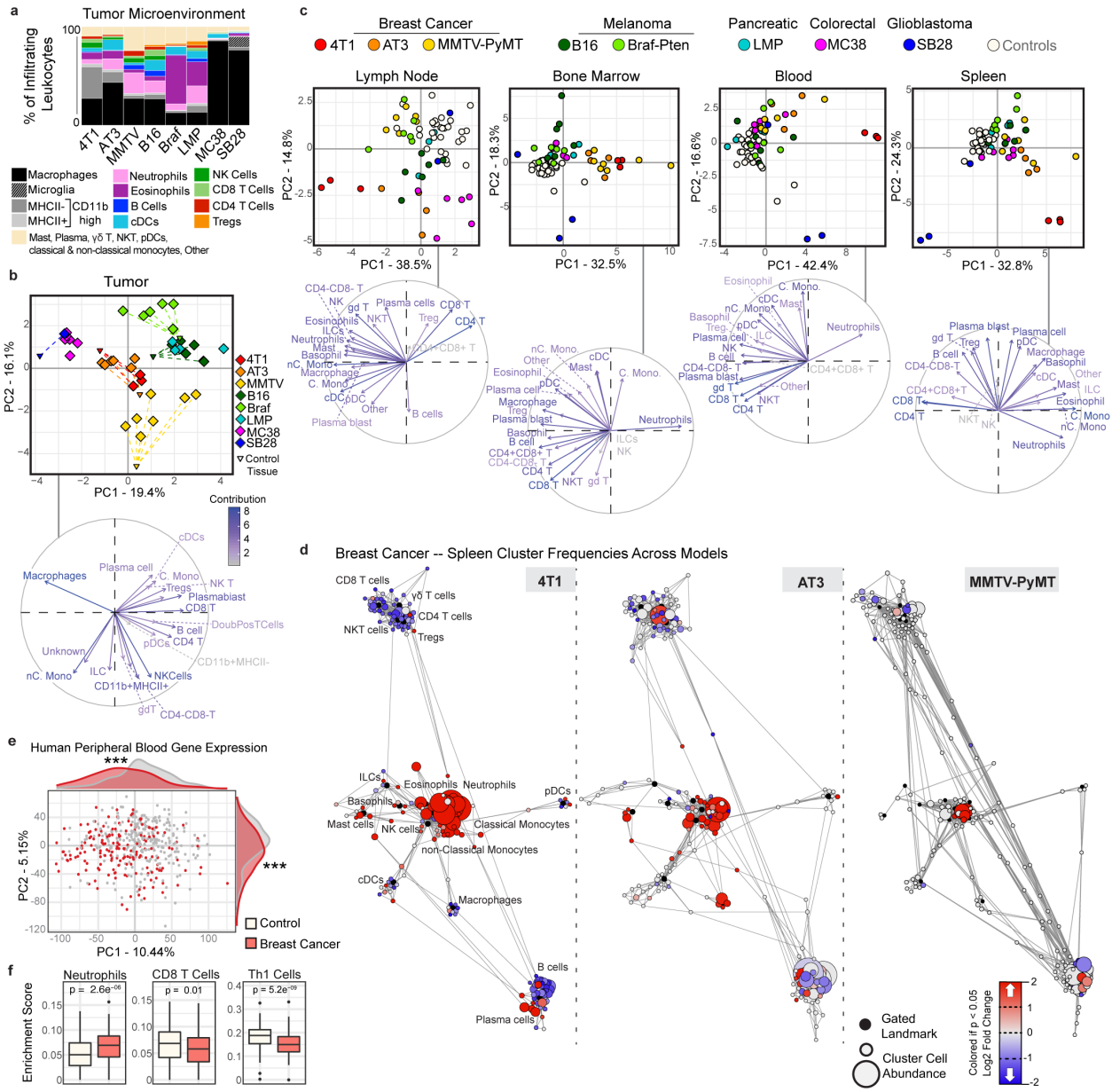

Figure 2.2: The systemic immune landscape is remodeled across tumor models.
a, Composition of tumor immune infiltrates across late stage mouse models, identified by manual gating (n = 3 independent animals for 4T1; n = 6 AT3; n = 7 MMTV-PyMT; n = 6 B16; n = 6 Braf-Pten; n = 4 LMP; n = 6 MC38; n = 1 SB28; n = 30 Controls). **b-c**, Principal component analysis (PCA) and corresponding vector plot of individual contributions for the tumor infiltrating immune frequencies (**b**), and the log2 fold change of immune frequencies for the tumor dLN, bone marrow, blood, and spleen (**c**) identified manually (n = 3 for SB28, otherwise as in panel (a)) **d**, Scaffold maps of spleen immune frequencies in breast tumor models (4T1, AT3, and MMTV-PyMT). Black nodes represent canonical cell populations identified manually. Other nodes reflect unsupervised clustering of leukocytes. Nodes are arranged by similarity using a force-directed graphing algorithm (see Methods). Red denotes populations significantly higher in frequency in

tumor-burdened animals compared to controls; blue denotes significantly lower frequency. For significant nodes ($q < 0.05$ by significance analysis of microarrays), the degree of coloring reflects log2 fold change (n as in panel (a)). **e-f**, PCA (**e**) and significant immune changes by cellular enrichment analysis (**f**) from human whole blood gene expression, comparing breast cancer patients (n = 173) and matched controls (n = 281), $p^{***} < 0.001$ by two-sided Wilcoxon rank-sum test with Benjamini-Hochberg correction. Box plots: center line, median; box limits, upper and lower quartiles; whiskers, 1.58x interquartile range / sqrt(n); points, outliers.

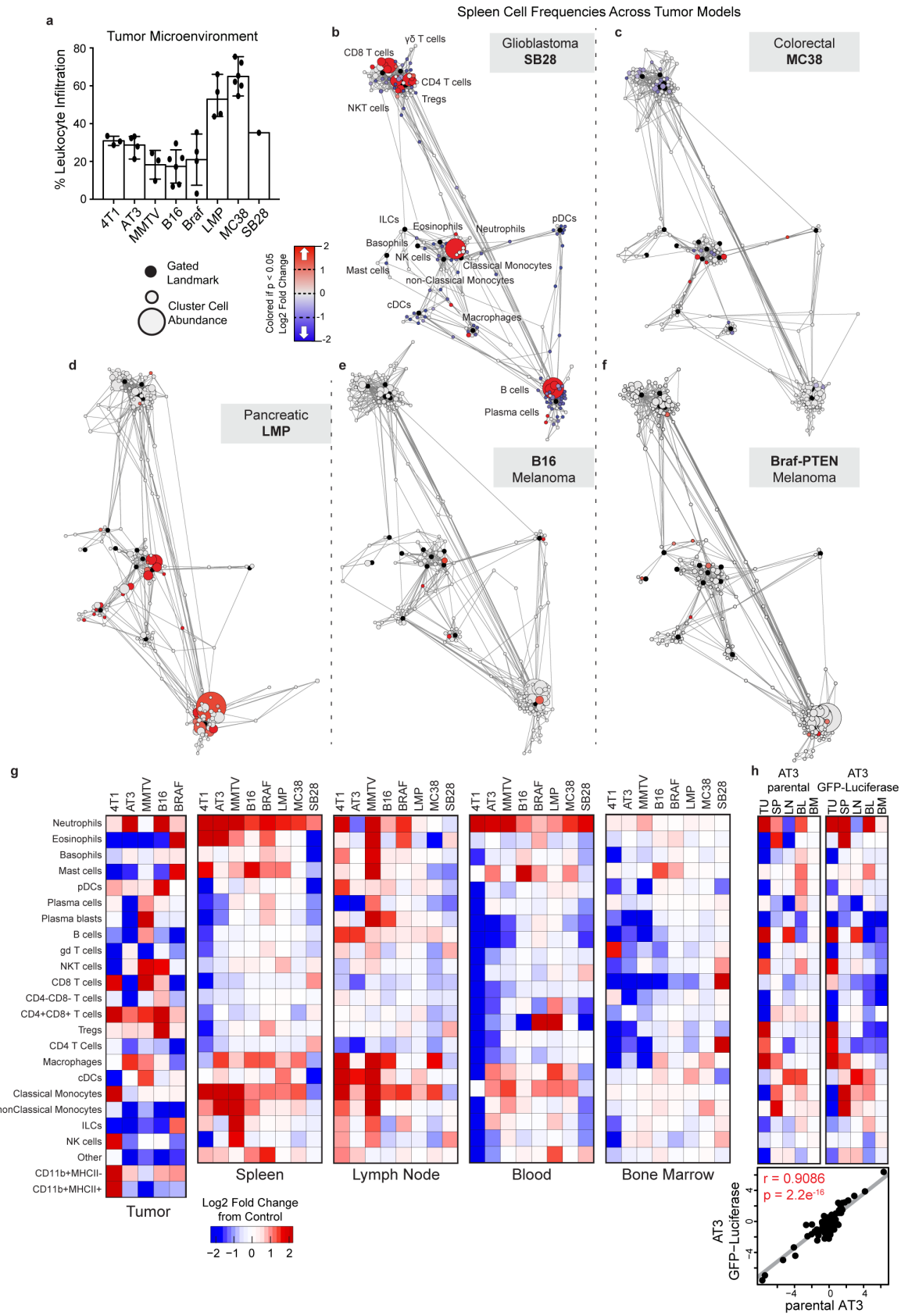

Figure 2.3: Systemic immunity is distinctly remodeled across tumor types.

a, Relative abundance of total leukocytes infiltrating the TME across eight tumor models. **b-f**, Scaffold maps of spleen cell frequencies across five distinct tumor models, SB28 glioblastoma (**b**), MC38 colorectal (**c**), LMP pancreatic (**d**), B16 melanoma (**e**), and Braf-PTEN melanoma (**f**), comparing late stage tumor burden to their respective health littermate controls. **g**, Heatmaps of the log2 adjusted fold change in bulk immune cell frequencies across all five tissues, where relevant, across all models. **h**, Heatmaps of the log2 adjusted fold change in bulk immune cell frequencies comparing the parental AT3 and engineered AT3 expressing reporters GFP and Luciferase, with cell labels in g. Lower inset shows linear correlation between these systemic immune features.

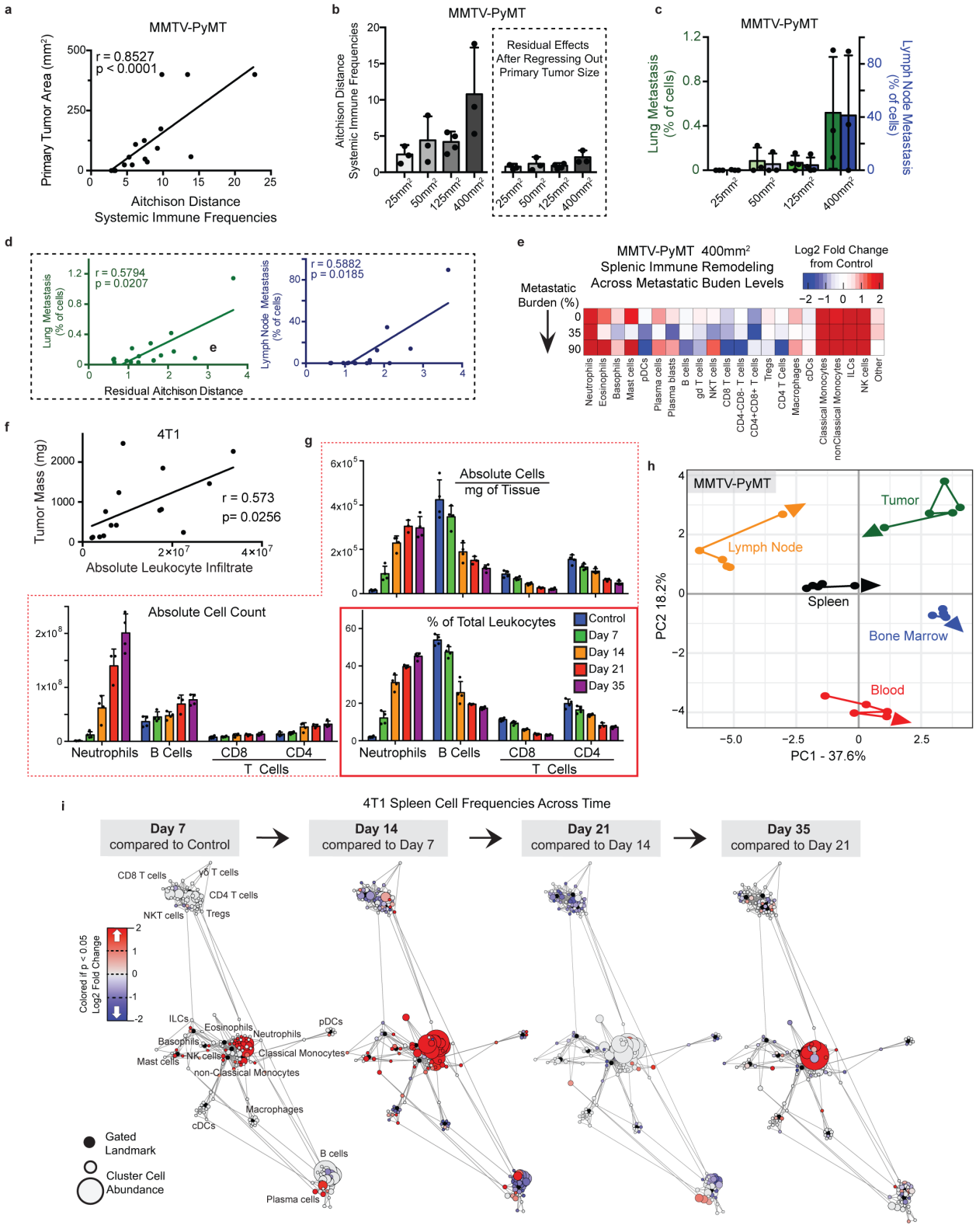

Figure 2.4: Systemic immunity is distinctly remodeled over tumor development.
a, Pearson correlation between MMTV-PyMT primary tumor size and change in systemic immune composition, measured as Aitchison distance. **b**, Degree of systemic immune change by Aitchison

distance over tumor growth (left) and after removing the contribution of primary tumor size by linear regression (right). **c**, Percent of PyMT expressing metastatic cancer cells in the lung (green) and primary dLN (blue). **d**, Pearson correlation between lung or lymph node metastasis and the residual changes in systemic immune composition after regressing out primary tumor burden. **e**, Heatmap of the log2 adjusted fold change in bulk spleen immune cell frequencies for each 400 mm^2 tumor-bearing mouse, ranging from 0 to high metastatic disease. **f**, Pearson correlation between tumor mass and absolute number of infiltrating leukocytes in 4T1 breast tumors. **g**, Spleen immune absolute cell counts, adjusted absolute cell counts per mg of tissue, and unadjusted immune frequencies at each time point for neutrophils, B cells and T cells of the 4T1 breast tumor model. **h**, PCA of relative immune cell frequencies from each major immune tissue over time in the MMTV-PyMT breast tumor model. Vectors designate progression from control (first point) to 25 mm^2, 50 mm^2, 125 mm^2, and 400 mm^2 (last point, arrowhead). **i**, Scaffold maps of immune cell frequencies in the spleen at each time point of 4T1 tumor burden, colored by log2 fold change in frequency compared to the previous time point.

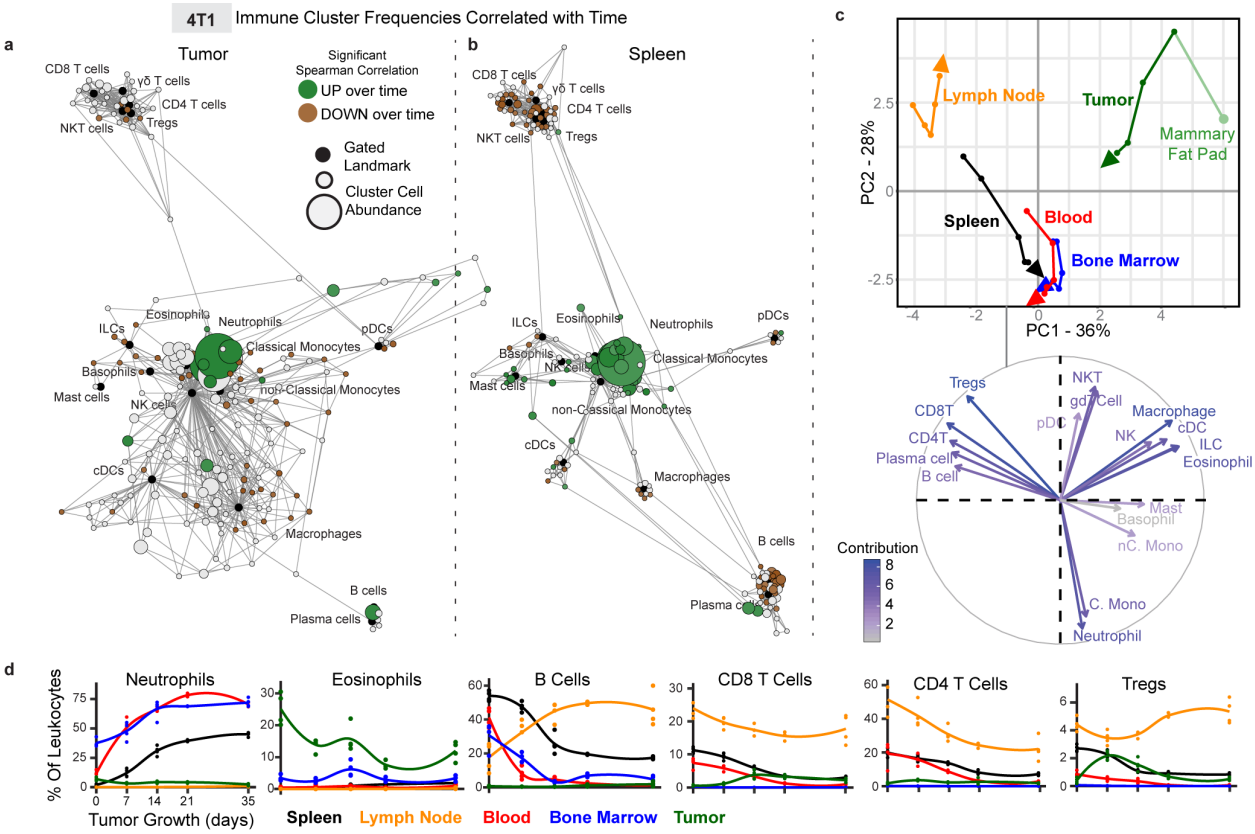

Figure 2.5: The systemic immune landscape is remodeled progressively with tumor development.

a-b, Scaffold maps of 4T1 tumor (**a**) and spleen (**b**) cell frequencies colored by significant Spearman correlation with time (across day 0, 7, 14, 21, and 35), $p < 0.05$ by two-sided t-test with Benjamini-Hochberg correction. Green denotes positive correlation, and brown denotes negative correlation. **c**, PCA and corresponding vector plot of contributions for immune cell frequencies from each immune tissue over 4T1 breast tumor growth. Vectors designate progression from control day 0 (first point) to day 7, 14, 21, and 35 (last point, arrowhead). **d**, Curves of mean cell frequencies across time from a subset of immune cell types contributing to c, colored by tissue corresponding with c. All panels from one experiment, n = 3 independent animals for day 21 and n = 4 for all other timepoints.

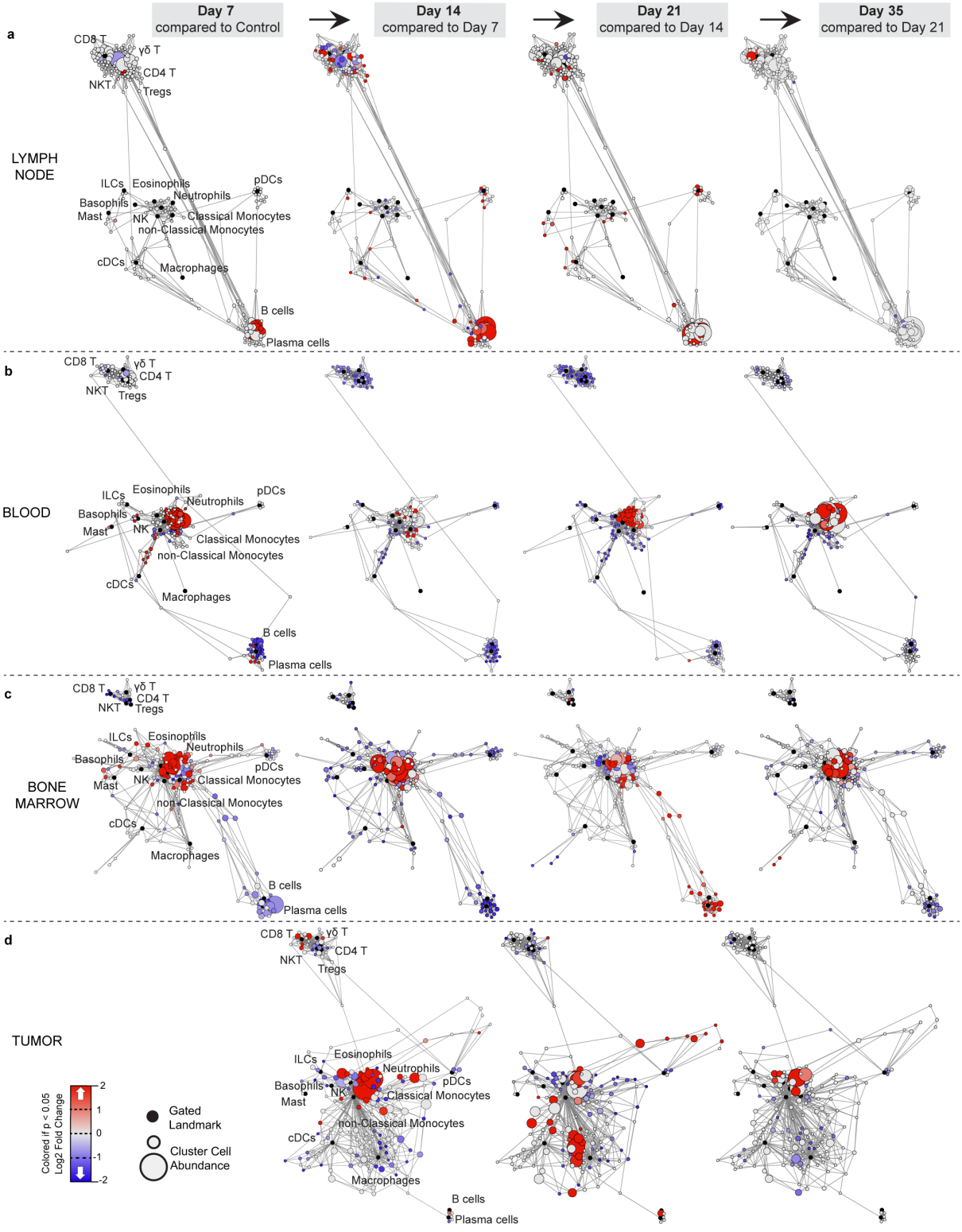

Figure 2.6: Immunity is distinctly remodeled by compartment over tumor development. **a-d**, Scaffold maps of immune cell frequencies over 4T1 tumor progression in the tumor dLN (**a**) blood (**b**), bone marrow (**c**), and tumor (**d**), colored by fold change relative to the previous time point.

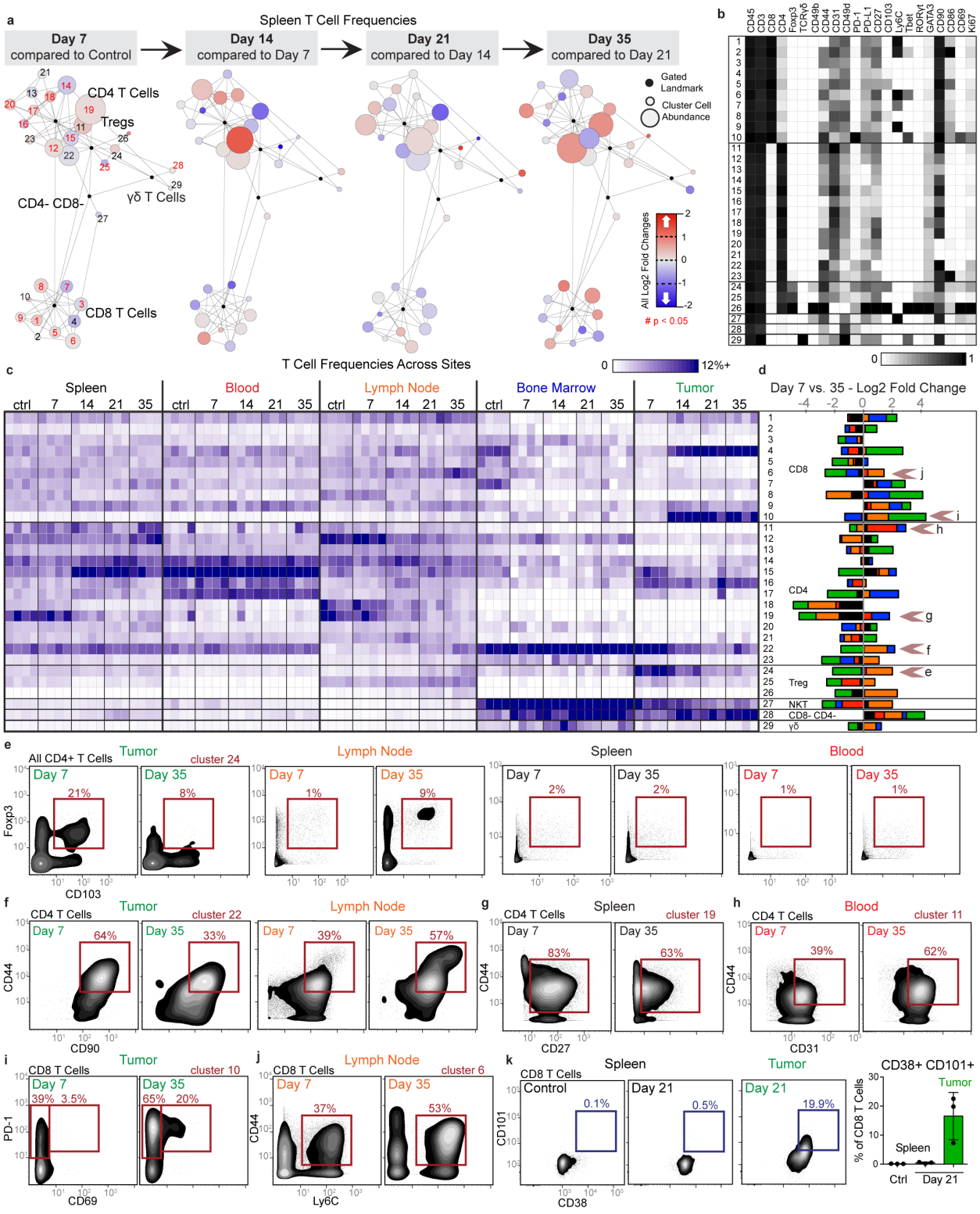

Figure 2.7: Tumor burden progressively changes the systemic T cell composition.
a-d, $CD3^+$ CD11b- leukocytes from all tissues from healthy and 4T1 tumor-burdened animals at progressive time points. **a**, Scaffold maps of the T cell cluster frequencies in the spleen at each disease stage, all colored by log2 fold change in frequency. Clusters with significant change over

time are highlighted in red in the first map, q <0.05 by multiclass significance analysis of microarrays. **b**, Heatmap of the protein expression defining each T cell cluster, column normalized to each protein's maximum positive expression. **c**, Heatmap of each T cell cluster frequency, by row, in each site and across the individual 3-4 animals per time point. **d**, Stacked bar plot of the log2 fold change in cluster frequency between early (day 7) and late (day 35) disease stage, colored by tissue. **e-j**, Representative scatter plots of key proteins defining T cell clusters that change in frequency in the designated tissues between early and late disease stage for Tregs (**e**), $CD4^+$ T cells (**f-h**), and $CD8^+$ T cells (**i-j**). **k**, Representative scatter plots and quantification of $CD101^+$ $CD38^+$ dysfunctional $CD8^+$ T cells in the spleen and tumor of health or day 21 tumor-burdened animals. All panels from one experiment, n = 3 independent animals for day 21 and n = 4 for all other timepoints. Barplot: centre, mean; whiskers, standard deviation.

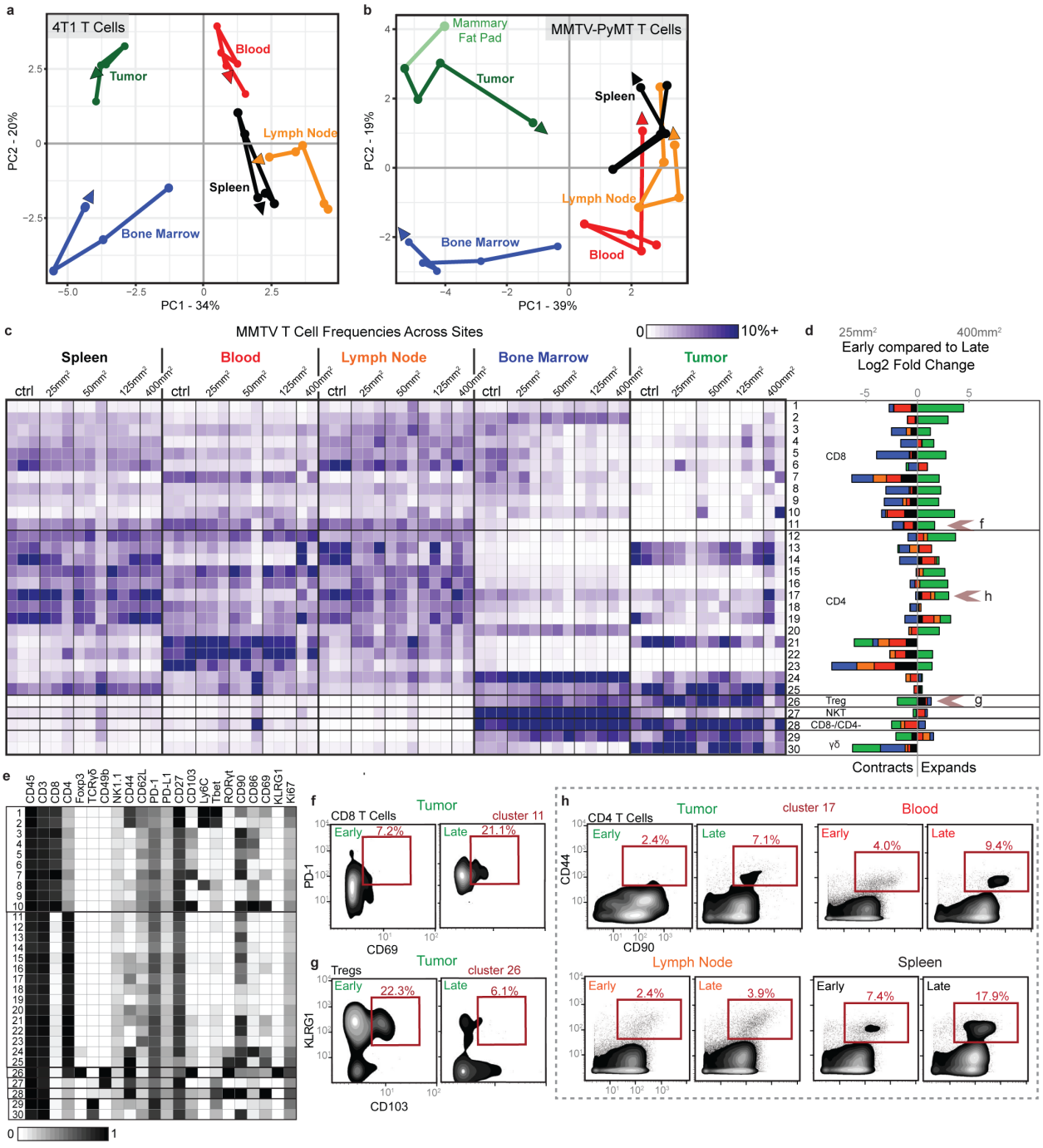

Figure 2.8: Tumor growth shifts the systemic T cell composition across models.
a-b, PCA of T cell cluster frequencies across lymphoid tissues over tumor development for the 4T1 (**a**) and MMTV-PyMT (**b**) breast tumor models. Vectors designate directional progression from control (first point) to late stage disease (last point, arrowhead). In **a**, tumor time points include day 7, 14, 21, and 35 after 4T1 cancer cell transplant. In **b**, tumor time points include tumor sizes of 25 mm^2, 50 mm^2, 125 mm^2, and 400 mm^2. **c-e**, $CD3^+$ CD11b- leukocytes from all tissues clustered together from healthy and MMTV-PyMT tumor-burdened animals at progressive tumor sizes. **c**, Heatmap of each T cell cluster frequency, by row, in each site and across the individual

2-3 animals per time point. **d**, Stacked bar plot of the log2 fold change in cluster frequency between early (25 mm^2) and late (400 mm^2) disease time points, colored by tissue. **e**, Heatmap of the protein expression defining each T cell cluster, column normalized to each protein's maximum positive expression. **f-h**, Representative scatter plots of key proteins that define T cell clusters changing in frequency in the designated site between early and late disease stage for $CD8^+$ T cells (**f**), Tregs (**g**), and $CD4^+$ T Cells (**h**).

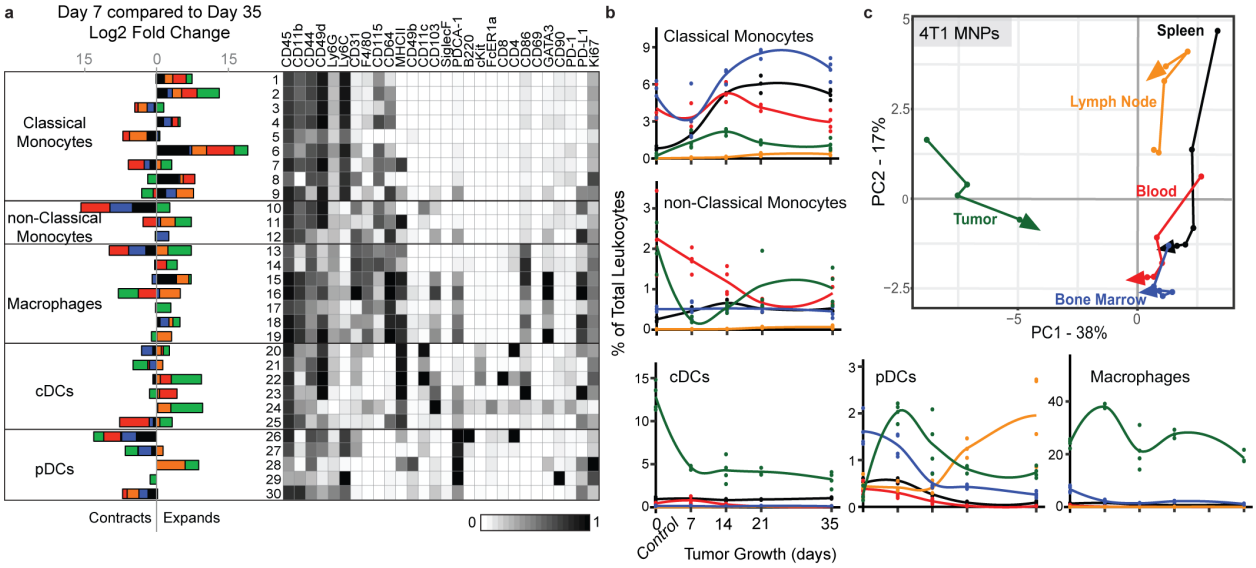

Figure 2.9: Tumor growth shifts the systemic mononuclear phagocyte composition.
a, CD3- CD19- leukocytes from all tissues clustered together from healthy and 4T1 tumor-burdened animals at progressive time points. Left, stacked bar plot of the log2 fold change in cluster frequency between early (day 7) and late (day 35) times points, colored by tissue. Right, heatmap of the protein expression defining each cluster, column normalized to each protein's maximum positive expression. **b**, Curves of the mean cell frequencies over time in the 4T1 breast tumor model from designated mononuclear phagocyte cell types, colored by tissue. **c**, PCA of the mononuclear phagocyte cell frequencies from each tissue over time in the 4T1 breast tumor model. Vectors designate progression from control (first point) to day 7, 14, 21, and 35 (last point, arrowhead). Coloring of tissues for a-c corresponds to labels in c.

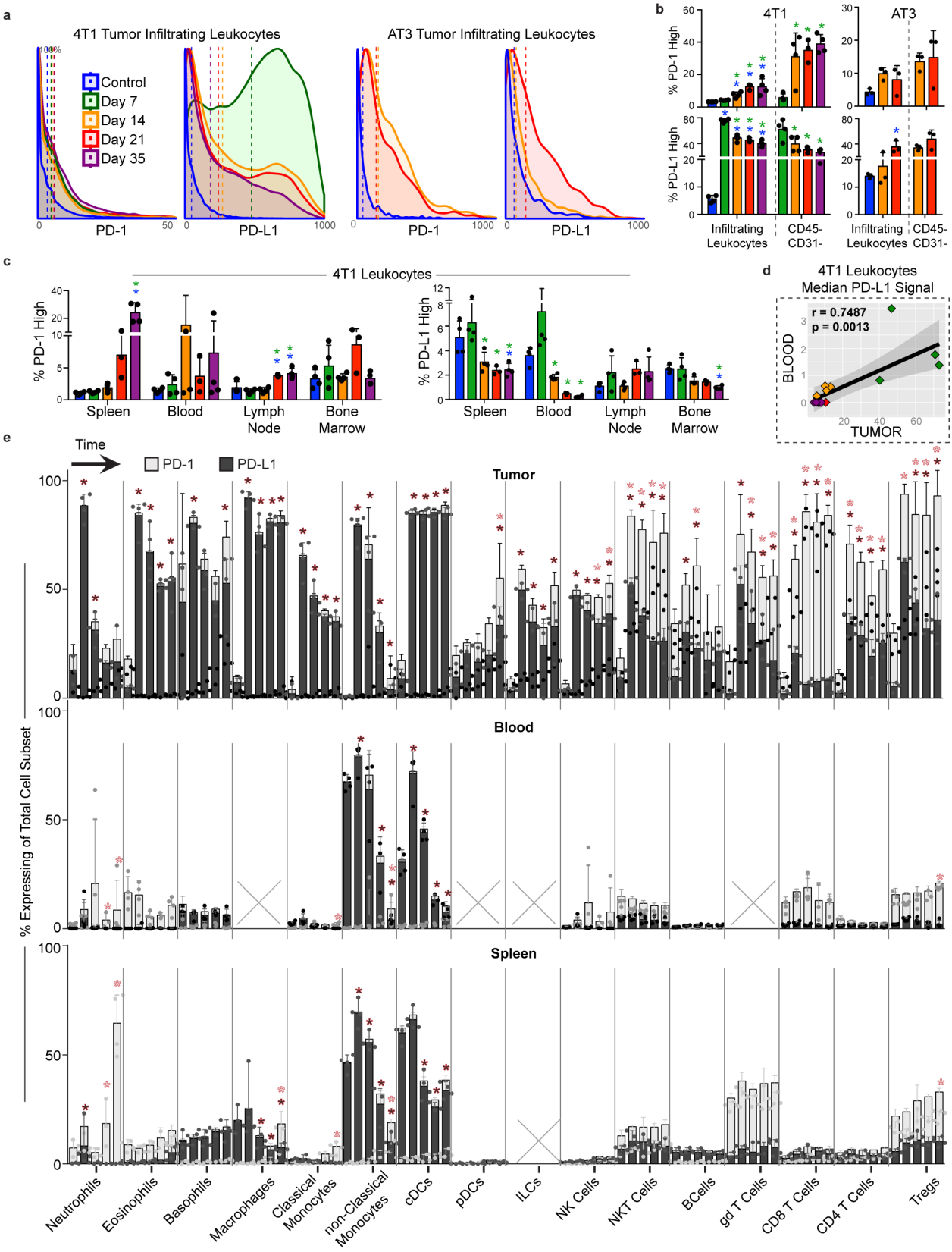

Figure 2.10: PD-1 and PD-L1 expression is dynamic over tumor growth.

a, Distribution of PD-1 and PD-L1 signal intensities on tumor infiltrating leukocytes over time in the 4T1 or AT3 breast tumor models. Coloring of time points for a-d corresponds to legend in a. **b**, Percent of total infiltrating leukocytes (left of dashed line) or CD45-, non-endothelial cells (right of dashed line) with high PD-1 or PD-L1 expression in the 4T1 or AT3 tumor models. **c**, Percent of leukocytes with high PD-1 or PD-L1 expression over time and across tissues, 4T1 model. **d**, Pearson correlation between median PD-L1 signal intensity on blood versus tumor infiltrating leukocytes, 4T1 model. **e**, Percent of each major immune cell subset expressing high PD-1 or PD-L1 in the tumor, blood, and spleen, identified manually. Cell subsets below 0.2% of total leukocytes were not included, X. Bars ordered by time point, beginning at healthy control. Double positive PD-1/PD-L1 expression was rare and not illustrated. p*<0.05, One-Way ANOVA, with Tukey correction versus control tissue or healthy mammary fat pad (blue in b-c, fill corresponding to bar color in e), or versus day 7 (green in b-c).

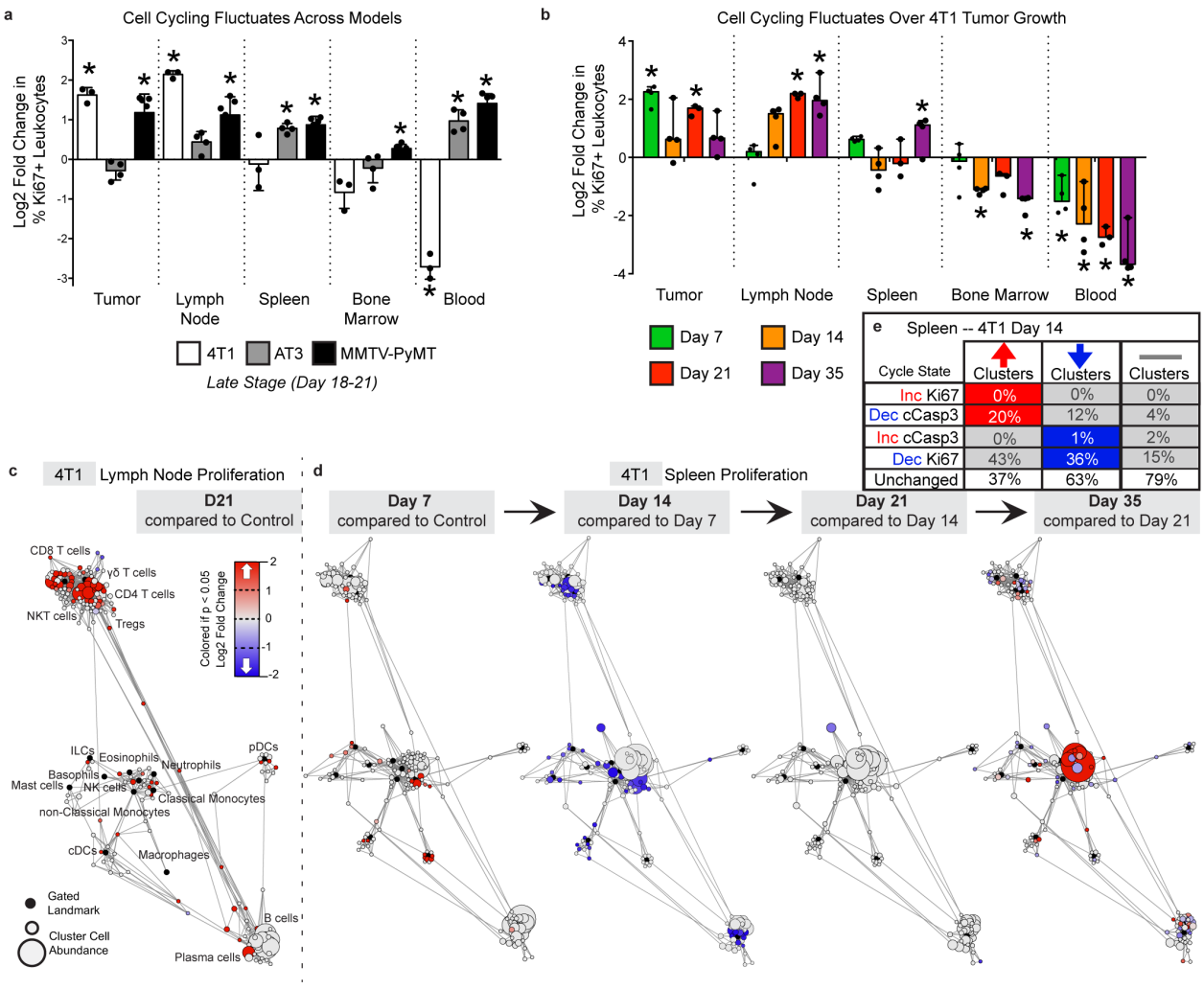

Figure 2.11: Tumor burden induces tissue-specific changes in immune cell cycling.
a-b, Log2 fold change in all Ki67-expressing leukocytes in each tissue tissues for 4T1, AT3, and MMTV breast tumors (**a**), and over 4T1 tumor progression (**b**). p*<0.05, One-Way ANOVA, with Tukey correction versus control. **c-d**, Statistical Scaffold maps of Ki67 expression in immune cells of the tumor dLN comparing control to day 21 (**c**) and the spleen over time (**d**) in 4T1 tumor-burdened animals. **e**, Percent of increasing clusters (red, total of 56), decreasing clusters (blue, total of 90), or unchanged cluster that have corresponding changes in cell cycle markers Ki67 and cleaved caspase-3.

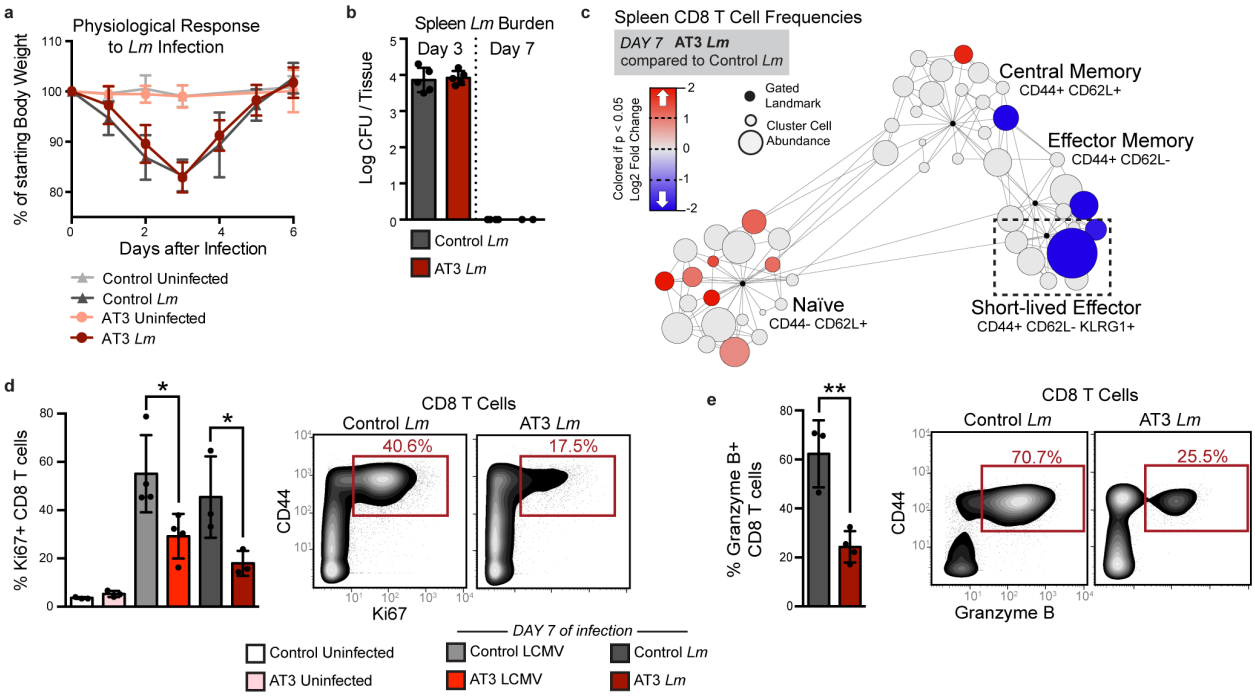

Figure 2.12: Tumor burden leads to impaired T cell responses to secondary infection.
a-b, Fold change in body weight after Listeria monocytogenes (*Lm*) infection (n = 11 independent animals for control groups and n = 9 for AT3 groups) (**a**), and quantification of *Lm* bacterial burden (**b**) in control and AT3 tumor-burdened animals (n = 5 for day 3 groups, n = 4 for control day 8, and n = 2 for AT3 day 8). **c**, Scaffold map of $CD8^+$ T cell frequencies in the spleen in AT3 tumor-burdened mice after 7 days of *Lm* infection, colored by fold change in frequency compared to infected control mice (n = 3 uninfected, n = 3 *Lm* infected), q <0.05 by significance analysis of microarrays. **d-e**, Quantification and representative scatter plots of splenic $CD8^+$ T cell proliferation (**d**) and granzyme B production (**e**) in response to LCMV Armstrong or *Lm* in healthy or AT3 tumor-burdened animals (n = 3 uninfected, n = 4 LCMV, and n = 3 *Lm* infected). For all barplots: p* <0.05, p** <0.01 by two-sided t-test; center, mean; whiskers, standard deviation.

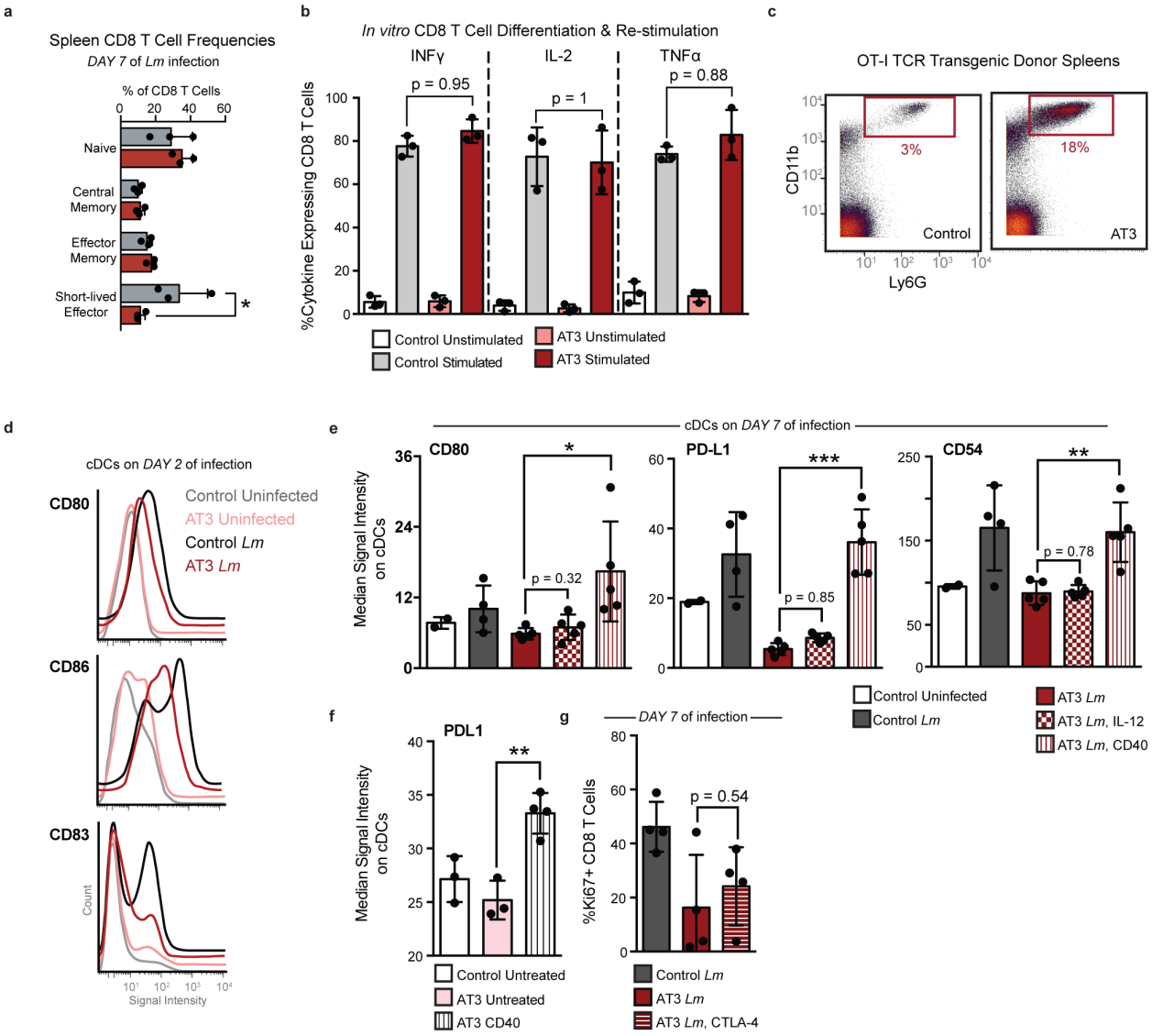

Figure 2.13: Tumor driven deficits in T cell responses are cell-extrinsic.
a, Quantification of all CD8$^+$ T cell populations in the spleen of healthy or AT3 tumor-burdened mice after 7 days of *Lm* infection, Two-Way ANOVA with Bonferroni correction. **b**, Expression of inflammatory cytokines, IFNγ, IL-2, and TNFα in splenic CD8$^+$ T cells isolated from control or AT3 tumor-burdened mice after *in vitro* differentiation with CD3, CD28 and IL-2, and re-stimulation with Brefeldin A and PMA Ionomycin. **c**, Scatter plots of CD11b and Ly6G showing expected neutrophilia in OT-I TCR transgenic mice with AT3 tumor burden. **d**, Histograms of CD80, CD86, and CD83 signal intensity on cDCs from healthy or AT3 tumor-burdened mice at day 2 of *Lm*-OVA infection. **e**, Median signal intensity of CD80, PD-L1 and CD54 activation markers on splenic cDCs from healthy or AT3 tumor-burdened mice compared to IL-12p70 or CD40 treatment at day 7 of *Lm*-OVA infection. **f**, Median signal intensity of PD-L1 on splenic cDCs from untreated or CD40 treated AT3 tumor-burdened (day 21) mice. **g**, Quantification of splenic CD8$^+$ T cell proliferation in healthy, untreated or CTLA-4-treated AT3 tumor-burdened animals in response to 7 days of *Lm*-OVA infection. p*<0.05, two-tailed t-test.

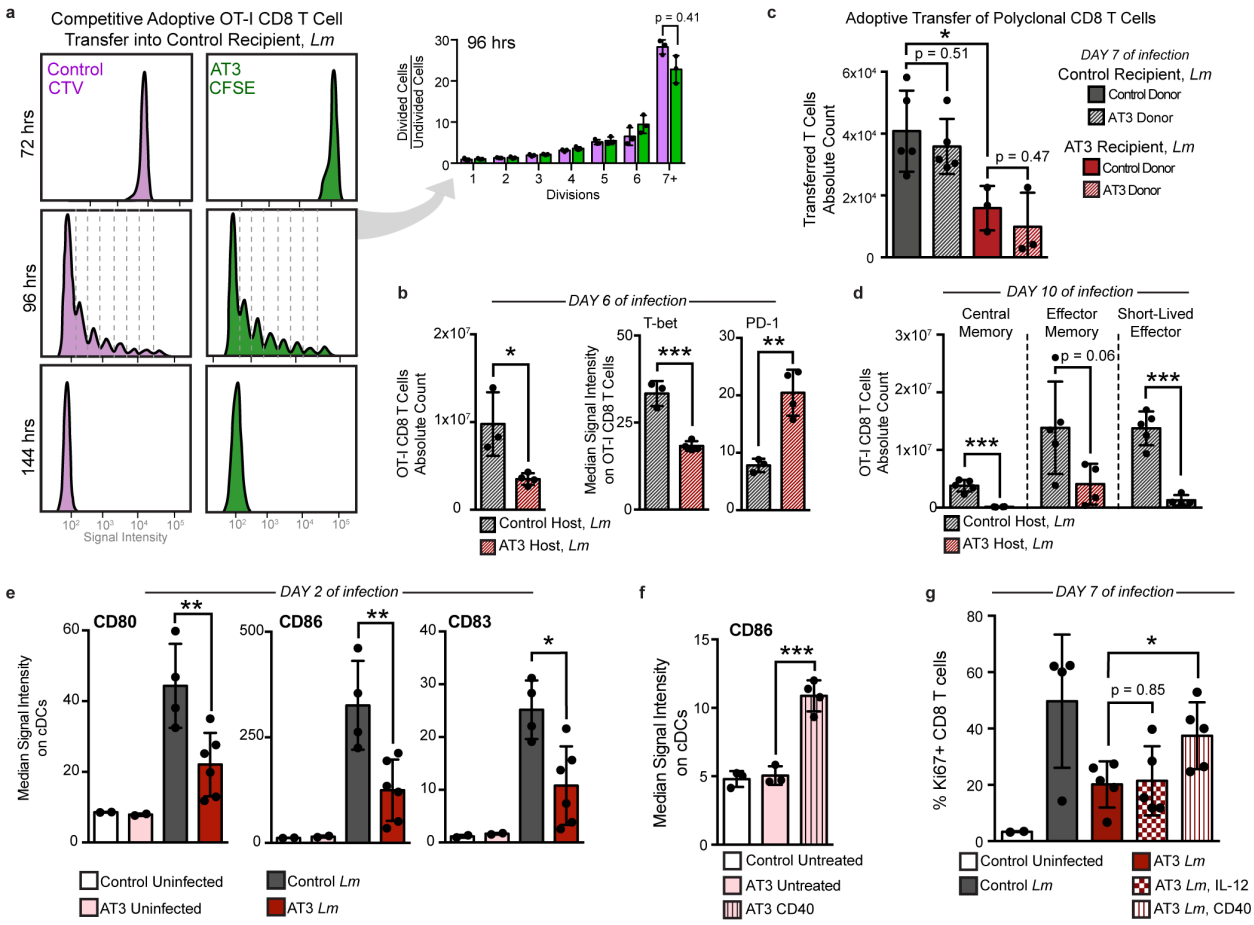

Figure 2.14: Tumor burden attenuates dendritic cell activation during secondary infection. **a**, OT-I T cell proliferation from control or tumor-burdened animals transferred into control recipients, and analyzed at 72, 96, and 144 hours post *Lm*-Ova infection (n = 3 independent animals per group). Quantification of 96 hours. **b**, Transferred OT-I T cell counts and median signal intensity of T-bet and PD-1 at day 6 of *Lm*-OVA infection (n = 3 for control, and n = 4 for AT3 hosts). **c**, Competitively transferred polyclonal $CD8^+$ T cell counts from congenic ($CD45.1^+$ AT3 tumor-burdened or $CD45.1^+CD45.2^+$ control) donors into CD45.2 control (n = 5) or AT3 tumor-burdened recipients (n = 4), after 7 days of *Lm* infection. **d**, $CD8^+$ T cell subtype counts from transferred $CD45.1^+$ OT-I T cells at day 10 of *Lm*-OVA infection (n = 5 for control, and n = 4 for AT3 hosts). **e**, Median signal intensity of CD80, CD86, and CD83 on splenic conventional dendritic cells (cDCs) from healthy (n = 4) or AT3 tumor-burdened (day 28, n = 6) mice, at day 2 of *Lm*-OVA infection (n = 2 for uninfected groups). **f**, Median signal intensity of CD86 on splenic cDCs from untreated (n = 3) or CD40 treated (n = 4) AT3 tumor-burdened (day 21) mice. **g**, Quantification of splenic $CD8^+$ T cell proliferation in healthy versus untreated, IL-12p70-treated, or anti-CD40 treated AT3 tumor-burdened animals at day 7 of *Lm*-OVA infection (n = 2 control uninfected, n = 4 control *Lm*, and n = 5 for AT3 groups). For all barplots: p* <0.05, p** <0.01, p*** <0.001 by two-sided t-test; center, mean; whiskers, standard deviation.

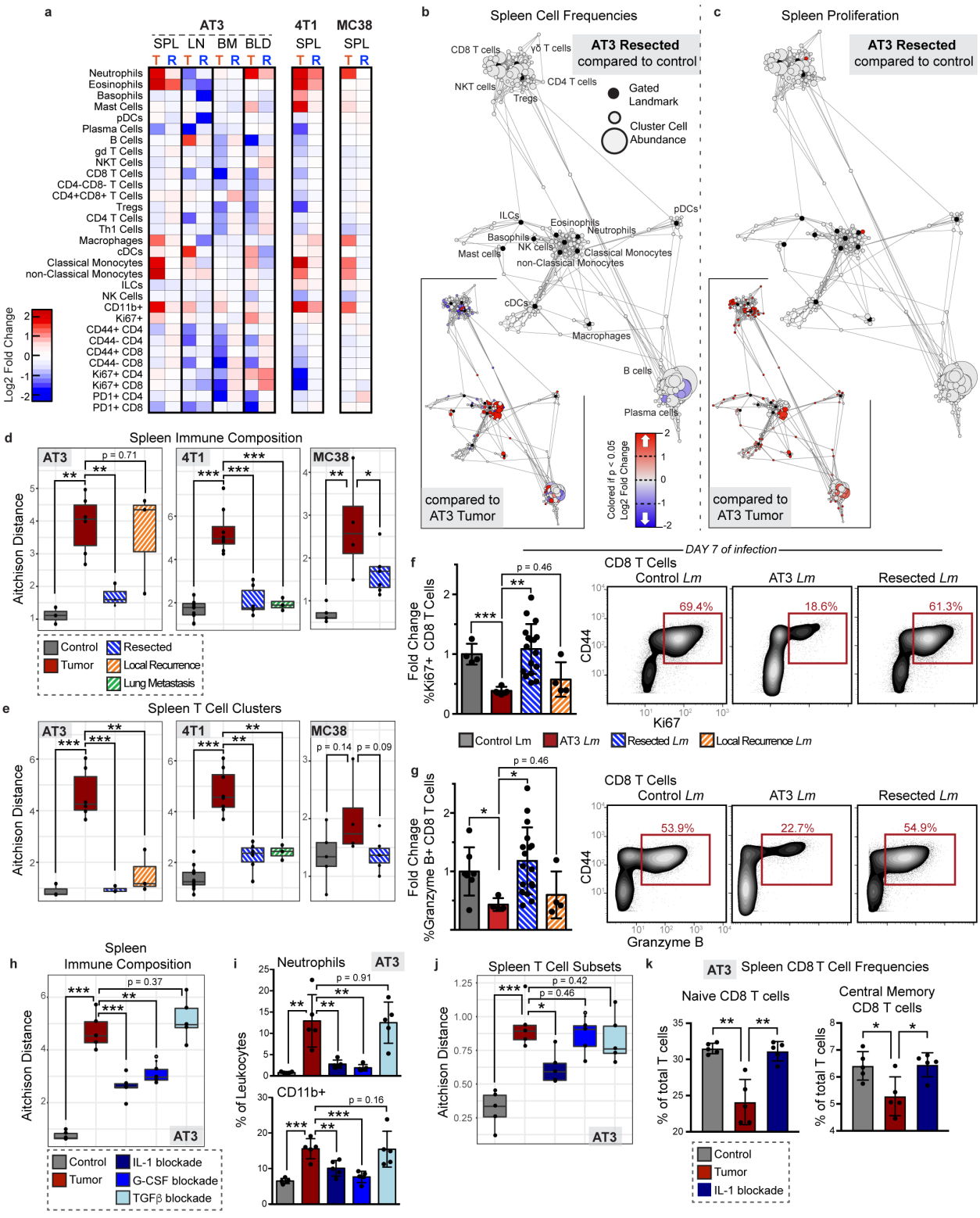

Figure 2.15: Tumor resection completely resets the systemic immune landscape.
a, Heatmaps of log2 fold changes in peripheral immune frequencies from tumor-burdened (T) or resected (R) mice. **b-c**, Scaffold maps of spleen immune frequencies (**b**) and proliferation (**c**) after AT3 resection compared to control (n = 3 per group). Insets show resected compared to tumor-

burden (n = 4), q <0.05 by significance analysis of microarrays. **d-e**, Compositional Aitchison distances in spleen immune frequencies (**d**) or T cell cluster frequencies (**e**) from control (n = 3 for AT3, 8 for 4T1, and 5 for MC38), tumor-burdened (n = 6, 8, and 4), resected (n = 3, 6 and 6), or locally recurrent mice for AT3 and distal lung metastasis for 4T1 (n = 3 for both)(2 independent experiments for 4T1 and 1 experiment for AT3 and MC38). **f-g**, Quantification and representative scatter plots of splenic $CD8^+$T cell proliferation (**f**) and granzyme B production (**g**) after *Lm* infection in control (n = 4 and n = 7), AT3 tumor-burdened (n = 4), resected (n = 17), or recurrent mice (n = 4), 3 independent experiments. **h-k**, Compositional Aitchison distances of spleen immune frequencies (**h**), spleen frequencies of neutrophil (top) and undefined $CD11b^+$ cells (bottom) (**i**), compositional Aitchison distances of T cell subset frequencies (**j**), and splenic $CD8^+$T cell frequencies (**k**) from control, or tumor-burdened mice untreated or with IL-1, G-CSF, or TGFβ antibody blockade (n = 5 per group, from 1 experiment). All box plots: center line, median; box limits, upper and lower quartiles; whiskers, 1.58x interquartile range / sqrt(n); points, outliers. All barplots: p* <0.05, p** <0.01, p*** <0.001 by two-sided t-test; center, mean; whiskers, standard deviation.

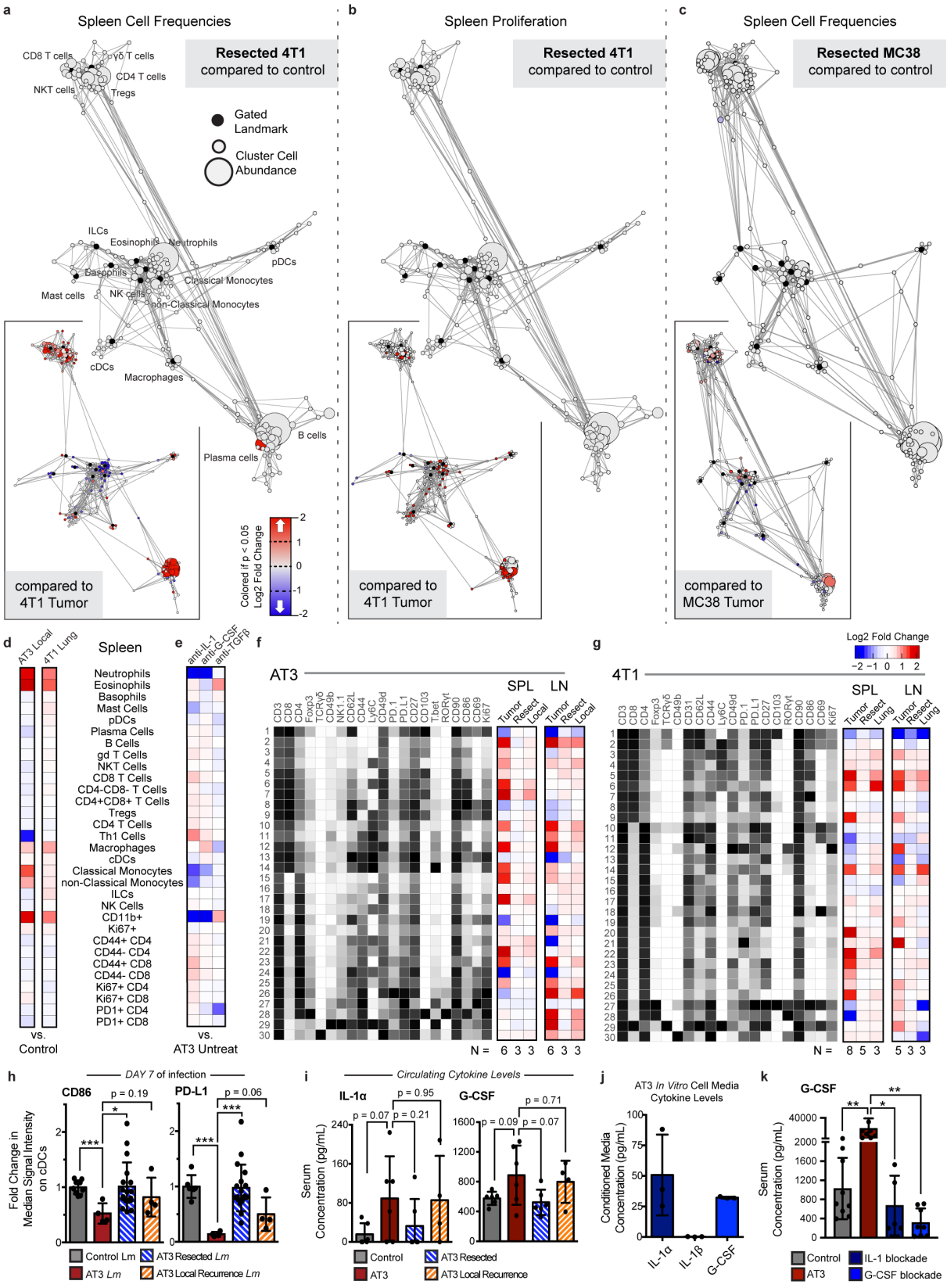

Figure 2.16: Tumor resection resets systemic immune organization and function.

a-c, Statistical scaffold maps of spleen immune cell frequencies (**a**) and proliferation by Ki67 expression (**b**) in 4T1-resected mice, and of spleen immune cell frequencies in MC38-resected mice (**c**) compared to healthy control. Insets show resected mice compared to tumor-burdened mice. **d-e**, Heatmap of the log2 fold changes in splenic immune cell frequencies for local or lung recurrences from control mice (**d**), and for IL-1, G-CSF, or TGFβ blockade from untreated AT3 tumor-burdened mice (**e**). **f-g**, Heatmaps of T cell cluster expression profiles and log2 fold change from control for AT3 (**f**) and 4T1 (**g**) for the spleen and dLN. **h**, Median signal intensity of CD86 and PD-L1 on splenic cDCs from healthy, AT3 tumor-burdened, resected, or resected mice with local recurrence at day 7 of *Lm*-OVA infection. **i**, Concentration of circulating cytokines, IL-1α and G-CSF from healthy, AT3 tumor-burdened, resected, or resected mice with local recurrence. **j**, Concentration of circulating G-CSF in control or AT3 tumor burdened mice left untreated or after 1L-1 or G-CSF blockade. **k**, Concentration of cytokines, IL-1α, IL-1β, and G-CSF from *in vitro* cell culture media conditioned with AT3 cancer cells. $p^{*}<0.05$, two-tailed t-test.

Table 2.1: Antibody panel used for mass cytometry experiments.

MAIN

Channel	Metal	Protein	Concentration (ug/ml)	Clone	Vendor	Catalogue #	Lot #
113	In	Ter119	3	TER119	Biolegend	116202	B250339
115	In	CD45	6	30-F11	Biolegend	103102	B253429
139	La	Ly6G	1.5	1A8	Biolegend	127602	B265459
140	Ce	IgD	3	11-26c.2a	Biolegend	405702	B165867
141	Pr	CD16/32	3	2.4G2	BD	553142	8130843
142	Nd	CD49b	0.75	HMα2	Biolegend	103501	--
143	Nd	CD11c	0.75	N418	Biolegend	117302	B191075
144	Nd	CD49d	3	R1-2	BioLegend	103610	B254009
145	Nd	CD27	0.75	LG.3A10	Biolegend	124202	B233065
146	Nd	CD138	0.1875	281-2	Biolegend	142502	B233106
147	Sm	PD-L1	3	10F.9G2	Biolegend	124302	B220492
148	Nd	CD103	3	2E7	Biolegend	121402	B249116
149	Sm	SiglecF	1.5	E50-2440	BD	552125	7264727
150	Nd	PDCA-1	0.75	129c1	Biolegend	127102	B188381
151	Eu	Ly6C	0.75	HK1.4	Biolegend	128002	B253176
152	Sm	Ki67	6	SolA15	BD	556003	6280947
153	Eu	CD11b	3	M1/70	Biolegend	101202	B261558
154	Sm	cKit	1.5	2B8	Biolegend	105802	B241900
155	Gd	CD8	3	53-6.7	Biolegend	100702	B237234
156	Gd	CD4	0.75	RM4-5	Biolegend	100506	B251707
157	Gd	CD3	0.75	17A2	Biolegend	100202	B241388
158	Gd	B220	1.5	RA3-6B2	Biolegend	103202	B170375
159	Tb	PD-1	0.75	29F.1A12	Biolegend	135202	B196019
160	Gd	NK1.1	1.5	PK136	Biolegend	108702	B187819
161	Dy	T-bet	6	O4-46	BD	561263	3032551
162	Dy	TCRgd	3	GL3	Biolegend	118101	--
163	Dy	CD62L-FITC	3	MEL-14	Biolegend	104443	B235113
164	Dy	CD86	0.375	GL-1	Biolegend	105002	B244244
165	Ho	CD69	0.75	Polyclonal	R&D	AF2386	UIU011808A
166	Er	FcER1a	1.5	MAR-1	Biolegend	134321	B243579
167	Er	Foxp3	3	NRRF-30	eBioscience	14-4771-80	1972297
168	Er	RORgt	6	B2D	eBioscience	14-6981-82	--
169	Tm	F4/80	1.5	BM8	Biolegend	123102	B226029
170	Er	CD115	1.5	AFS98	Biolegend	135521	--
171	Yb	CD64	6	X54-5/7.1	Biolegend	139302	B270355
172	Yb	GATA3	3	16E10A23	Biolegend	653802	B201420
173	Yb	CD19	0.75	6D5	Biolegend	115502	B166684
174	Yb	IgM	6	RMM-1	Biolegend	406502	B256697
175	Lu	CD44	0.375	IM7	Biolegend	103002	B246298
176	Yb	CD90	0.75	G7	Biolegend	105202	B187334
209	Bi	MHC II	0.1875	M5/114.15.2	Biolegend	107602	B141287

Other Substitutes

Channel	Metal	Protein	Concentration (ug/ml)	Clone	Vendor	Catalogue #	Lot #
89	Y	Ter119	6	TER119	BioLegend	116202	B250339
113	In	CD45.2	3	104	BioLegend	109802	B269632
115	In	CD45.1	3	A20	BioLegend	110702	B237865
140	Ce	H2KB	3	AF6-88.5	BioLegend	116501	--
140	Ce	KLRG1	0.75	2F1	BD	562190	8113778
141	Pr	GranzymeB	3	QA16A02	BioLegend	372202	--
144	Nd	CD43	6	S7	BD	553268	8268962
160	Gd	CD31	6	MEC13.3	BioLegend	102512	B226133
161	Dy	CD80	3	16-10A1	BioLegend	104702	B237237
162	Dy	CD83	3	Michel-19	BioLegend	121502	B253543
163	Dy	CD62L	3	95218	R&D	MAB5761	--
168	Er	CD25	3	PC61	BioLegend	102014	B235231
172	Yb	cCaspase3	1	5A1E	Fluidigm	3172023A	0391807
174	Yb	CD127	4	A7R34	BioLegend	135002	B168578
174	Yb	GranzymeB	1.5	GB11	BioRad	MCA2120	--
176	Lu	CD54	3	YN1/1.7.4	BioLegend	116102	B197852
163	Dy	a-FITC		Polyclonal	Southern Biotech	6400-01	L1217-QE58
FITC	NA	CD62L	3	MEL-14	Biolegend	104406	B233014

Table 2.2: Change in spleen immune cell frequencies with tumor burden.

two-sided Wilcoxon rank-sum tests with Benjamini-Hochberg correction

4T1		
Immune Cell Type	**raw pVal**	**adjusted pVal**
ClassicalMonocytes	5.28E-05	0.000686167
Neutrophils	5.28E-05	0.000686167
Bcells	6.55E-05	0.000785893
Tregs	8.11E-05	0.000891661
gdTCells	0.000123	0.001232678
nonClassicalMonocytes	0.000186	0.001670571
CD8TCells	0.00072	0.004320097
NKCells	0.000598	0.004320097
PlasmaCells	0.00072	0.004320097
Eosinophils	0.001481	0.007403936
CD4TCells	0.006514	0.026055191
pDCs	0.011825	0.035476343
cDCs	0.779707	0.779706761
Macrophages	0.460883	0.779706761

Number of Animals	
Controls	**8**
Tumor	**17**

p < 0.05
P < 0.1
nonsignificant

AT3		
Immune Cell Type	**raw pVal**	**adjusted pVal**
ClassicalMonocytes	8.73E-05	0.00122275
Neutrophils	0.000115	0.001489942
Eosinophils	0.000253	0.003031765
nonClassicalMonocytes	0.000419	0.004611308
Macrophages	0.000869	0.008688611
Bcells	0.001384	0.012454788
CD8TCells	0.005073	0.040583301
pDCs	0.007574	0.053018294
cDCs	0.019242	0.096212185
NKCells	0.016096	0.096212185
CD4TCells	0.037797	0.151188336
gdTCells	0.156288	0.468863135
PlasmaCells	0.488718	0.921212055
Tregs	0.921212	0.921212055

Number of Animals	
Controls	**10**
Tumor	**12**

MMTV-PyMT		
Immune Cell Type	**raw pVal**	**adjusted pVal**
ClassicalMonocytes	0.014248	0.170976956
NKCells	0.014248	0.170976956
nonClassicalMonocytes	0.014248	0.170976956
Neutrophils	0.022494	0.247436983
CD8TCells	0.034611	0.311495018
pDCs	0.034611	0.311495018
Eosinophils	0.051913	0.415303719
cDCs	0.075927	0.531488741
Bcells	0.150786	0.799846106
Macrophages	0.271899	0.799846106
CD4TCells	0.446873	0.799846106
PlasmaCells	0.672604	0.799846106
Tregs	0.672604	0.799846106
gdTCells	0.799846	0.799846106

Number of Animals	
Controls	**3**
Tumor	**7**

Table 2.3: Antibody panel used for flow cytometry experiments.

Fluorophore	Protein	Ratio	Clone	Vendor	Catalogue #	Lot #
PE-Dazzle594	CD3	1:100	17A2	Biolegend	100246	B246894
PacificBlue	CD4	1:100	RM4-5	BD	558107	56828
BV786	CD8	1:100	53-6.7	BD	563332	--
APC-Cy7	CD45	1:100	30-F11	Biolegend	103116	B266564
APC	CD38	1:50	90	Biolegend	102712	B259441
PE	CD101	1:50	Moushi101	eBioscience	12-1011-80	1911703
PE-Cy7	PD-1	1:100	29F.1A12	Biolegend	135215	--
BV421	TCRb	1:100	H57-597	Biolegend	109229	B264324
PE	IFNg	1:100	XMG1.2	Biolegend	505808	B265789
BV711	IL-2	1:100	JES6-5H4	Biolegend	503837	B264812
FITC	TNFa	1:100	MP6-XT22	BD	554418	68325
BV650	CD8	1:100	53-6.7	Biolegend	100741	B253266
BV510	KLRG1	1:100	2F1/KLRG1	Biolegend	138421	--
BV421	CD62L	1:100	MEL-14	Biolegend	104435	--
FITC	CD45.2	1:100	104	Biolegend	109805	--
APC	CD8	1:100	53-6.7	Biolegend	100711	--
PE-Cy7	MHC II	1:200	AF6-120.1	Biolegend	116419	--
PE	CD45.1	1:100	A20	Biolegend	110708	B262097

2.5 Materials and Methods

Animals:

All mice were housed in an American Association for the Accreditation of Laboratory Animal Care–accredited animal facility and maintained in specific pathogen-free conditions. Animal experiments were approved and conducted in accordance with Institutional Animal Care & Use Program protocol number AN157618. Wild-type female BALB/c, C57BL/6, and B6x 129 F1 mice between 8-10 weeks old were purchased from The Jackson Laboratory and housed at our facility. 4T1 ($1X10^5$ cells / 100 µl) or AT3 ($5x10^5$ cells / 100 µl) breast cancer cells were transplanted into the fourth mammary fat pad. SB28 glioblastoma cells ($1x10^5$ cells / 2 µl) were transplanted into the right cerebral hemisphere by stereotactic injection. MC38 colon cancer cells ($1x10^5$ cells / 100µl), B16-F10 melanoma cancer cells ($1x10^5$ cells / 100 µl), or LMP pancreatic cancer cells ($2x10^5$ cells / 100 µl) were transplanted into the subcutaneous region of the flank. Female MMTV-PyMT mice were bred at Stanford University. Tyr::CreER; $Braf^{V600E/+;}$ $Pten^{lox/lox}$ mice were purchased from Jackson Laboratory and housed at our facility. Tumors were considered well-established when they reached approximately 1 cm^3 in volume. TCR Transgenic OT-I CD45.1 mice and heterozygous CD45.2, CD45.1 mice were bred at our facility. Animals were housed under standard SPF conditions with typical light/dark cycles and standard chow.

Cell Lines:

4T1 cells were gifted from Dr. Mary-Helen Barcellos-Hoff (UCSF). AT3 cells were gifted from Dr. Ross Levine (MSKCC). For *in vivo* experiments tracking tumor growth and recurrence after resection, we used 4T1 cells expressing mCherry-Luciferase and AT3 cells expressing GFP-Luciferase. SB28 cells, derived from a NRasV12;shp53;mPGDF transposon-induced glioma[111],

were gifted from Dr. Hideho Okada (UCSF). LMP cells, derived from the $Kras^{G12D/+}$;LSL-$Trp53^{R172H/+}$;Pdx-1-Cre model of pancreatic cancer[112], were gifted from Dr. Edgar Engleman (Stanford University). MC38 cells and B16-F10 cells gifted from Dr. Jeffrey Bluestone (UCSF). 4T1, MC38, B16, and SB28 cells were cultured in RPMI-1640, and AT3 and LMP cells were cultured in DMEM, all supplemented with 10% fetal calf serum, 2 mM L-glutamine,100 U/ml penicillin and 100 mg/ml penicillin/streptomycin.

Infectious Agents:

Listeria monocytogenes strain 10403s expressing OVA (*Lm*-OVA) was originally kindly provided by Dr. Shomyseh Sanjabi (UCSF).[113] Lm-OVA stocks frozen at -80° C were grown overnight at 37° C in BHI broth supplemented with 5 ug/ml erythromycin. Then, overnight cultures were sub-cultured by diluting into fresh BHI broth supplemented with 5 ug/ml erythromycin and grown for 4 hours. Bacteria CFU was then quantified by measuring optical density at 600 nm. Bacteria were then diluted to $5X10^4$ CFU / 100 µl in sterile PBS and 100 µl was injected per mouse i.v. via the retro-orbital vein.

Lymphocytic choriomeningitis virus (LCMV) was kindly provided by Dr. Jason Cyster (UCSF) and mice were infected with pre-titered and aliquoted stocks stored in PBS at -80° C and diluted with sterile PBS. Mice were infected with $2x10^5$ PFU by intraperitoneal injection.

Mass Cytometry Antibodies:

All mass cytometry antibodies and concentrations used for analysis can be found in Supplementary Table1. Primary conjugates of mass cytometry antibodies were prepared using the MaxPAR antibody conjugation kit (Fluidigm) according to the manufacturer's recommended

protocol. Following labeling, antibodies were diluted in Candor PBS Antibody Stabilization solution (Candor Bioscience GmbH, Wangen, Germany) supplemented with 0.02% NaN3 in PBS to between 0.1 and 0.3 mg/ml and stored long-term at 4° C. Each antibody clone and lot was titrated to optimal staining concentrations using primary mouse samples.

Cell Preparation:

All tissue preparations were performed simultaneously from each individual mouse, as previously reported[46]. After euthanasia by $C0_2$ inhalation, peripheral blood was collected via the posterior vena cava prior to perfusion of the animal and transferred into sodium heparin-coated vacuum tubes prior to dilution in PBS with 5 mM EDTA and 0.5% BSA (PBS/EDTA/BSA). Spleens and lymph nodes were homogenized in PBS/EDTA at 4° C. Bone marrow was flushed from femur and re-suspended in PBS/EDTA at 4° C. Tumors were finely minced and digested in RPMI-1640 with 4 mg/ml collagenase IV, and 0.1 mg/ml DNase I. After digestion, re-suspended cells were quenched with PBS/EDTA at 4° C. All tissues were washed with PBS/EDTA and re-suspended 1:1 with PBS/EDTA and 100 mM cisplatin (Enzo Life Sciences, Farmingdale, NY) for 60 s before quenching 1:1 with PBS/EDTA/BSA to determine viability as previously described[83]. Cells were centrifuged at 500 x g for 5 min at 4° C and re-suspended in PBS/EDTA/BSA at a density between 1-10 x 106 cells/ml. Suspensions were fixed for 10 min at room temperature (RT) using 1.6% paraformaldehyde in PBS and frozen at -80° C.

Mass-Tag Cellular Barcoding:

Mass-tag cellular barcoding was performed as previously described[114]. Briefly, 1 x 10^6 cells from each animal were barcoded with distinct combinations of stable Pd isotopes in 0.02%

saponin in PBS. Samples from any given tissue from each mouse per experiment group were barcoded together. Cells were washed once with cell staining media (PBS with 0.5% BSA and 0.02% NaN3), and once with 1X PBS, and pooled into a single FACS tube (BD Biosciences). After data collection, each condition was deconvoluted using a single-cell debarcoding algorithm[114].

Mass Cytometry Staining and Measurement:

Cells were resuspended in cell staining media (PBS with 0.5% BSA and 0.02% NaN3) and metal-labeled antibodies against CD16 and CD32 were added at 20 mg/ml for 5 min at RT on a shaker to block Fc receptors. Surface marker antibodies were then added, yielding 500 µl final reaction volumes and stained for 30 min at RT on a shaker. Following staining, cells were washed 2 times with cell staining media, then permeabilized with methanol for at 10 min at 4° C. Cells were then washed twice in cell staining media to remove remaining methanol and stained with intracellular antibodies in 500 µl for 30 min at RT on a shaker. Cells were washed twice in cell staining media and then stained with 1ml of 1:4000 191/193Ir DNA intercalator (Fluidigm) diluted in PBS with 1.6% paraformaldehyde overnight. Cells were then washed once with cell staining media and then two times with double-deionized (dd) H_20. Care was taken to assure buffers preceding analysis were not contaminated with metals in the mass range above 100 Da. Mass cytometry samples were diluted in dd H_20 containing bead standards (see below) to approximately 10^6 cells per ml and then analyzed on a CyTOF 2 mass cytometer (Fluidigm) equilibrated with dd H_20. We analyzed 1-5 x 10^5 cells per animal, per tissue, per time point, consistent with generally accepted practices in the field.

Mass Cytometry Bead Standard Data Normalization:

Data normalization was performed as previously described[46]. Briefly, just before analysis, the stained and intercalated cell pellet was resuspended in freshly prepared dd H_20 containing the bead standard at a concentration ranging between 1 and 2 x 10^4 beads/ml. The mixture of beads and cells were filtered through a filter cap FACS tubes (BD Biosciences) before analysis. All mass cytometry files were normalized together using the mass cytometry data normalization algorithm[115], which uses the intensity values of a sliding window of these bead standards to correct for instrument fluctuations over time and between samples.

Mass Cytometry Gating Strategy:

After normalization and debarcoding of files, singlets were gated by Event Length and DNA. Live cells were identified by Cisplatin negative cells. All positive and negative populations and antibody staining concentrations were determined by titration on positive and negative control cell populations.

Scaffold Map Generation:

Statistical scaffold maps were generated using the open source Statistical Scaffold R package available at github.com/SpitzerLab/statisticalScaffold with modifications detailed below. Statistical scaffold analysis combines unsupervised clustering to identify immune cell subsets with dimensionality reduction using a force-directed graph to visualize the organization of immune cells within a tissue. Regions of the graph are easy to identify due to the incorporation of canonical immune cell types defined manually as 'landmarks' in the graph. As previously described[46,83], cells from each tissue for all animals were clustered together and then deconvolved into their

respective samples. Cluster frequencies or the Boolean expression of specific proteins for each cluster were passed into the Significance Analysis of Microarrays algorithm[116] (using a q-value cutoff of 0.05), and the fold change results were reported (rather than the binary significance cutoff as originally implemented in Spitzer et al., 2017). Cluster frequencies were also correlated with the time from tumor inoculation using Spearman's rank-ordered correlation. All results were tabulated into the Scaffold map files for visualization through the graphical user interface, with coloring modifications to graph the spectrum of fold change or correlation strength. The fold change was log2 normalized and graphed with an upper and lower limit of a four-fold difference, unless otherwise indicated. Cluster frequencies were calculated as a percent of total live leukocytes or parent immune subset as indicated. The spleen data from the 4T1 model were used to spatialize the initial Scaffold map because all major, mature immune cell populations are present in that tissue.

Cell Frequency Heat Map Generation:

Specified subsets, i.e. T cells and mononuclear phagocytes, were manually gated from each tissue for all animals and clustered together. Cluster frequencies were calculated as a percent of total live nucleated cells within that subset (excluding erythrocytes). T cells were identified as $CD3^{+}$, $CD11b^{lo}$. Mononuclear phagocytes were defined as $CD11b^{+}$, $CD19^{-}$, $CD3^{-}$, $Ly6G^{-}$. Heatmaps of the resulting cluster frequencies were generated in R.

Human Gene Expression Analysis:

Whole blood microarray data was generated by The Norwegian Women and Cancer (NOWAC) study and is deposited in the European Genome-Phenome Archive under accession

number EGAS00001001804 as previously reported[117]. Principal component analysis of centered and scaled data was performed in R using the prcomp function. xCell cell type enrichment analysis[118] was performed in R using the xCell package (https://github.com/dviraran/xCell) using a customized list of cell populations known to exist in peripheral whole blood (B-cells, basophils, $CD4^+$ T cells, $CD4^+$ naïve T cells, $CD4^+$ T central memory, $CD4^+$ T effector memory, $CD8^+$ T cells, $CD8^+$ naïve T cells, $CD8^+$ T cells, $CD8^+$ T central memory, $CD8^+$ T effector memory, cDC, class-switched memory B-cells, eosinophils, erythrocytes, megakaryocytes, memory B-cells, monocytes, naïve B-cells, neutrophils, NK cells, NKT, pDC, plasma cells, platelets, Tgd cells, Th1 cells, Th2 cells, and Tregs).

***In vitro* $CD8^+$ T cell Differentiation and cytokine production:**

Mice bearing 21-day AT3 tumors were euthanized and their spleens harvested and dissociated. $CD8^+$ T cells were enriched using the EasySep Streptavidin Negative Selection Kit with the following biotinylated markers: CD11b, MHCII, CD11c, Gr1, B220, CD4, CD44, and Ter119. Isolated $CD8^+$ T cells were then stimulated with plate-bound anti-CD3 (1 ug/ml) and suspended in anti-CD28-containing (0.5 ug/ml) T cell media for 3 days. The cells were then removed from CD3+CD28 stimulation and rested for 1 day. Cells were then restimulated with PMA and ionomycin or left unstimulated for 4 hours with brefeldin A and analyzed by flow cytometry.

Adoptive T Cell Transfer:

For OT1 and polyclonal adoptive transfers, $CD8^+$ T cells were isolated from spleens of CD45.1 OT1 TCR transgenic or CD45.1, CD45.2 heterozygote wildtype or CD45.1 BoyJ mice by

enrichment with EasySep Streptavidin Negative Selection Kit with the following biotinylated markers: CD11b, MHCII, CD11c, Gr1, B220, CD4, and Ter119. Cells were stained with CFSE or Cell Trace Violet and 1 x 10^5 cells were then adoptively transferred into each recipient mouse via the retroorbital vein.

Quantifying Bacterial Burden:

To quantify bacterial burden, spleens were harvested and dissociated. Cells from each mouse were lysed in 0.5% Triton X-100 in PBS and cells were serially diluted in duplicate and aliquots were then added to BHI agar and incubated overnight at 37° C. Colonies grown were then counted to quantify bacterial CFU present.

Treatments:

For infection studies, *in vivo* antibody treatments were given i.p. starting on day 0 of *Lm*-Ova infection: 200 μg of agonistic anti-CD40 (FGK4.5, BioXCell) on day 0, 225 μg of recombinant IL-12p70 (BioLegend) daily, and 200 μg of anti-CTLA-4 (9H10, BioXCell) on day 0 and day 3. For cytokine inhibition studies, *in vivo* antibody treatments were given i.p. starting on day 5 after injection of AT3 cells: 10 ug of blocking anti-GCSF (67604, R&D Systems) daily, and 200 ug of both blocking anti-IL-1a (ALF-161, BioXCell) and blocking anti-IL-1R (JAMA-147, BioXCell) every 3 days. We observed compensatory elevations in circulating IL-1α with anti-IL-1α treatment, so we added anti-IL-1R to ensure sufficient blockade of this pathway.

Tumor Resection:

Mice bearing 14-day 4T1 tumors or 16 to 21-day AT3 or MC38 tumors (between 350-

550mm^3) were anesthetized by intraperitoneal (i.p) injection with a mixture of ketamine and xylazine, and titrated to effect with isoflurane from a precision vaporizer. The surgical site was shaved and sterilized with 70% ethanol and 10% povidone iodine. An incision was made subcutaneously at the anterior midline and along the flank of the side with the tumor, using surgical scissors, to reveal the inguinal mammary tumor. The tumor was teased away using forceps and the surgical wound closed with wound clips. Wound clips were removed after 7 days. 20-30% of AT3 or 4T1-resected mice had tumor recurrence due to incomplete removal of primary tumors or outgrowth of micro-metastases. These mice were separated from successful resection analyses.

Cytokine Quantification:

For *in vivo* circulating plasma cytokines, mice were bled via the retroorbital vein using heparinized capillary tubes. Blood was then centrifuged at 1000 x g for 10 minutes and the supernatant plasma was removed for analysis. For tissue culture supernatants, cells were grown for 48 hours in fresh media, then supernatant was removed, centrifuged at 3000 x g for 10 minutes to remove debris. Plasma and tissue culture supernatant samples were sent to Eve Technologies (Calgary, AB), and analyzed using a multiplex cytokine array.

Flow Cytometry:

All flow cytometry antibodies and concentrations used for analysis can be found in Table 2.3. Cells were stained for viability with Zombie-NIR stain. Cell surface staining was performed in cell staining media (PBS with 0.5% BSA and 0.02% NaN3) for 15 minutes at room temperature. Intracellular staining was performed after fixing cells with BioLegend FluoroFix Buffer and permeabilizing cells with BioLegend's Intracellular Staining Perm Wash Buffer. The following

anti-mouse antibodies were used: (PE-Dazzle594) – CD3 (clone 17A2), (Pacific Blue) – CD4 (clone RM4-5), (BV786) – CD8 (clone 53-6.7), (APC-Cy7) – CD45 (clone 30-F11), (APC) – CD38 (clone 90), (PE) – CD101 (clone Moushi101) , (PD1) – PE-Cy7 (clone 29F.1A12), (BV421) – TCRβ (clone H57-597), (PE) – IFNγ (clone XMG1.2), (BV711) – IL2 (clone JES6-5H4), (FITC) – TNFα (clone MP6-XT22), (BV650) – CD8 (clone 53-6.7), (BV510) – KLRG1 (clone 2F1-KLRG1), (BV421) – CD62L (clone MEL-14), (FITC) – CD45.2 (clone 104), (APC) – CD8 (clone 53-6.7), (PE-Cy7) – MHC I (clone AF6-120.1), (PE) – CD45.1 (clone A20). All antibodies were purchased from BioLegend, Inc., BD Biosciences, or Thermo Fisher Scientific. Stained cells were analyzed with a CytoFLEX flow cytometer (Beckman Coulter) or an LSR II flow cytometer (BD Biosciences). Singlets were gated by forward scatter area (FSC-A) and forward scatter width (FSC-W), as well as by side scatter area (SSC-A) and side scatter width (SSC-W). All positive and negative populations were determined by staining on positive and negative control populations.

Quantification and statistical analysis:

Comparison of cell frequencies and protein expression in Statistical Scaffold was performed using Significance Analysis of Microarrays as described above and in Bair and Tibshirani, 2004 and Bruggner *et al*., 2014. Features with $q < 0.05$ were considered statistically significant. Comparison of bulk manually gated cell frequencies was performed using Wilcoxon rank-Sum test with Benjamini-Hochberg correction in R. Analysis of principle components for human gene expression was performed using two-sided Wilcoxon rank-sum test in R. Analysis of cell correlation with time was performed using Spearman correlation with Benjamini-Hochberg correction. All comparisons over 4T1 tumor growth were performed by one-way ANOVA with Tukey correction in Prism. Unless otherwise states, all other comparisons after infection,

treatment, or resection were made using two-sided t tests in Prism. All tests with $p < 0.05$ were considered statistically significant. Unless otherwise stated in the figure legends, n = 3 to 6 independent mice for each experimental condition.

Data availability:

All mass cytometry data are publicly available by request to the senior author without restrictions or at https://premium.cytobank.org/cytobank/projects/2433/.

Code availability:

The updated Statistical Scaffold package is available at https://github.com/SpitzerLab/statisticalScaffold.

Chapter 3 The immune macroenvironment in cancer dictates responses to PD-L1 and CD40 immunotherapies

Breanna M. Allen[1,2], Iliana Tenvooren[2], Diana M. Marquez[2], Kamir J. Hiam[1,2], and Matthew H. Spitzer[1,2]*

[1]Graduate Program in Biomedical Sciences, University of California, San Francisco, San Francisco, CA, USA

[2]Departments of Otolaryngology and Microbiology & Immunology, Helen Diller Family Comprehensive Cancer Center, Parker Institute for Cancer Immunotherapy, Chan Zuckerberg Biohub, University of California, San Francisco, San Francisco, CA, USA

*Corresponding author

3.1 Abstract

The organization and functional capacity of systemic immunity is perturbed over tumor development, yet the implications of these preexisting differences for the efficacy of immunotherapies has not been explored. Here, we investigated how cancer immune macroenvironments affect the efficacy and mechanisms of two classes of immunotherapies: PD-L1 checkpoint blockade, or agonism of the costimulatory molecule CD40. We discovered that both cancer cell type and anatomical location differentially shape the immune macroenvironment. Only cancers with preexisting peripheral immune engagement responded to PD-L1 blockade, whereas CD40 agonism overcame preexisting deficits by driving efficacious *de novo* systemic immune remodeling across cancer models. All effective immunotherapies led to systemically coordinated immune responses with convergent expansion of key effector T cell subsets, but each strategy drove nuanced phenotypic states, including terminal effector bias with combination therapy and dichotomous CD27 and CD127 expression between monotherapies. Efficacy associated with peripheral cDC behavior, and CD40 agonism massively activated and expanded both cDC1s and cDC2s in the tumor dLN. This study demonstrates that the preexisting immune macroenvironment in cancer dictates therapeutic choice in driving optimal antitumor immune responses.

3.2 Introduction

Strategies to harness immune defense mechanisms against cancer are rapidly expanding, from various checkpoint inhibitors to T cell engineering, and yet the clinical impact of immunotherapy remains limited by the inability to identify when a specific strategy will be efficacious. This gap underscores the need to identify appropriate stratification criteria to rationally choose immune interventions with the greatest potential in each patient setting. The heterogeneity in local immune responses has been well characterized[10,119–121], used to broadly stratify cancer patients across a range from immunological deserts with little to no local immune involvement, to excluded with immune recruitment but poor infiltration, to inflamed with ample immune infiltration and highest likelihood of response to checkpoint inhibitor immunotherapies[122,123]. PD-L1 expression in the tumor microenvironment (TME) is another often cited stratification criterion[124–126], where more local expression suggests heavy tumor reliance on this mode of immune disengagement and thus greater susceptibility to blockade. There has also been extensive work to describe local immune remodeling during successful immunotherapy[127]. While the clinical focus remains largely on the TME, an appreciation is growing for the importance of peripheral immune engagement in productive antitumor responses.

Numerous studies of late demonstrate that peripheral immune involvement is essential to immunotherapeutic efficacy in both preclinical and clinical studies. Blocking peripheral immune trafficking or otherwise impairing peripheral immune integrity abrogates the therapeutic benefit of checkpoint blockade[45,47,48]. Efficacy necessitates peripheral involvement because T cells in the TME acquire states of terminal dysfunction[56,57,128], whereas clinical responses are associated with stem-like memory T cell populations[59]. Several recent studies show that effective immunotherapies expand peripheral TCR diversity and drive new and activated T cell clones into

the TME, which recognize novel antigen targets[60–63]. Importantly, we are learning that peripheral immune signatures are in fact predictive of efficacy both prior to and during immunotherapy. Baseline TCR repertoire diversity is predictive of PD-1 and CTLA1-4 blockade efficacy in classical Hodgkin lymphoma and metastatic melanoma[29,129]. In non-small cell lung cancer patients, pre-treatment peripheral $CD8^+$ T cells levels associated with durable clinical benefit in response to checkpoint inhibitors (CPIs), with predictive power further strengthened after one round of checkpoint blockade[130]. Across cancer therapeutic strategies, the importance of peripheral immunity holds. Postoperative peripheral $CD4^+$ T cell frequencies are predictive of both recurrence free survival and favorable response to adjuvant chemotherapy in patients with colorectal cancer (CRC)[131]. These findings clearly implicate the need for systemic immune engagement for productive antitumor responses, but how different therapies achieve this across diverse cancer settings remains unclear.

Novel T cell expansion suggests that *de novo* immune responses mediate immunotherapeutic efficacy, rather than reinvigoration of existing local responses. Work primarily within the past year has identified conventional dendritic cells (cDCs) in the tumor draining lymph nodes (dLNs) as the primary mediators of checkpoint blockade efficacy[49,51–53], where they prime new T cell responses. A fundamental, yet underappreciated, limitation to generating new immune responses is the functional capacity of immunity in a tumor-burdened host. Cancer patients show disrupted peripheral immunity, including a reduction in circulating T cell frequencies and TCR repertoire diversity as well as defects in T cell and monocyte cytokine signaling compared to healthy individuals[29,132,133]. Our group recently demonstrated that tumor development significantly alters the systemic immune landscape, ultimately impacting the integrity of adaptive immune responses[132]. We found that the strong activation of antigen-presenting cells was capable of

restoring *de novo* adaptive immunity in tumor-burdened hosts, specifically via agonism of the costimulatory molecule CD40 on antigen-presenting cells. In cancer contexts resistant to checkpoint blockade, CD40 agonism is showing great promise likely via enabling cDCs[64–67], however the systemic consequences of CD40 agonism and how they bare out across different cancer settings is incompletely described. Altogether, these findings implicate the immune macroenvironment in cancer as a critical determining factor in immunotherapeutic efficacy.

Here, we build off recent discoveries noting the importance and disruption of systemic immunity in cancer by directly asking how the immune macroenvironment influences immunotherapeutic mechanisms, and thus efficacy. We show that disease context matters, where both cancer cell type and anatomical tumor location impact systemic immune remodeling. Across three distinct immune macroenvironments, we show that PD-L1 checkpoint blockade is efficacious in settings with preexisting immune involvement, while CD40 agonism drives robust systemic immune remodeling and is pan-effective. Effective antitumor immune responses were highly systemically coordinated and converged across therapies on the expansion of key effector immune populations. However, the quality of effector $CD8^+$and $CD4^+$ T cell states was dependent on the treatment condition. Finally, we show that cDC states in the dLN are associated with immunotherapeutic efficacy and that CD40 agonism dramatically elevates activation of peripheral, but not intratumoral, cDC1s and cDC2s. This study provides the first in depth assessment of the global immune consequences, across multiple contexts, of key immunotherapies either approved or in clinical trials for several human cancers. The findings build on recent literature to identify the potential predictive value of preexisting peripheral immune responses in determining the mechanisms of immunotherapeutic strategies and their effect on disease outcome.

3.3 Results

3.3.1 Cancer context dictates remodeling of the systemic immune macroenvironment

We previously showed that the systemic immune state is disrupted with cancer development, and that immune changes were distinct across tumor models. To understand the consequence of the immune macroenvironment on immunotherapies, we investigated the commonly studied and treatment-responsive MC38 subcutaneous model of colon cancer and the AT3 orthotopic model of breast cancer in the mammary fat pad (Figure 3.1A). To deconvolute immune consequences due to the cancer cell type and the anatomical tumor location, we additionally explored the AT3 breast cancer cell line injected subcutaneously. These models developed at different rates, with MC38 growing the fastest and subcutaneous AT3 the slowest, though all three reached a size of 150 mm^3 by day 20 (Figure 3.1B-C). We profiled the immune macroenvironment using mass cytometry in 5 organs critical to immune responses, including the tumor, dLN, blood, spleen and bone marrow. Single $CD45^+$ cells across organs and models were clustered using the *Clara* algorithm, and clusters were classified according to their most similar canonical immune cell type (defined by manual gating), to which we refer as a "landmark reference" (Figure 3.1D). All major immune cells were captured with our pan-immune antibody panel, along with several markers of cell states and activity (Table 3.1).

We began by assessing the local and peripheral immune responses to tumor development across these three contexts. The immune composition of the TME was strikingly concordant with cancer cell type, remaining highly similar between AT3 models regardless of tumor location (Figure 3.1E-F). MC38 tumors were dominated by macrophages, with notable infiltration of effector $CD8^+$ T cells. By comparison, both subcutaneous and orthotopic AT3 tumors had greater neutrophil, cDC and NK cell infiltration. One key differentiator, orthotopic AT3 had greater

effector $CD4^+$ T cell infiltration relative to either subcutaneous tumor. The Aitchison distance measuring overall immune cell composition was significantly different between the MC38 model and the AT3 models, but not between the AT3 tumors at different sites (Figure 3.1F). We next compared peripheral immune remodeling, having previously established that breast cancer models lead to dramatic systemic immune disruption dependent on active tumor burden[132]. Indeed, orthotopic AT3 led to significant changes across the 4 peripheral sites investigated, whereas subcutaneous MC38 showed more modest changes (Figure 3.1G-H). Subcutaneous AT3 resulted in a near absence of peripheral responses aside from monocyte expansion (Figure 3.1G-H). Notably, the dLN was highly altered by orthotopic but not the subcutaneous AT3 tumors. Thus, the peripheral immune landscape was jointly dictated by the anatomical location and the cancer cell type. Overall, this setup provided a useful stratification of systemic immune remodeling, with distinct TMEs and a gradient of peripheral immune engagement spanning low (AT3 subcutaneous), moderate (MC38 subcutaneous), and high (AT3 mammary fat pad). Further, we found that peripheral immune responses were significantly more coordinated in the orthotopic AT3 and MC38 models, AT3 bearing the most connectivity, consistent with more total changed features in that model (Figure 3.1J).

Lastly, we explored the expression dynamics of the PD-1/PD-L1 checkpoint blockade pathway to assess potential model-specific susceptibility to immunotherapeutic intervention. As previously described, MC38 showed high PD-L1 expression on tumor or stromal cells, macrophages and cDCs in the TME[134], which was significantly lower for both AT3 models (Figure 3.1K). In the dLN, both MC38 and orthotopic AT3 showed elevated PD-L1 expression specifically on $CD11b^+$ cDC2s, corresponding with peripheral immune activation in these models (Figure 3.1L). MC38 showed a greater proportion of cDC1s relative to cDC2s. We next explored PD-1

expression on T cells systemically and found greater expression on $CD8^+$ T cells in the tumor, blood, and dLN in the MC38 model, and higher expression on Tregs in the orthotopic AT3 model (Figure 3.1M). Tracking with PD-L1 dynamics on cDC2s, $CD4^+$ T cells in the dLN showed higher PD-1 expression for both MC38 and orthotopic AT3. These results are particularly interesting given that the field has relied on PD-L1 expression dynamics in the tumor to predict efficacy, but our data suggest a potential role of PD-L1 blockade in affecting dLN interactions between $CD4^+$ T cells and cDC2s.

3.3.2 PD-L1 blockade and CD40 agonism show different efficacies across cancer immune macroenvironments

Recent literature supports the idea that a *de novo* immune response may be critical to driving productive anti-tumor immune responses, particularly in contexts lacking a strong pre-existing immune response. Here, we employed two immune intervention strategies: relief of immunosuppression by PD-L1 antibody inhibition, or activation of antigen-presenting cells by CD40 antibody agonism. Given that PD-L1 blockade itself does not provide a new activating signal, but rather blocks a suppressive signal, we hypothesized that PD-L1 blockade would be effective in contexts with pre-existing systemic immune activation. Indeed, PD-L1 blockade alone was sufficient to stall or slow MC38 and orthotopic AT3 tumor growth over a 7-day course of treatment; however, it failed to affect the growth of subcutaneous AT3 tumors, which induce the least peripheral immune remodeling (Figure 3.2A-B). In contrast, CD40 agonism was sufficient to stall or slow tumor growth across all three cancer contexts. Within this time window, the combination of PD-L1 blockade and CD40 agonism did not provide added therapeutic benefit over CD40 agonism alone. The delay in tumor outgrowth was sustained after cessation of treatment on

day 7, particularly for the MC38 model (Figure 3.3).

Given these distinct outcomes, we assessed global changes in the immune landscape with therapy. Broadly, effector $CD8^+$ T cells expanded in the tumor in every case of treatment efficacy, but CD40 agonism induced much greater expansion and was uniquely sufficient to significantly remodel the overall local immune composition across contexts (Figure 3.4A-C). CD40 agonism was also uniquely capable of dramatically remodeling peripheral immunity, showing large divergences in principal component (PC) space and significant changes in Aitchison compositional distance across all three settings ((Figure 3.4D-E). These results suggest that peripheral immune responses are important during productive antitumor immune responses and that CD40 agonism is sufficient to drive strong peripheral immune engagement in settings lacking a preexisting response.

3.3.3 PD-L1 blockade and CD40 agonism drive both shared and unique immune features during effective antitumor responses.

In order to shed light on the specific cellular and molecular contributions to a productive response, and why therapy fails in some settings, we investigated the systemic immune changes induced by PD-L1 blockade, CD40 agonism, or combination in depth. Our study design also allowed us probe whether distinct immunotherapeutic interventions result in similar or entirely distinct immune outcomes during a productive response.

We began by assessing immune changes unique to each monotherapy and then defined convergence between the two, with the goal of highlighting critical immune features that drive responses to immunotherapy. We summarized the total number of immune cell clusters that significantly changed across sites and models for each therapy (Figure 3.5A) and constructed a

detailed systemic map of the altered immune cell types (Figure 3.5B and Figure 3.6A-B). PD-L1 blockade uniquely changed a moderate number of immune cluster frequencies across all tissues in the MC38 model. In comparison, PD-L1 blockade only changed a few clusters in the mammary AT3 model, which had greater preexisting alterations in systemic immunity. One shared change between these two models specific to PD-L1 blockade was an increase in $Ly6C^+$ $CD127^+$ $CD62L^+$ $CD44^-$ $CD8^+$ T cells in the blood.

CD40 agonism drove dramatic systemic remodeling with many unique changes in cluster frequencies across all five tissues and in all three models, including notable expansions in circulating effector $CD4^+$ T and $CD8^+$ T cells and activated NK cells. In the subcutaneous contexts with moderate or low preexisting systemic immune changes, CD40 agonism drove between 1.5-2 fold more changes as compared to the mammary AT3 model, which already highly remodeled the systemic immune state in the absence of therapy (187 clusters for subcutaneous AT3, 233 clusters for MC38, 118 clusters for mammary AT3). Focusing in on the MC38 model, in which these therapies demonstrated the most dramatic efficacy, PD-L1 blockade and CD40 agonism each demonstrated unique systemic alterations in clusters of effector $CD8^+$ T cells, $CD4^+$ T cells, and NK cells, which largely increased with therapy (Figure 3.5B and Figure 3.7). Thus, each monotherapy was capable of driving treatment-specific effects on the systemic immune landscape, though CD40 agonism resulted in larger global changes.

In addition to their unique effects, we found multiple convergent immune cell clusters altered by both PD-L1 blockade and CD40 agonism, defined as changing in the same direction (similar) and to the same degree (converge). Unsurprisingly, intratumoral expansion of effector $CD8^+$ T cells showed convergence between therapies in both the MC38 and mammary AT3 models (Figure 3.5A-B and Figure 3.6A). This was the only locally convergent immune feature between

PD-L1 blockade and CD40 agonism in the mammary AT3 model, consistent with the critical cytotoxic functions of these cells in cancer. In the MC38 model, activated KLRG1$^+$ granzyme B$^+$ NK cell and Th1 (T-bet$^+$) CD4$^+$ T cell populations expanded intratumorally across both therapies (Figure 3.7). This model exhibits lower levels of infiltrating NK cells and effector CD4$^+$ T cells without treatment (Figure 3.1E). The tissue with the greatest number of convergent immune features between therapies in the MC38 tumor model was the blood, supporting the importance of robust peripheral immune engagement (Figure 3.5A-B).

We asked whether combination therapy resulted in additive or synergistic effects on the immune response, as quantified by changes in the abundances of immune cell clusters. Instead, we found that the majority of combination-induced changes either mimicked one or the other monotherapy, particularly CD40 agonism, or even antagonized changes that took place after monotherapy (Figure 3.5C-D and Figure 3.6C-D). In the MC38 model, combination therapy did lead to greater increases in highly active PD-1$^+$ effector CD8$^+$ T cell clusters in the tumor, which trended toward increased abundances in the blood. Interestingly, the most striking combinatorial impact was on systemic monocyte populations. Classical monocytes uniquely expand in the bone marrow, and MHC-II high monocytes (cluster m32 and a34) trended toward increased abundance in the spleen and blood after combination therapy (Figure 3.8A, B, and E). Conversely, non-classical monocytes almost completely disappeared from the blood, spleen, and bone marrow (Figure 3.8C, D, and F). Overall, combination therapy did not inherently augment the systemic immune impacts of monotherapy.

Given the robust systemic consequences of CD40 agonism, we anticipated dramatic alterations in circulating cytokine profiles to help mediate these effects. We assessed a panel of 44 cytokines in the blood and found moderate changes induced by tumor burden, but dramatic

upregulation across nearly all cytokines by CD40 agonism, which were also mimicked by combination therapy (Figure 3.9). Consistent with the significant expansion of effector T cells and NK cells in the blood, inflammatory cytokines IL-2, IFNγ, and the active heterodimer IL-12p70 were elevated by CD40 agonism across models (Figure 3.9E). PD-L1 blockade induced moderate changes across circulating cytokines in the MC38 model but showed less of an impact in the AT3 models (Figure 3.9). This careful analysis of systemic immune abundances and cytokine profiles emphasizes the dramatic ability of CD40 agonism to reorient the immune system regardless of preexisting immune activity.

3.3.4 Effective antitumor immune responses are coordinated between the tumor and periphery.

We defined which of the many systemic immune changes with immunotherapy were associated with treatment efficacy and likely critical features of a productive antitumor immune response. We rationalized that cancer cell killing requires immune cells within the tumor, so we began by correlating immune features in the tumor that significantly changed after therapy with the tumor volume at day 7 after the initiation of therapy. We focused on the MC38 model because therapy showed the most dramatic impact on tumor volume in this setting. We found mainly negative correlations between changed tumor immune clusters and end-point tumor volume across therapies, suggesting that effective therapy largely increases immune responses in the tumor (Figure 3.10A). Importantly, two effector $CD8^+$ T cell clusters, an effector $CD4^+$ T cell cluster, and an NK cell cluster showed significant associations with tumor volume in each of the three treatment settings (Figure 3.10A-B). Defining their phenotype, the effector $CD8^+$ T cell subsets showed high activation ($CD44^+$, $PD\text{-}1^+$, $CD90^+$, $Ly6C^+$), and high cytotoxicity and evidence of

ongoing or recent proliferation (granzyme B^+, $Ki67^+$). MC38 cluster number 63 (cluster m63) was more differentiated, with high CD69 and CD86 but lacking CD27, whereas cluster m67 was more memory like with high CD27 expression. The NK cell cluster m29 was terminally mature ($TCF1^-$ $CD27^-$ and $CD11b^+$) and cytotoxic ($KLRG1^+$ and granzyme $B^{+)}$, and the effector $CD4^+$ T cell cluster m73 was a proliferative Th1 subset (T-bet^+ $CD27^+$ $Ki67^+$). This result pairs with our previously described convergence results to highlight that expansion of these critical effectors is associated with tumor clearance.

We addressed how these critical tumor immune subsets associated with peripheral immune changes to understand the peripheral immune dynamics involved in the cellular network that results in productive cancer cell killing. We correlated the log2 fold change in cluster abundance in the tumor with that of the blood, spleen, lymph node, and bone marrow for monotherapies (Figure 3.10C-F), as well as combination therapy (Figure 3.11A-D). PD-L1 blockade induced immune coordination in efficacious settings between the tumor and circulating immunity in the blood and spleen. Greater coordination was driven in the MC38 context that lacked the strong preexisting coordination observed in the mammary AT3 model. CD40 agonism, and similarly combination therapy, led to dramatic coordination between the tumor and all peripheral sites. This supports a developing picture of coordinated systemic remodeling by immunotherapy, where PD-L1 blockade leads to immune effects that largely magnify the type of immune response seen at baseline, while CD40 agonism leads to robust novel immune activation networks in primary and secondary lymphoid organs in addition to immune cells trafficking through the blood.

We focused on associations between the tumor and blood because this relationship was evident across all treatments, and therapeutically informative changes in the blood carry the highest translational potential due to its accessibility in cancer patients. We found a module of

positive association containing the critical effector immune clusters in the tumor and general NK cell and effector $CD8^+$ T cell clusters as well as Th1 cluster m73 in the blood (Figure 3.10G-H and Figure 3.11E). This module also contained PD-1^+ Treg cluster m77, and MHC-II^{high} $Ly6C^+$ B cell clusters in the blood. The latter result, evident in both PD-L1 blockade and CD40 agonism, supports the notion that B cell activation may be a part of effective antitumor immune responses rather than just a consequence of systemic CD40 agonism[135]. We also observed a negative correlation between this module of immune features and MHC-II^- PD-$L1^+$ non-classical monocytes in the blood across treatments. Accordingly, these blood populations themselves correlated with therapeutic outcome by day 7 tumor volume (Figure 3.10I). Combination therapy tended to drive higher frequencies of effector T cell clusters in the blood, with significantly greater total effector $CD8^+$ T cells and trends for individual clusters. We detected similar associations between effector T cells in the tumor and circulating NK cells, effector $CD4^+$and $CD8^+$ T cells, Tregs and MHC-II^- PD-$L1^+$ non-classical monocytes in the blood in the AT3 models (Figure 3.11F-H). Taken together, these results demonstrate that productive antitumor immune responses involve coordination between peripheral immune dynamics and effector cells in the tumor.

3.3.5 Distinct immunotherapeutic strategies drive nuanced phenotypic states in $CD8^+$ T cells.

Having established that $CD8^+$ T cells are systemically altered across immunotherapies and associated with therapy outcome, we further interrogated their phenotypic states to better understand whether each therapeutic condition drove activation in the same way.

As shown above, effective therapy consistently increases effector $CD8^+$ T cells in the tumor, with CD40 agonism doing so to the greatest extent and similarly expanding effectors in circulation at the expense of naïve subsets (Figure 3.12A-B). However, the types of expanded clusters varied across models. Cluster m63, previously associated with efficacy, began as the most

dominant cluster in the MC38 tumor and continued as such with therapy-driven effector expansion. The AT3 models had a similar cluster a63, but also showed significant amounts of clusters a66 and a64 in the TME, expressing higher CD27 and Ki67, all of which expanded. Although CD40 agonism drove dramatic changes, each immunotherapy ultimately drove nuanced phenotypic outcomes depending on the preexisting context. Probing effector phenotype began to also expose nuance between each immune intervention, including unique features of combination therapy-induced cell states. At the bulk level, all three treatment strategies elevated granzyme B^+ effector $CD8^+$ T cells to similar degrees, but combination led to even higher numbers of $Ki67^+$ cytotoxic cells in the tumor and in circulation (Figure 3.12C-G).

To more deeply investigate changes in composition of cell states, we plotted an equivalent number of single cells from each treatment context in UMAP reduced dimensional space and noticed striking treatment-specific patterns in regional density even within clusters (Figure 3.12H and J). We capitalized on regional density to understand how different treatments influenced the relative degree of protein expression and designed a new computational strategy, Regional Enrichment Analysis. Each individual cell is classified into a treatment neighborhood based on the treatment identities of its nearest neighbors, or otherwise classified as unenriched if there are no significantly enriched treatments in the region. We tested this method on control blood $CD8^+$ T cells assessing enrichment for individual mice, as well as real treatment groups, and compared the percentage of individual cells that fell into the unenriched category to define the optimal threshold (Figure 3.13). We tested different numbers of nearest neighbors to decide on $k = 15$ as optimal. An enrichment cutoff of 8 of 15 neighbors from the same treatment identity was not only individually significant, with a p value of <0.005, but also showed the greatest difference in the percent of cells assigned to enriched communities between control data (biological replicates of

wild-type mice) and data from different treatments. This strategy resulted in 14% of cells from control samples, but 72% of cells from immunotherapy-treated mice assigned to enriched communities, supporting the notion that treatment induced changes in protein expression profiles within $CD8^+$ T cells, even within those that are assigned to the same cluster.

Proceeding with this strategy in the MC38 model, we found that PD-L1 blockade, CD40 agonism, and especially combination therapy each resulted in unique regional enrichment of intratumoral $CD8^+$ T cells, indicating differential protein expression based on treatment (Figure 3.12I). We profiled key proteins that indicate cell state across these regions by calculating Z-scores, and indeed found several proteins with significant differences in expression between treatment enrichment groups (Figure 3.12K). $CD8^+$ T cells in regions that were enriched for untreated and PD-L1-treated mice showed higher expression of several activation markers, including CD44, PD-1, and T-Bet. PD-L1 blockade also elevated CD86 and CD90. In contrast, regions enriched for cells from anti-CD40-treated mice contained cells with significantly greater KLRG1 and less Ki67 expression, both consistent with a terminally differentiated short-lived effector cell state. Interestingly, regions enriched for cells from combination therapy were characterized by high cytotoxic protein expression of granzyme B and KLRG1 along with the proliferation marker Ki67 and a marked drop in all other activation markers. T cell memory markers also showed striking regulation by immune intervention, where PD-L1 blockade increased CD27, CD40 agonism reduced CD27 and instead increased CD127, and combination therapy dramatically reduced CD127. These features could be observed on individual clusters, including cluster m63 most abundant in the tumor (Figure 3.12L), as apparent when visualizing protein expression gradients on UMAP dimensionality reduction plots (Figure 3.12M).

Given the strong and outcome relevant associations between tumor and blood, we deployed

Regional Enrichment Analysis on circulating $CD8^+$ T cells (Figure 3.12N-P). Again, we found treatment-enriched zones largely emphasizing the shift from naïve and memory pools to effector cells, evident to some extent with PD-L1 blockade but most striking with CD40 agonism or combination therapy (Figure 3.12N-P). These differences were also evident when computing the Euclidean distance between overall expression profiles of $CD8^+$ T cells from the average cell in untreated mice (Figure 3.12Q). PD-L1 blockade elevated CD27 expression on naïve $CD8^+$ T cells as well as CD127 and CD86 expression on memory $CD8^+$ T cells, though expression of Ki67 in these cells was reduced. Memory $CD8^+$ T cells enriched for treatment with CD40 agonism alone expressed reduced levels of CD127 and elevated Ki67, potentially indicative of a shift away from a quiescent memory state. Effector cells with phenotypes enriched in the CD40 agonism group expressed lower levels of the memory marker CD27 while those enriched in the combination therapy group expressed higher levels of CD27 (Figure 3.12R-S). Both expressed higher levels of and granzyme B (Figure 3.12R-S). Cells enriched in the CD40 agonism monotherapy group also expressed more KLRG1, whereas those enriched for combination therapy expressed more PD-1 (Figure 3.12R-S).

We also studied therapy-driven regional biases in the AT3 models, and similarly found that each treatment context resulted in unique protein expression outcomes on tumor and blood $CD8^+$ T cells (Figure 3.14). Interestingly, the CD27 dynamics on tumor cells were flipped, where effector $CD8^+$ T cells enriched in the CD40 agonism group expressed higher levels while those enriched in the PD-L1 blockade group expressed lower levels. The significance of these expression patterns and whether they result in differential outcomes with longer-term therapy or disease recurrence are important areas for future investigation.

3.3.6 CD40 agonism enhances intratumoral and circulating CD4$^+$ T cell activation.

While the focus of immunotherapies has largely been on cytotoxic CD8$^+$ T cells, recent studies have led to a growing appreciation of the multifaceted role of CD4$^+$ T cells. Tumor antigen-experienced CD4$^+$ T cells from the periphery are sufficient to provide more long-term protection against rechallenge following a productive response to immunotherapy[46,66], and their TCR diversity increases locally and peripherally with effective PD-1 blockade[29]. Impressively, peripheral CD4$^+$ T cell diversity at baseline was shown to be associated with PD-1 blockade efficacy. We therefore also characterized the phenotypic state of systemic CD4$^+$ T cells during productive antitumor responses to understand and how they are shaped by different cancer contexts and immunotherapeutic interventions.

We hypothesized that CD4$^+$ T cells would show nuanced changes after therapy influenced by cancer type and the pre-existing differences in effector abundances and PD-1/PD-L1 expression dynamics in the dLN. Of note, cells with a phenotype matching the cluster of CD4$^+$ T cells that associated with outcome in the MC38 model (cluster m73; PD-1$^+$ CD27$^+$ Ki67$^+$) were significantly more prevalent in the mammary AT3 model than in either subcutaneous model without treatment (Figure 3.15A-C). CD40 agonism elevated the frequency of effector CD4$^+$ T cells in the MC38 and subcutaneous AT3 models but not in the mammary AT3 model, in which CD4$^+$ T cells were already present at a greater frequency without treatment (Figure 3.15A-B). However, PD-L1 blockade uniquely resulted in a trend toward an increase in effector CD4$^+$ T cells in mammary AT3 tumors (Figure 3.15A-B). Also unique to PD-L1 blockade, the total frequency of effector CD4$^+$ T cells in the tumor significantly correlated with the expression of PD-L1 by CD11b$^+$ cDC2s in the dLN (Figure 3.15D). In circulation, PD-L1 blockade did not dramatically alter CD4$^+$ T cell frequencies, but CD40 agonism and combination therapy resulted in dramatic increases in effector

$CD4^+$ T cells expressing PD-1 and Ki67 (Figure 3.15E-F).

Delving deeper into treatment-induced phenotypes, we again performed Regional Enrichment Analysis on $CD4^+$ T cells from the tumor and the blood. Tumor-infiltrating $CD4^+$ T cells showed phenotypic variation depending on treatment (Figure 3.15G-I). Focusing on individual clusters m72 and efficacy-associated m73, CD40 agonism or combination therapy elevated the transcription factor T-bet and proliferation marker Ki67 expression, evident of activated effector status (Figure 3.15J). Summarizing treatment enriched zones across clusters, we found more broadly that regions enriched for CD40 agonism and combination treatments contained cells expressing elevated levels of T-bet and Ki67, whereas regions enriched for PD-L1 blockade or untreated mice contained cells expressing higher levels of CD127 and TCF1 (Figure 3.15K). We calculated an overall effector $CD4^+$ T cell activation score by adding activation marker Z-scores and found that both anti-CD40 monotherapy and combination therapy drove unique $CD4^+$ T cells with higher activation across all three models (Figure 3.15L and Figure 3.16A-F).

We also observed expansion of effector $CD4^+$ T cells in the blood. $CD4^+$ T cells enriched by PD-L1 blockade expressed higher levels of $CD90^{136}$, CD69 and T-bet, leading to a modest but significant increase in $CD4^+$ T cell activation score in the MC38 model (Figure 3.15M-S). In fact, CD69 expression differentiates a unique effector $CD4^+$ T cell island enriched for PD-L1 blockade in UMAP dimensionality reduction plots (Figure 3.15N-O). In comparison, treatment with anti-CD40 or combination therapy led to a dramatic expansion in effector $CD4^+$ T cells with higher activation scores across models, driven by the expression of PD-1, Ki67, CD86, and T-bet (Figure 3.15M-S). Efficacy-associated cluster m73 occupies the UMAP region with this expression profile, which was entirely dominated by CD40 agonism or combination therapy. The marker enrichment bias across therapies was also observed in the subcutaneous AT3 model (Figure 3.16G-

N). In addition, both anti-CD40 monotherapy and combination therapy resulted in effector cells expressing higher levels of CD27 but not CD127 in both the MC38 and mammary AT3 models (Figure 3.15P, R). Effective immunotherapy clearly involves stimulation of $CD4^+$ T cells systemically, with nuance in their phenotypic characteristics according to the cancer context and type of therapeutic intervention.

3.3.7 CD40 agonism elevates peripheral but not local activation of cDC1s and cDC2s.

Dendritic cells have recently been shown to be the critical mediator of effective antitumor immune responses following PD-1/PD-L1 checkpoint blockade, specifically via interactions with T cells in the dLN[52,53]. This provides mechanistic context to our observation that PD-L1 blockade is effective in cancer settings with elevated PD-L1 expression on cDCs and PD-1 expression on T cells in the dLN. Given their essential role in orchestrating *de novo* immune responses, we expected that cDCs would also be critical mediators of the efficacy of CD40 agonism, a strategy that directly activates these antigen-presenting cells and has been shown to be sufficient for T cell priming in cancer models[66,137]. To this end, we were interested in understanding systemic cDC responses and how they differ between PD-L1 blockade and CD40 agonism across our three cancer contexts.

Because cDCs are rare cells, clustering all immune subsets above collapsed into only 1 or 2 clusters, fewer than the number of cDC subsets that are known to exist. Therefore, we clustered cDCs separately (defined as $CD11c^+$ MHC-II^+ $F4.80^{lo}$ $CD64^{lo}$) and asked how the internal composition of cDC subsets changed with therapy. We found that CD40 agonism significantly remodeled the cDC composition across models in the tumor as well as the dLN (Figure 3.17A-C), whereas PD-L1 blockade induced moderate changes. This finding presents one mechanism by which CD40 agonism may orchestrate the significant systemic expansion of $CD8^+$and $CD4^+$ T

cells. To probe this hypothesis further, we performed Regional Enrichment Analysis to assess nuances in cDC behavior, modifying the number of neighbors to account for the relative rarity of cDCs compared to T cells. Beginning with the tumor, we found a striking reduction in the abundance of cDCs with effective therapy in the MC38 model (Figure 3.17D-G), particularly $CD103^+$ cDC1s (red arrows). We followed this up by assessing absolute cell counts, and indeed found that all three therapies in the MC38 model led to significant loss of intratumoral $CD103^+$ cDC1s (Figure 3.17H). The activation score on remaining intratumoral $CD103^+$ cDC1s was not altered by any treatment, calculated by the summation of activation marker Z-scores (Figure 3.17H). Similarly, absolute cell counts of intratumoral $CD11b^+$ cDC2s decreased, significantly by PD-L1 blockade and trending by CD40 agonism, and overall activation was not significantly altered Figure 3.17I). There were variable changes in protein expression intensities within the activation profile across treatments, but most interestingly, combination therapy actually reduced CD86 and MHC-II expression on both cDC1s and cDC2s. Combination therapy additionally enriched for cDCs with lower PD-L1 expression while CD40 agonism alone enriched for higher PD-L1 (Figure 3.17E-G). Similar activation patterns were observed on cDCs in AT3 tumors, however, $CD11b^+$ cDC2s did uniquely trend toward higher activation with combination therapy for subcutaneous AT3 (Figure 3.18A-B).

Prior studies suggest that cDCs can migrate from the tumor to the dLN[46,138,139], so we next investigated cDC behavior in this secondary lymphoid organ. By regional enrichment analysis, it was immediately apparent that several regions were enriched for cells from mice that received CD40 agonism therapy (Figure 3.17J-M). Specifically, we observed the emergence of cDCs with dim but detectable CD103 and CD8 belonging to cluster m6/a6 (Figure 3.18C, Figure 3.17J-M and Figure 3.18F-M, red arrows), matching the subset that decreased in abundance in the tumor and

likely representing recent emigrants. Consistently, the absolute count of $CD103^+$ cDC1s in the dLN significantly increased with CD40 agonism or combination therapy in the MC38 model (Figure 3.17N). As observed in the tumor, the activation score was not elevated on this subset in the dLN and was actually reduced by combination therapy (Figure 3.17N). Instead, $CD8^+$ cDC1 resident to the dLN showed significant increases in both absolute cell count and expression intensities across activation and co-stimulation proteins (PD-L1, PDCA.1, Ki67, CD69, and CD86), resulting in a significantly higher activation score (Figure 3.17O). PD-L1 blockade drove a similar trend of increased $CD8^+$ cDC1 abundance and activation, suggesting importance across effective therapies. $CD11b^+$ cDC2s also increased in absolute frequency by all three therapies in the dLN of the MC38 model, although only CD40 agonism or combination therapy was able to significantly increase activation (Figure 3.17P). We again observed similar activation of cDC1s and cDC2s in the dLNs of subcutaneous AT3, whereas mammary AT3 was distinct in already driving dLN cDC2 activation at baseline (Figure 3.18N-O).

Relating these observations of dLN cDC expansion and activation to therapeutic efficacy, we found that $CD8^+$ cDC1s and $CD11b^+$ cDC2s in the dLN both significantly correlated with reduced tumor volume in the MC38 model with CD40 agonism (Figure 3.17Q). There was absolutely no correlation between outcome and $CD103^+$ or $CD11b^+$ cDC activation in the tumor. These findings demonstrate that cDC activity in the dLN, and not the tumor itself, are indicative of strong ongoing antitumor immune responses.

Inspired by the significant associations between the tumor and the blood, which also associated with therapeutic outcome, we also investigated cDCs in circulation. All three effective immunotherapeutic strategies resulted in significant remodeling of the circulating cDC composition for MC38 and mammary AT3, wheras only CD40 agonism or combination therapy

significantly altered circulating cDCs in the subcutaneous AT3 model (Figure 3.18P). More fascinating still, $CD8^+$ cDC1s in the blood were significantly activated by all three treatments in the MC38 model, and in all cases this activation was strongly associated with efficacy (Figure 3.18Q and T and Figure 3.17R). In contrast, circulating cDCs were not activated by PD-L1 blockade in the AT3 models, though they were subtly activated by CD40 agonism, resulting in higher expression of CD86, MHC-II, and Ki67 (Figure 3.18R-T). Altogether, these data reveal that effective immunotherapies drive strong cDC activation in the periphery rather than intratumorally, likely promoting the observed systemic activation of effector $CD4^+$ and $CD8^+$ T cells.

3.4 Discussion

This study provides the first in-depth assessment of systemic immune consequences driven by PD-L1 blockade, CD40 agonism, or combination therapy across three discrete cancer immune macroenvironments. We show that effective immunotherapy involves systemic immune remodeling, either preexisting or driven *de novo* by therapy, and converges on the expansion of key tumor infiltrating effector $CD8^+$ T cells, $CD4^+$ T cells, and NK cells. Importantly, we show that PD-L1 blockade is effective in contexts with an engaged immune macroenvironment, and associates with PD-L1 expression dynamics on cDCs in the dLN and not cells in the TME. CD40 agonism drives dramatic systemic immune remodeling, including the expansion and activation of both cDC1s and cDC2s in the dLN, and is more broadly effective. We also show tight associations between the tumor and circulating immune responses that also correspond with efficacy. These findings have implications for the way immunotherapy is prescribed, supporting recent evidence that the preexisting peripheral immune state can predict therapeutic outcome, and further can guide

which treatment strategy is most likely to succeed. A key future direction is to clearly define which peripheral immune responses, within broad systemic immune engagement, are essential for PD-L1 blockade efficacy and what immune contexts not explored here may impede the efficacy of CD40 agonism.

Combination therapy has been widely viewed as a promising avenue for success in patients resistant to checkpoint blockade immunotherapies[140]; however, it is becoming clear that adding multiple immune interventions is not inherently synergistic. We did not observe benefit in tumor outcome with the combination of PD-L1 blockade and CD40 agonism in these settings, which has become a theme in combination therapy clinical trials[141]. One group previously showed that combination therapy can improve efficacy against well-established tumors, but actually impairs antitumor immunity in low tumor burden settings by inducing deletion of tumor-specific T cells via over-activation and skewing the overall repertoire to lower frequency clones[142]. This argues strongly that immune interventions should be tailored to the need, which can be facilitated by using the immune macroenvironment as an indicator of ongoing immune responses. Subtyping of triple-negative breast cancer patients based on systemic immune state has proved useful[120], where systemic accumulation of neutrophils identifies a subtype resistant to checkpoint blockade and thus a case for combined approaches. Settings with a low pre-existing systemic immune response and lack of tumor immune infiltration are served by therapeutically driving strong immune responses, such as therapy-resistant and immunologically quiet pancreatic cancer. In both a preclinical model and early clinical trial, combing CD40 agonism with checkpoint blockade is showing promise[66,67]. Another application of combinatorial strategies informed by the immune macroenvironment is in late-stage disease where checkpoint blockade more often fails[143]. We previously showed that systemic immune remodeling becomes more disrupted over the course of

tumor development. Our current study assessed the immune impact in relatively early to mid-stage disease but paves the way for critical future investigation on reorienting highly disrupted systemic immunity. Future work is also needed to parse the consequences of systemic depletion of non-classical monocytes by combination therapy, observed in our study across all three models, which could include unintended disease spread in more metastatic cancer settings[144].

Understanding how different therapies drive efficacy is important to improving patient reach, and our study demonstrates that PD-L1 blockade, CD40 agonism, and their combination each lead to nuanced phenotypic T cell states. CD40 agonism or combination drove more late-stage effector states in both $CD8^+$and $CD4^+$ T cells in the tumor, but also the blood. Intratumoral CD8s were particularly stratified, where CD40 agonism drove greater KLRG1 expression on T cells than PD-L1 blockade, but combination additionally reduced several activation markers likely indicative of terminal effector status. In the $CD4^+$ T cell compartment, CD40 agonism drive more cell cycle activity, with higher Ki67 and cCaspase3 suggesting higher turnover with expansion. The magnitude of T cell activation bias with CD40 agonism, and even more so combination, may impede immune memory. The expression dichotomy of memory markers CD27 and CD127 across immunotherapies has not been previously described, but here suggests a role in supporting massive effector expansion. We showed that combination therapy uniquely and universally drove elevated CD27 and loss of CD127 expression in effector $CD4^+$ and $CD8^+$ T cells. In viral responses, CD27 was shown to compliment CD28 signaling by promoting the survival of activated T cells during successive divisions[145]. Both CD27 and CD127 expression identify cells that can give rise to long-term memory[146,147], but loss of CD127 specifically was shown to define functional effector $CD8^+$ T cells in HIV-infected individuals[148]. We also found an interesting but context dependent regulation of CD27 by monotherapies, where PD-L1 blockade increased and CD40 agonism

decreased CD27 expression in the MC38 model. A study showed that CD27 stimulation supports cytotoxic T cell responses by enhancing $CD4^+$ T cell help, where CD27 agonism alone or paired with PD-1 blockade improved vaccine efficacy against human papillomavirus–expressing tumors[149]. We found the opposite monotherapy impact in the AT3 models, with CD40 instead elevating CD27, suggesting that the precise mechanisms at play during productive response depend on the entire immune context. Thus, the type of immunotherapeutic strategy deployed skews antitumor responses in the balance between strong immediate cytotoxicity and long-term memory potential. Studies to follow should include temporal analysis of T cell states over long-term therapeutic interventions and investigate resulting memory capacity with rechallenge or metastatic spread.

Finally, our work supports recent studies implicating conventional dendritic cell activity in tumor dLNs as the critical orchestrator of productive antitumor immunity. Conventional DC function is impaired by tumor burden, with perturbed development and deficits in tumor infiltration impeding the productive priming of new T cell responses[20,26,150]. Immunotherapies drive efficacy when they promote *de novo* immune activation beginning with cDCs. Multiple groups recently showed that cDCs in the dLN were the critical mediators of checkpoint blockade efficacy[52,53], which culminates in the systemic expansion of new T cell clones and unique antigen specifies[29,60–62]. Here, we show preexisting PD-L1 elevation on cDCs in the dLN of cancer models that respond to PD-L1 blockade, and significant associations between efficacy and dLN cDC activation. Importantly, we found no associations between efficacy and intratumoral PD-L1 expression or cDC activation, exposing an inherent weakness in the common use of tumor checkpoint expression as a stratification criterion for checkpoint blockade success. We do show that circulating cDC1 activation may be a viable and accessible indicator of ongoing efficacy

across therapies, which warrants follow-up in clinical samples. A recent study demonstrated that migratory cDCs transfer tumor antigen to dLN resident cDCs, which then carry out T cell priming functions[139], a dynamic supported by our finding that resident cDCs in the dLN and not immigrating $CD103^+$ subsets were highly activated by CD40 agonism. Successful antitumor responses are highly collaborative and systemic in nature, and recent discoveries indicate a shift in priority from reinvigoration to *de novo* activation. We expect that targeted DC interventions will become an essential element of next generation immunotherapies.

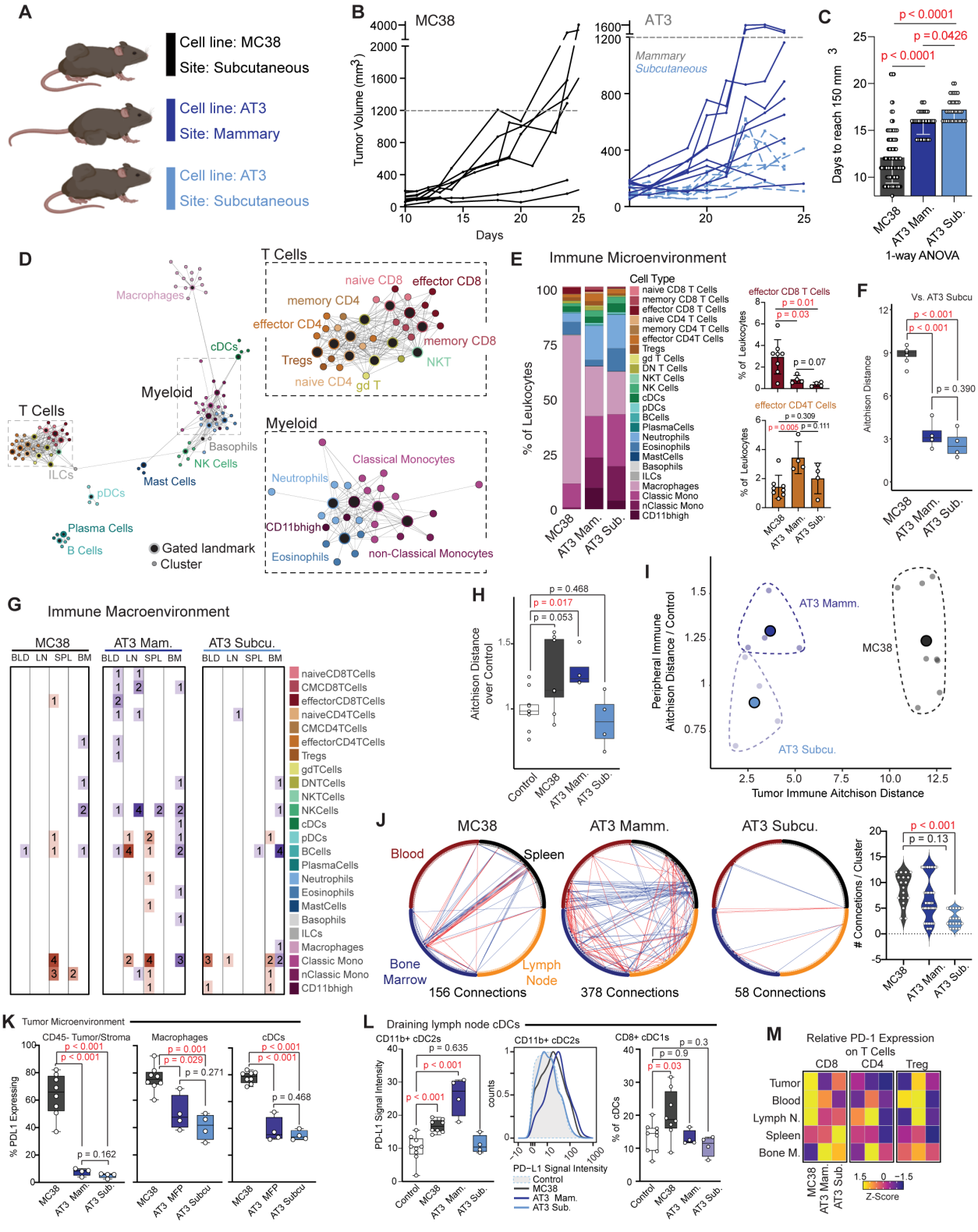

Figure 3.1: Cancer cell type and anatomical location dictate the immune macroenvironment in cancer.

A, Cancer models seeded by direct injection into the target site. B, Tumor growth curves after

cancer cell injection for subcutaneous MC38 (left) and mammary fat pad AT3 or subcutaneous AT3 (right). **C**, Number of days to reach ~150 mm^3, the designated size for treatment start. **D**, Force-directed map of immune clusters representing the systemic immune landscape, constructed from clusters in the MC38 model but with corresponding clusters in the AT3 datasets. **E**, Stacked frequencies of clusters in the tumor, collapsed by major immune landmarks (left) and highlighted frequencies of all effector $CD8^+$and $CD4^+$ T cell clusters (right); p values calculated by two-tailed t-test. **F**, Aitchison distance of the tumor immune composition between the MC38 model and each AT3 model; p values calculated by two-tailed t-test. **G**, Map summarizing the number of significantly changed clusters binned by major landmark across the blood, tumor dLN, spleen, and bone marrow in each model, increasing in the first column (red) and decreasing in the second column (blue) for each organ; $p < 0.05$, significance analysis of microarrays (SAM). **H**, Aitchison distance of the peripheral immune composition between control animals and tumor burdened animals; p values calculated by two-tailed t-test. **I**, Summary of local and peripheral immune compositional distance, stratifying the immune macroenvironments of the three models. **J**, Systemic correlation networks connecting clusters significantly changed from control, showing positive correlations (red) and negative correlations (blue) of log2 fold change from control between organs; p values <0.05, spearman correlation. The number of correlations per cluster is plotted on the right; p values calculated by Wilcoxon rank-sum test. **K**, Percent of PD-L1 expressing cells in the tumor; by two-tailed t-test. L, PD-L1 signaling intensity on $CD11b^+$ cDC2s and percent of $CD8^+$ cDC1s in the dLN; by two-tailed t-test. **M**, Z-scores of relative PD-1 expression across models on T cells in the tumor and each immune organ.

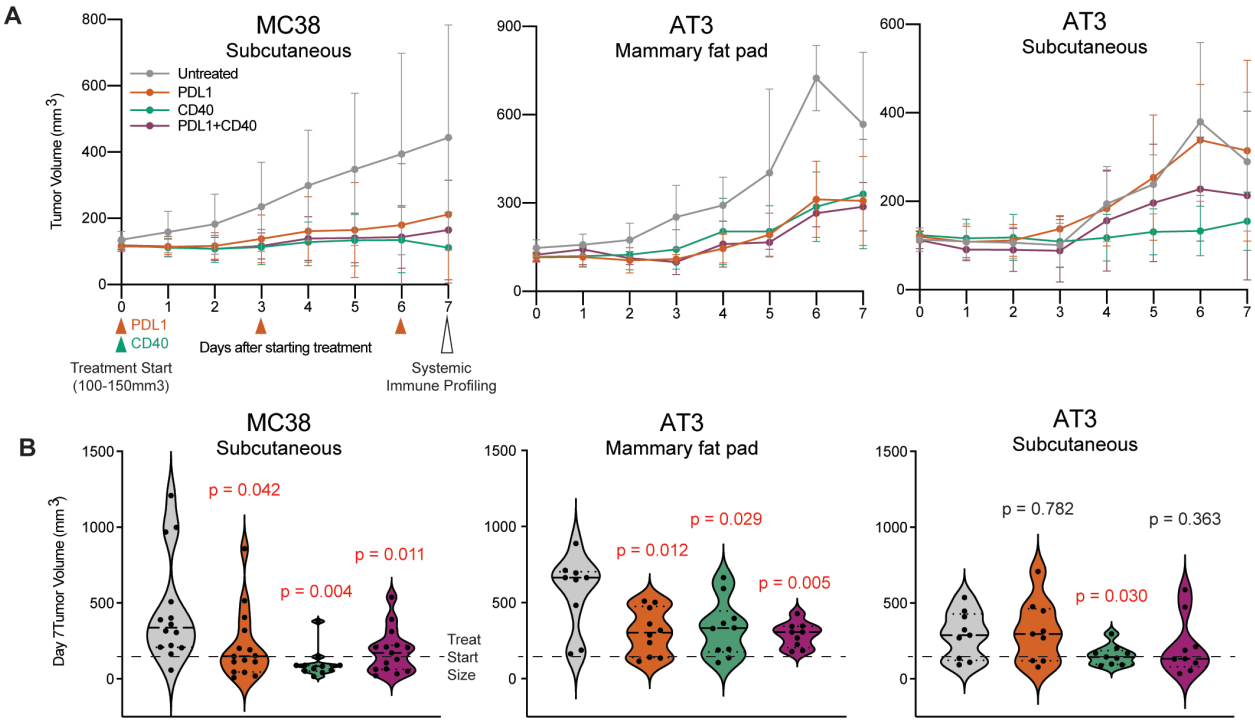

Figure 3.2: CD40 agonism is pan-effective, but PD-L1 blockade efficacy is context-dependent
A, Tumor growth curves over a 7-day course of PD-L1 blockade, CD40 agonism, combination or no immunotherapy. **B**, Day 7 tumor volume across treatment groups for each model; p values calculated by two-tailed t-test.

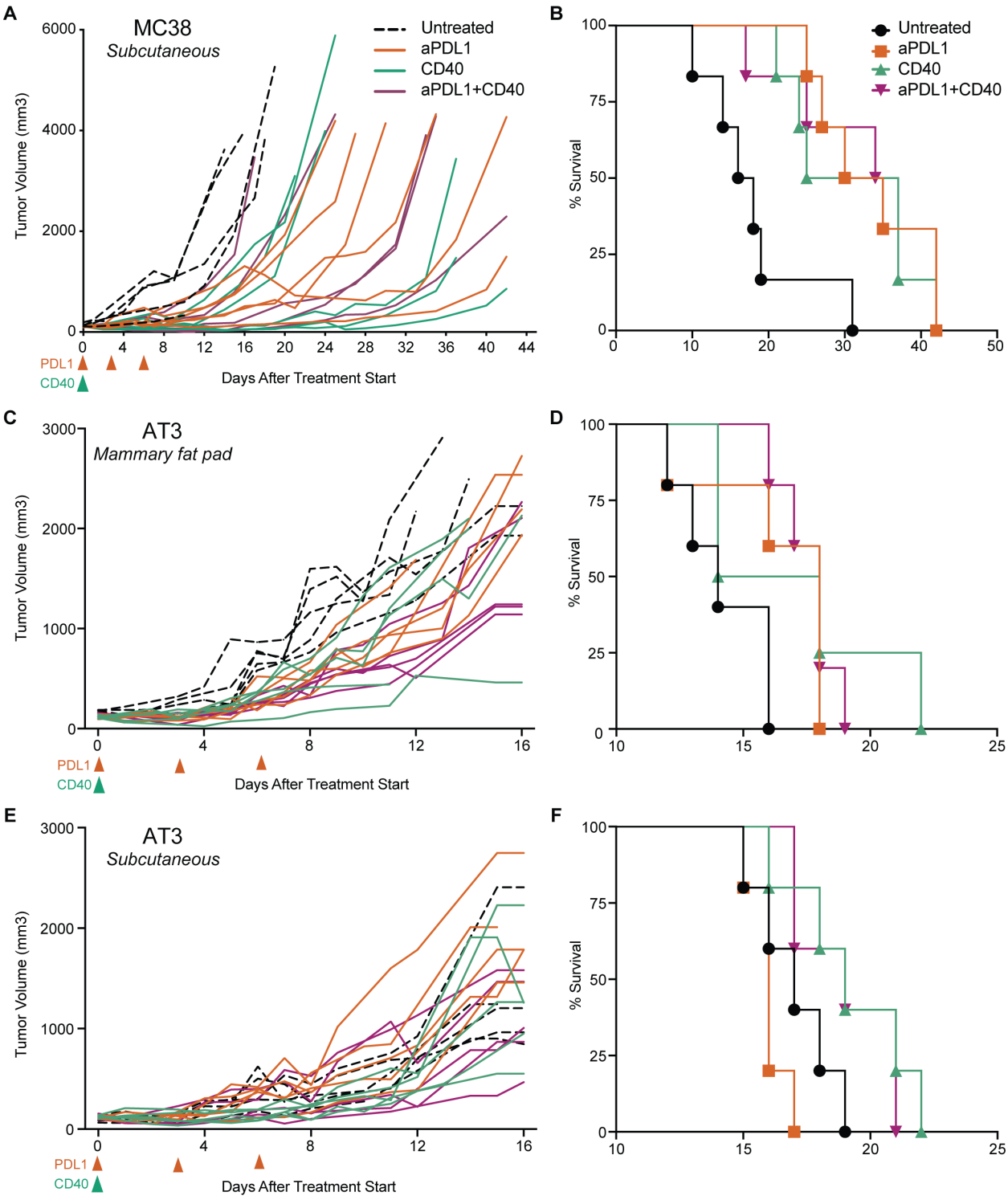

Figure 3.3: Long-term tumor growth responses to immunotherapy in each model.
A-F, Tumor volume growth curves and survival after a 7-day window of PD-L1 blockade, CD40 agonism or combination immunotherapy in subcutaneous MC38 (**A-B**), mammary AT3 (**C-D**), or subcutaneous AT3 (**E-F**) tumor models.

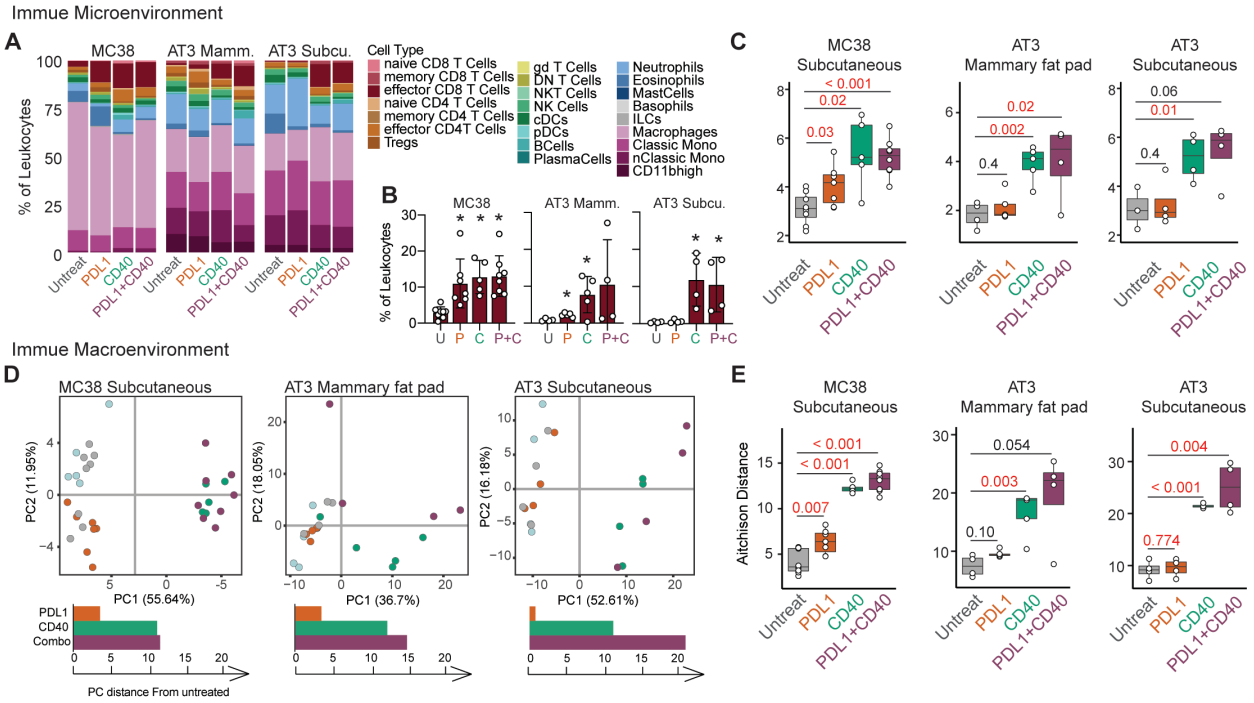

Figure 3.4: PD-L1 blockade operates within preexisting immune responses while CD40 agonism drives systemic immune remodeling.

A, Stacked frequencies of clusters in the tumor, collapsed by major immune landmarks, with treatment for each model. **D**, Highlighted frequencies of all effector $CD8^+$ T cell clusters with treatment for each model; $p < 0.05$, two-tailed t-test. **C**, Aitchison distance of the tumor immune composition with treatment for each model; p values calculated by two-tailed t-test. **D**, Principal component analysis of the center-log-ratio of peripheral immune frequencies with treatment for each model, with average Euclidean distance in PC space shown below. **E**, Aitchison distance of the peripheral immune composition with treatment for each model; p values calculated by two-tailed t-test.

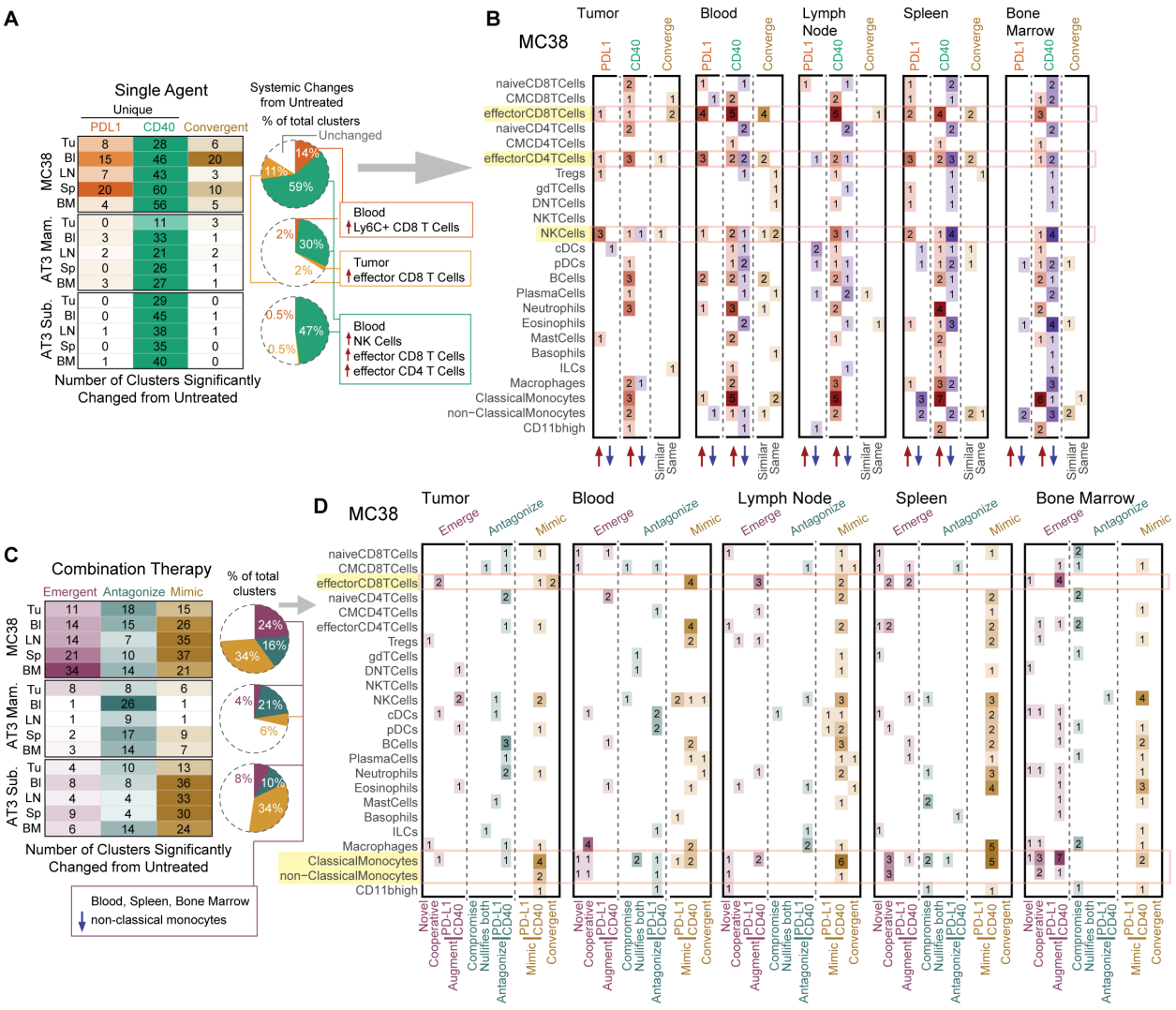

Figure 3.5: Effective PD-L1 and CD40 interventions drive both unique and shared systemic immune responses.

A, Summary of the number of clusters significantly changed with treatment that were unique to PD-L1 blockade, unique to CD40 agonism, or convergent and taking place with both monotherapies, across models. The total frequency of clusters falling into each category is summarized on the right with callouts of overlapping changes; p <0.05, SAM. B, Map summarizing the number of clusters significantly changed with treatment in the MC38 model, falling into each unique or convergent category and binned by major landmark across immune organs; increasing in the first column (red) and decreasing in the second column (blue), or changed in either direction but similar or statistically the same between monotherapies (gold). C, Summary of the number of clusters significantly changed with combination treatment that were unique, and antagonized or mimicked changes induce by monotherapies, across models. The total frequency of clusters falling into each category is summarized on the right with a callout of overlapping change. D, Map summarizing the number of clusters significantly changed with combination therapy in the MC38 model, falling into each emergent (purple), antagonistic (green), or mimetic (gold) category and binned by major landmark across immune organs; p <0.05, SAM.

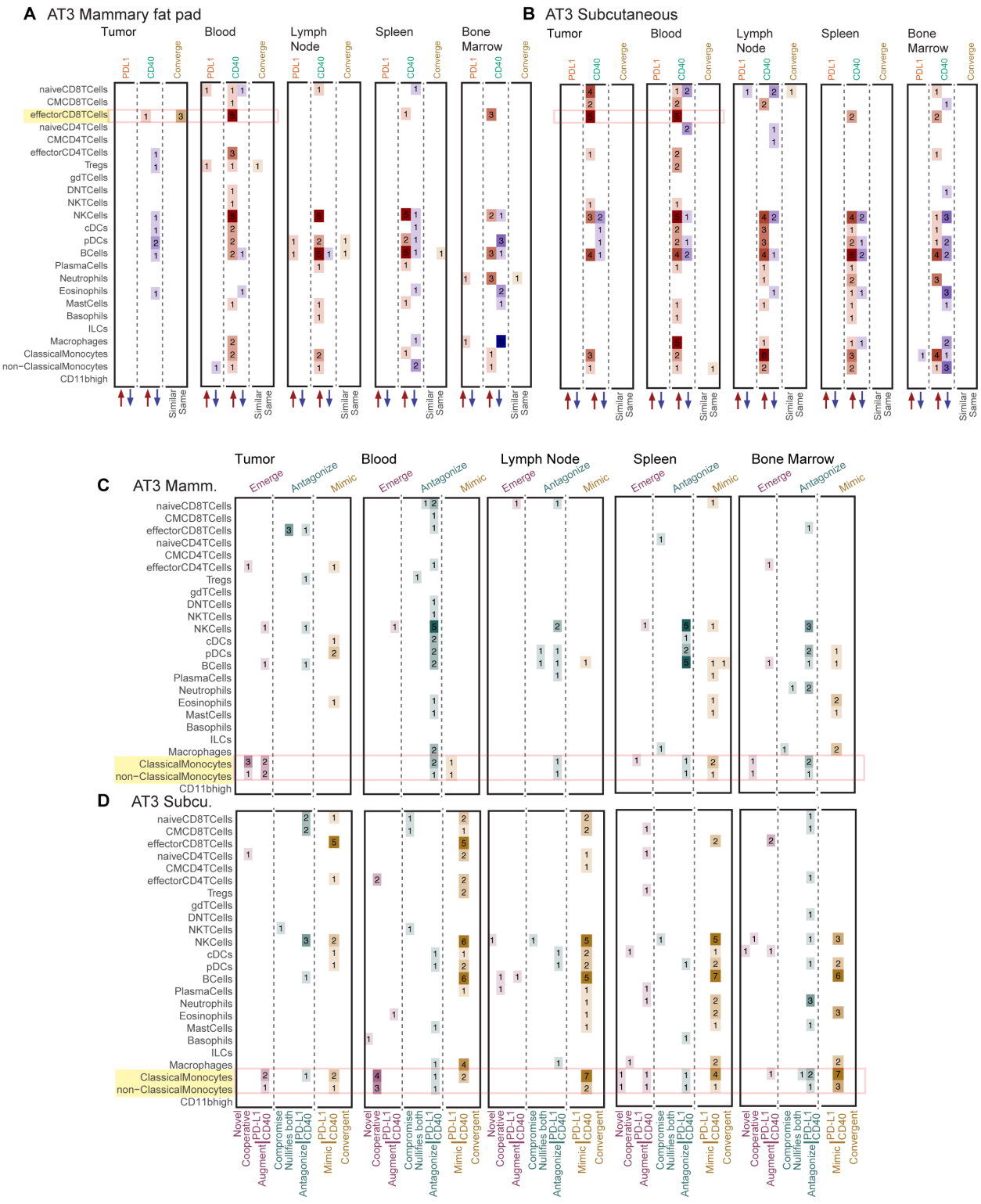

Figure 3.6: Convergent and emergent systemic immune features with single or combination therapies in AT3 models.

A-B, Map summarizing the number of clusters significantly changed with treatment in the mammary AT3 (A) or subcutaneous AT3 (B) models, falling into each unique or convergent

category and binned by major landmark across immune organs; increasing in the first column (red) and decreasing in the second column (blue), or changed in either direction but similar or statistically the same between monotherapies (gold); $p < 0.05$, SAM. C-D, Map summarizing the number of clusters significantly changed with combination therapy in the mammary AT3 (C) or subcutaneous AT3 (D) models, falling into each emergent (purple), antagonistic (green), or mimetic (gold) category and binned by major landmark across immune organs; $p < 0.05$, SAM.

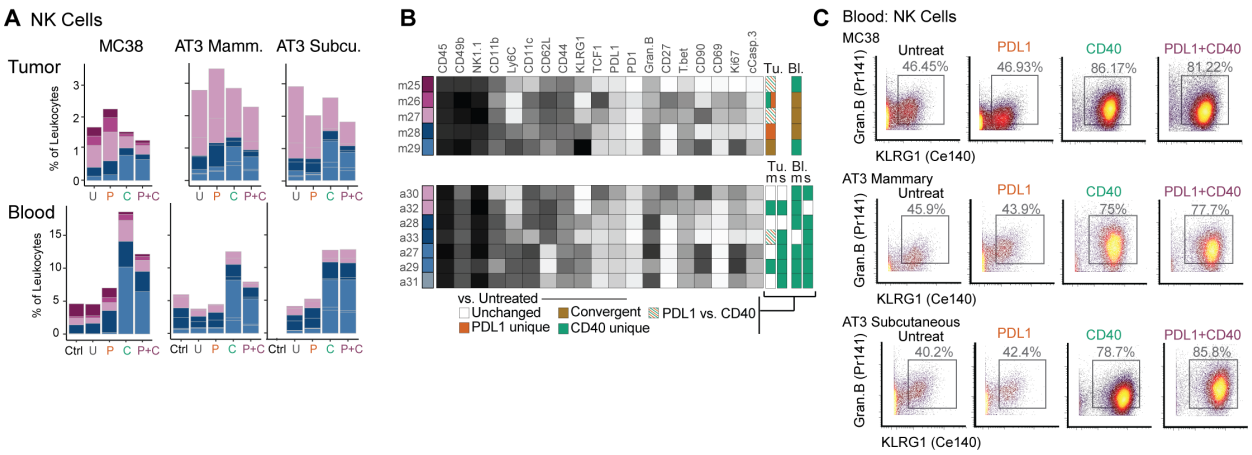

Figure 3.7: Activated NK cell expansion with immunotherapy in the tumor and blood.
A, NK cell cluster frequencies as a percent of total leukocytes for the tumor and blood with treatment across models. **B**, Cluster protein expression identities across NK cell clusters. Significant clusters are indicated on the right, color by uniqueness or convergence between monotherapies as described in Figure 3.5. **C**, Representative scatter plots of KLRG1 and granzyme B expression on NK cells in the blood across models.

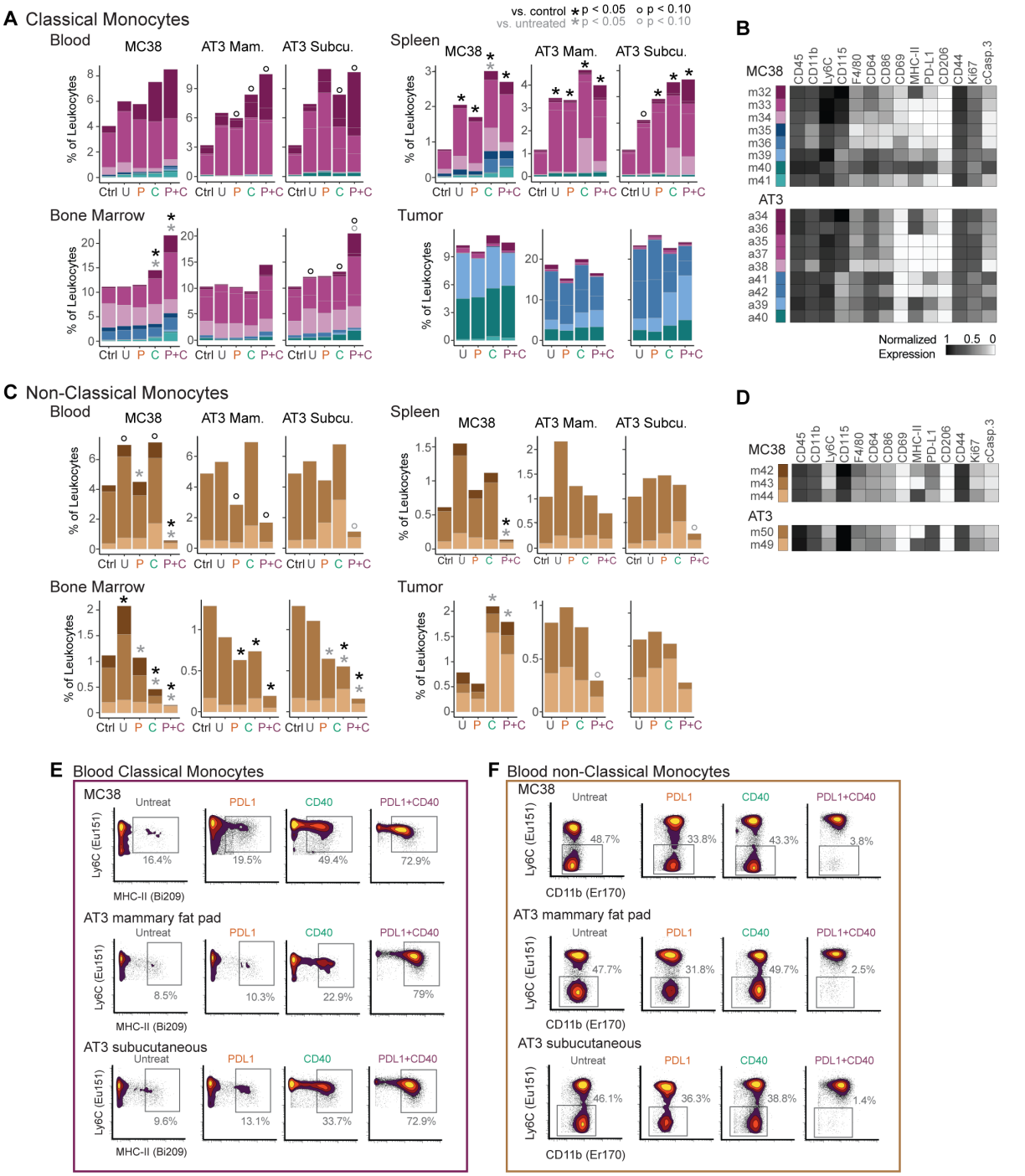

Figure 3.8: Combination therapy reorganizes systemic monocyte abundances.
A-D, Classicalal monocyte (**A-B**) and non-classical monocyte (**C-D**) cluster frequencies as a percent of total leukocytes for the blood, spleen, bone marrow and tumor with treatment across models, and the corresponding protein expression identities across clusters; $p < 0.05$ or $p < 0.1$ as indicated against control (black) or untreated tumor-bearing (grey), Wilcoxon rank-sum test. **E**, Representative density plots of Ly6C and MHC-II expression on classical monocytes in the blood across models. **F**, Representative density plots of Ly6C and CD11b expression on monocytes in the blood across models.

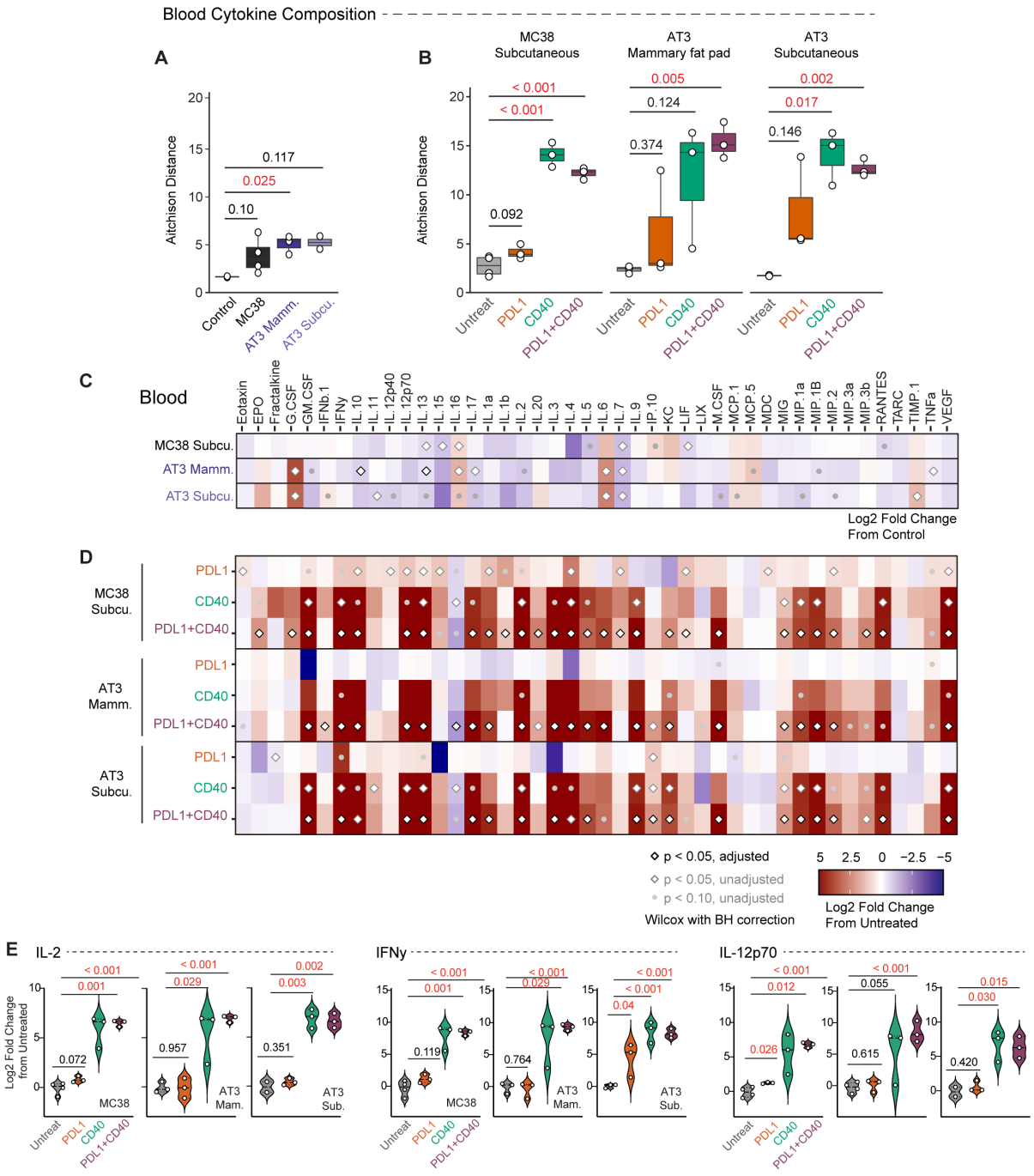

Figure 3.9: CD40 agonism elevates a variety of cytokines in circulation.
A, Aitchison distance between circulating cytokine levels across models; p values calculated by Wilcoxon rank-sum test. **B**, Aitchison distance between circulating cytokine levels across treatments in each model; p values calculated by Wilcoxon rank-sum test. **C-D**, Heatmap of cytokine log2 fold changes between untreated and control (**C**) or between untreated and treated (**D**) for each model; p values calculated by Wilcoxon rank-sum test with or without benjamini Hochberg correction. **E**, Log2 fold change in circulating abundance of specific pro-inflammatory cytokines IL-2, IFNγ, and IL-12p70 with treatment in all three models; p values calculated by two-

tailed t-test.

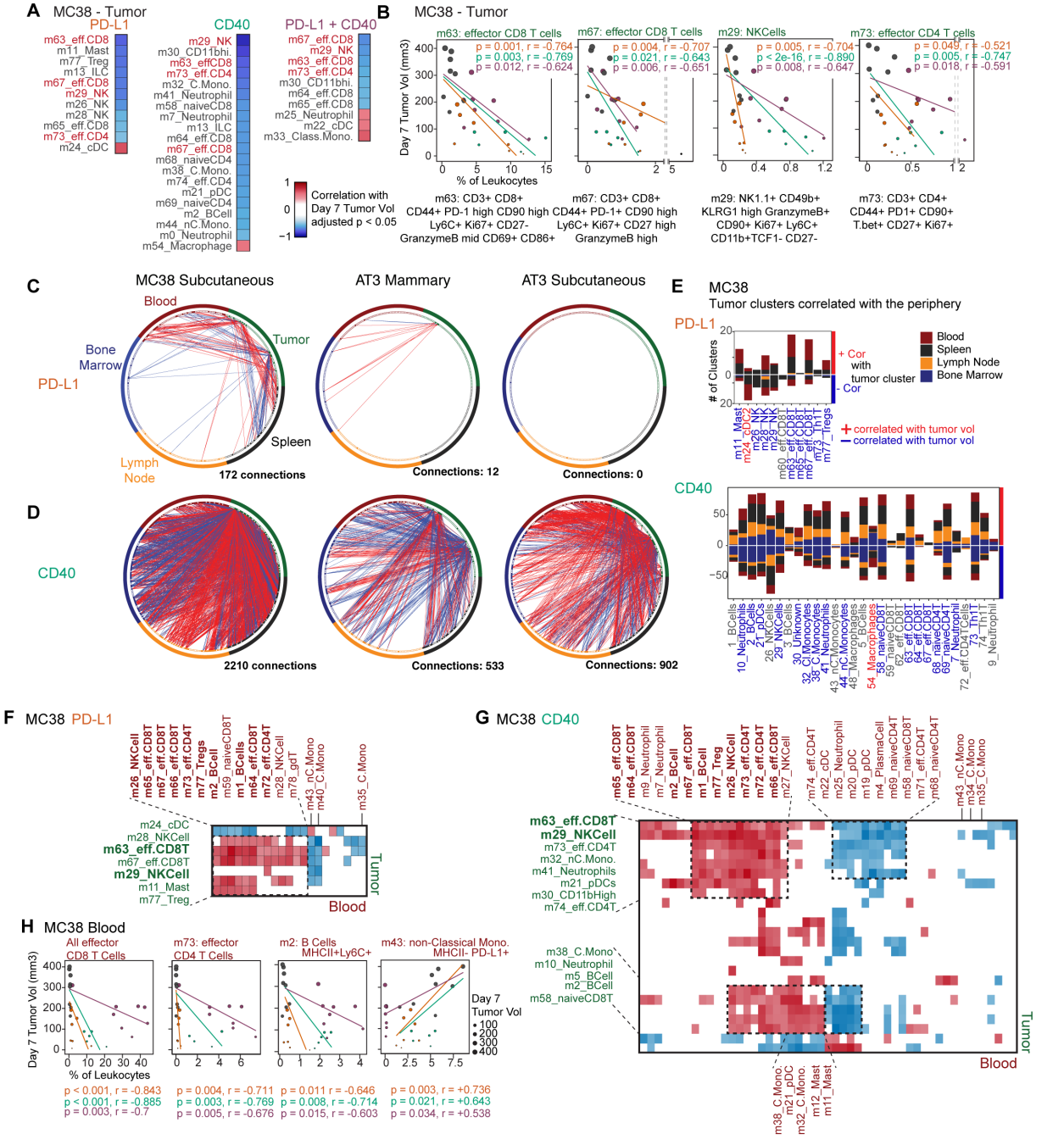

Figure 3.10: Effective immunotherapies drive coordination of immune responses between the tumor and periphery.

A, Immune clusters changed in the tumor with treatment and significantly correlated with day 7 tumor volume in the MC38 model; p values <0.05, spearman correlation. **B**, Immune clusters in the tumor significantly associated with day 7 tumor volume for all three therapies in the MC38 model. **C-D**, Correlation networks connecting clusters between the tumor and peripheral immune organs that are significantly changed with PD-L1 blockade (**C**) or CD40 agonism (D) and show positive correlations (red) or negative correlations (blue) of log2 fold changes from untreated; p

<0.05, spearman correlation. **E**, Number of clusters colored by organ across specific MC38 tumor immune clusters, corresponding with networks in **C** and **D**. **F-G**, Heatmap of cluster correlations between the tumor and blood of MC38 tumor-bearing animals after PD-L1 blockade (**F**) or CD40 agonism (**G**), with callout to specific positive and negative correlation modules. **H**, Day 7 tumor volume by immune cluster frequencies in the blood identified in correlation modules in **F** and **G**, of MC38 tumor-bearing animals.

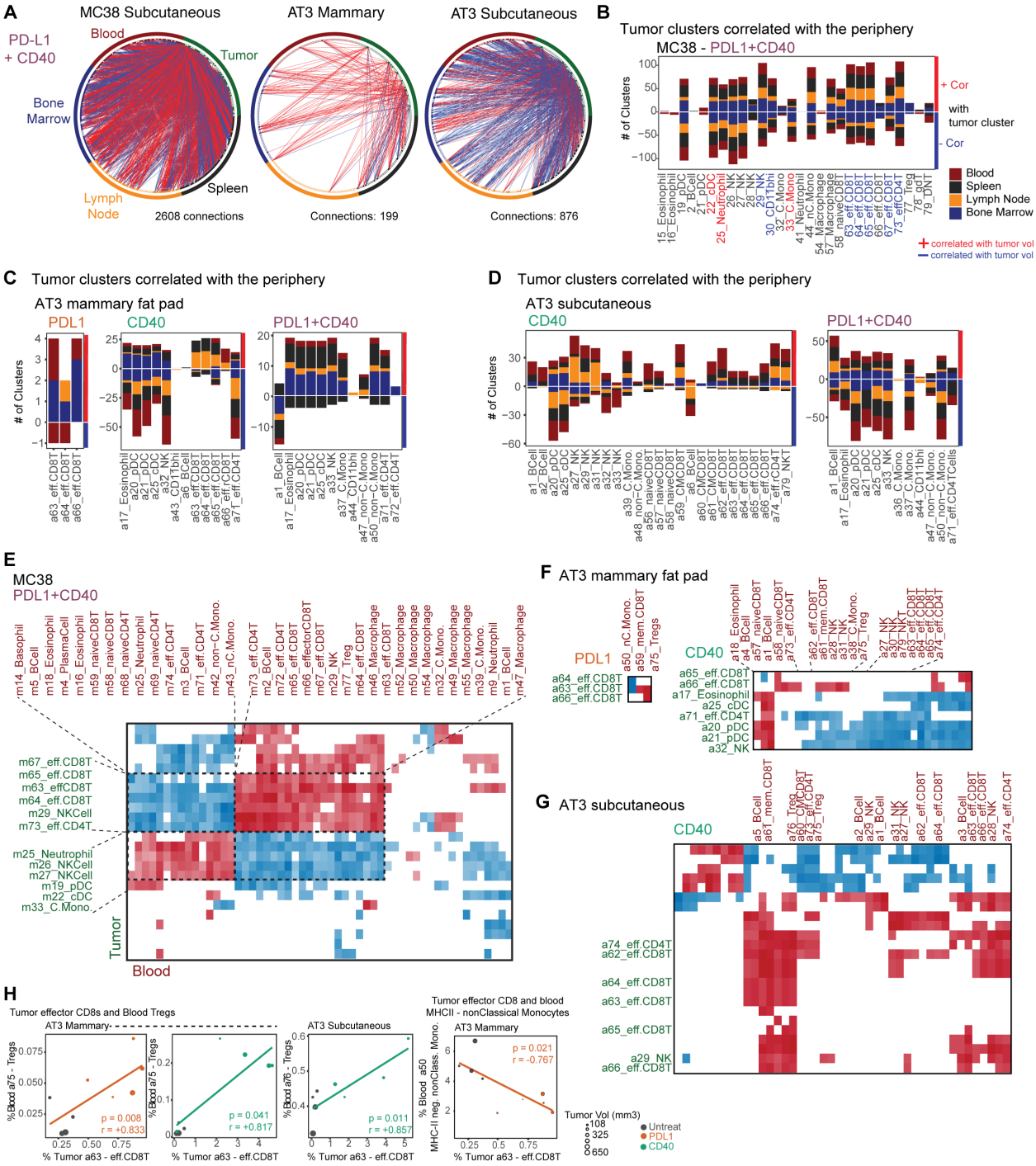

Figure 3.11: Systemic immune responses are coordinated across models with effective therapy.

A, Correlation networks connecting clusters between the tumor and peripheral immune organs that are significantly changed with combination PD-L1 blockade and CD40 agonism, showing positive correlations (red) or negative correlations (blue) of log2 fold changes from untreated; p <0.05, spearman correlation. **B-D**, Number of clusters colored by organ across specific tumor immune clusters for combination therapy in MC38 (**B**), monotherapies or combination in mammary AT3

(**C**) and CD40 agonism or combination in subcutaneous AT3 (**D**). **E-G** Heatmaps of cluster correlations between the tumor and blood after combination therapy in MC38 (**E**) monotherapies or combination in mammary AT3 (**F**), or CD40 agonism in subcutaneous AT3 (**G**) with callout to specific positive and negative correlation modules; $p < 0.05$, spearman correlation. **H**, Correlation scatterplots of immune cluster frequencies in the tumor and blood identified in **F** and **G**, for mammary or subcutaneous AT3 tumor-bearing animals; spearman.

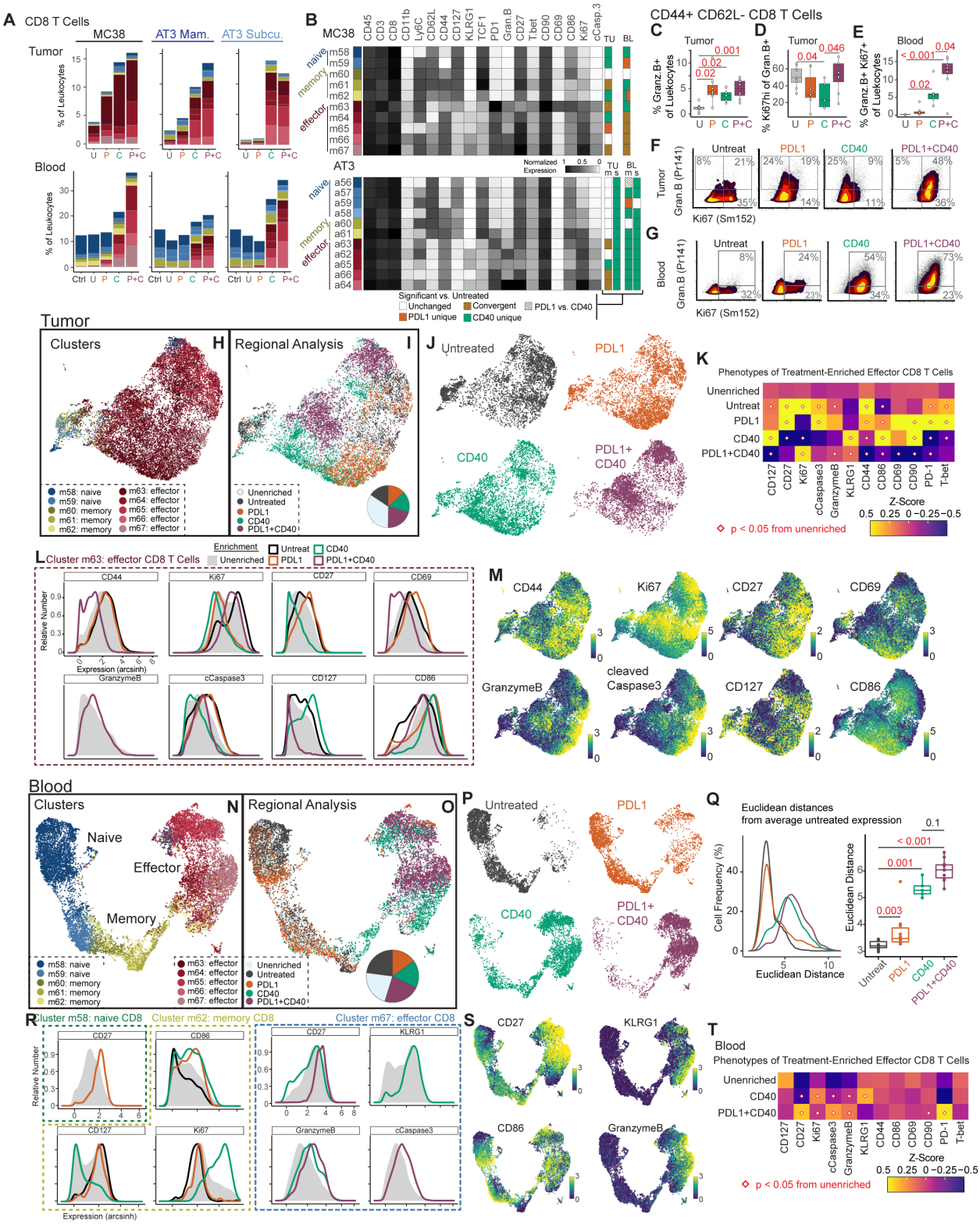

Figure 3.12: Immunotherapies drive nuanced phenotypic states in systemically expanding effector CD8⁺ T cells.

A, CD8⁺ T cell cluster frequencies as a percent of total leukocytes for the tumor and blood with

treatment across models. **B**, Cluster protein expression identities across naïve, memory, and effector subsets. Significant clusters are indicated on the right, color by uniqueness or convergence between monotherapies as described in Figure 3.5. **C-E**, Ki67 and granzyme B expression on effector $CD8^+$ T cells in the tumor (**C-D**) and the blood (**E**). Representative density plots of Ki67 and granzyme B expression on effector $CD8^+$ T cells in the tumor (**F**) and blood (**G**). **H**, UMAP of single $CD8^+$ T cells in MC38 tumor colored by cluster, subsetted to consistent number of total $CD8^+$ T cells per treatment condition to represent internal composition. **I**, Regional Enrichment Analysis on MC38 tumor $CD8^+$ T cells, with an inset of frequency for each enrichment category. **J**, UMAPs of MC38 tumor $CD8^+$ T cells for each treatment condition. **K**, Heatmap of relative expression of key memory and activation proteins on effector $CD8^+$ T cells across enrichment regions; $p < 0.05$, SAM. **L**, Histograms of significantly distinct protein expression in enrichment regions for cluster m63 in the MC38 tumor; $p < 0.05$, SAM. **M**, UMAPs of $CD8^+$ T cells in the MC38 tumor colored by protein expression intensity. **N-P**, Blood $CD8^+$ T cell UMAP and Regional Enrichment Analysis colored by cluster (**N**), enrichment category (**O**), or each treatment condition (**P**). **Q**, Euclidean distance between blood $CD8^+$ T cell protein expression profiles across treatments. **R-T**, Enriched region protein expression differences, shown by histograms in specific clusters (**R**), UMAPs colored by protein expression intensity (**S**), and heatmap of relative memory and activation protein expression on effector $CD8^+$ T cells across enriched regions; $p < 0.05$, SAM.

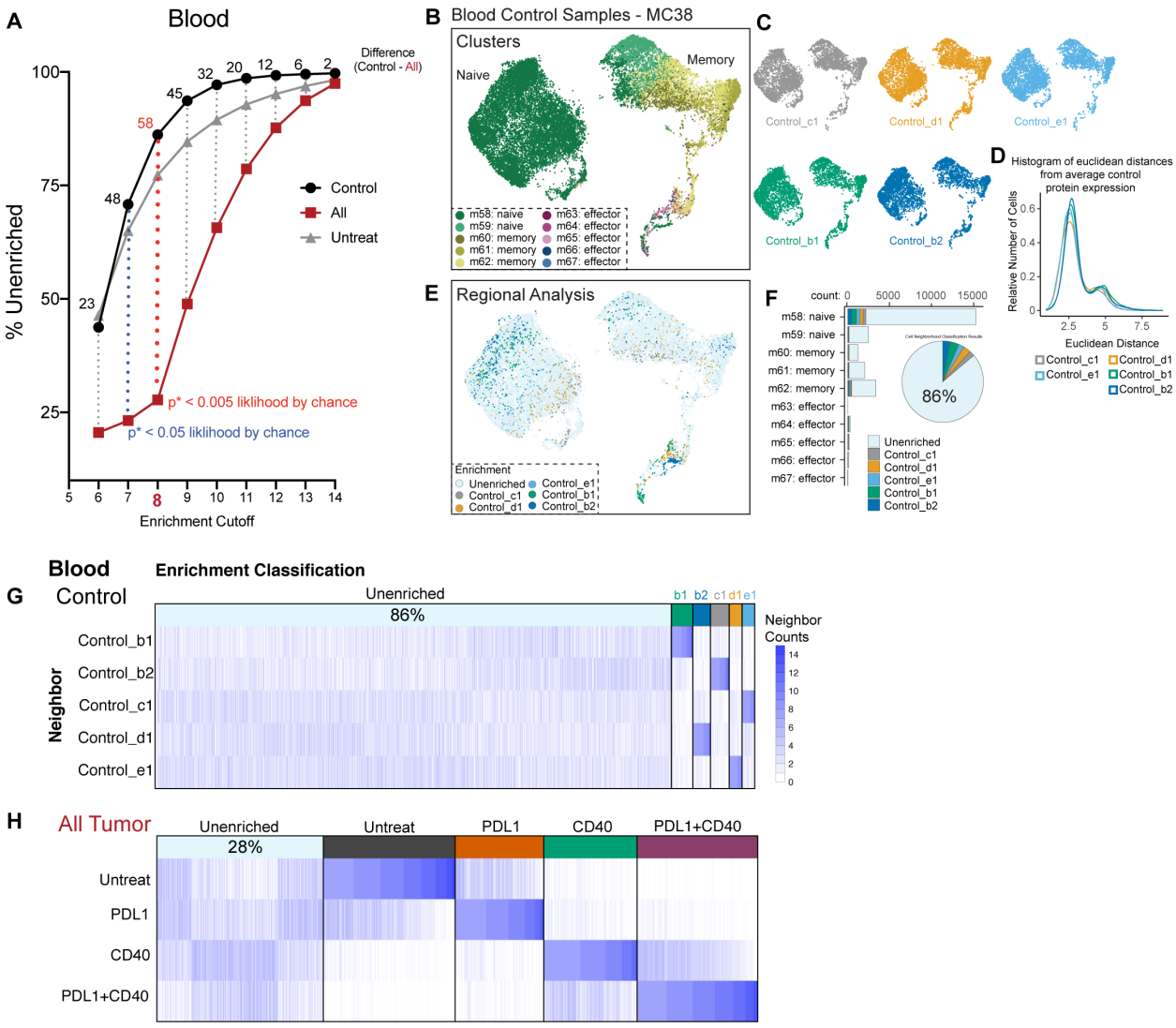

Figure 3.13: Benchmarking Regional Enrichment Analysis on control CD8$^+$ T cells.
A, Percent of total cells categorized as unenriched after Regional Enrichment Analysis of blood CD8$^+$ T cells across independent control animals (black) untreated animals (grey) or across all treated tumor-bearing conditions (red) for each enrichment cutoff, out of 15 nearest neighbors. B-C, UMAPs of blood CD8$^+$ T cells in control animals colored by cluster (B) or individual animal (C). D, Euclidean distance between blood CD8$^+$ T cell expression profiles across control animals. E, UMAP colored by enrichment category. F, Distribution of enrichment categories across clusters. G-H, Map of neighborhood barcodes falling into each enrichment category for control animals (G) or all treated tumor-bearing conditions (H).

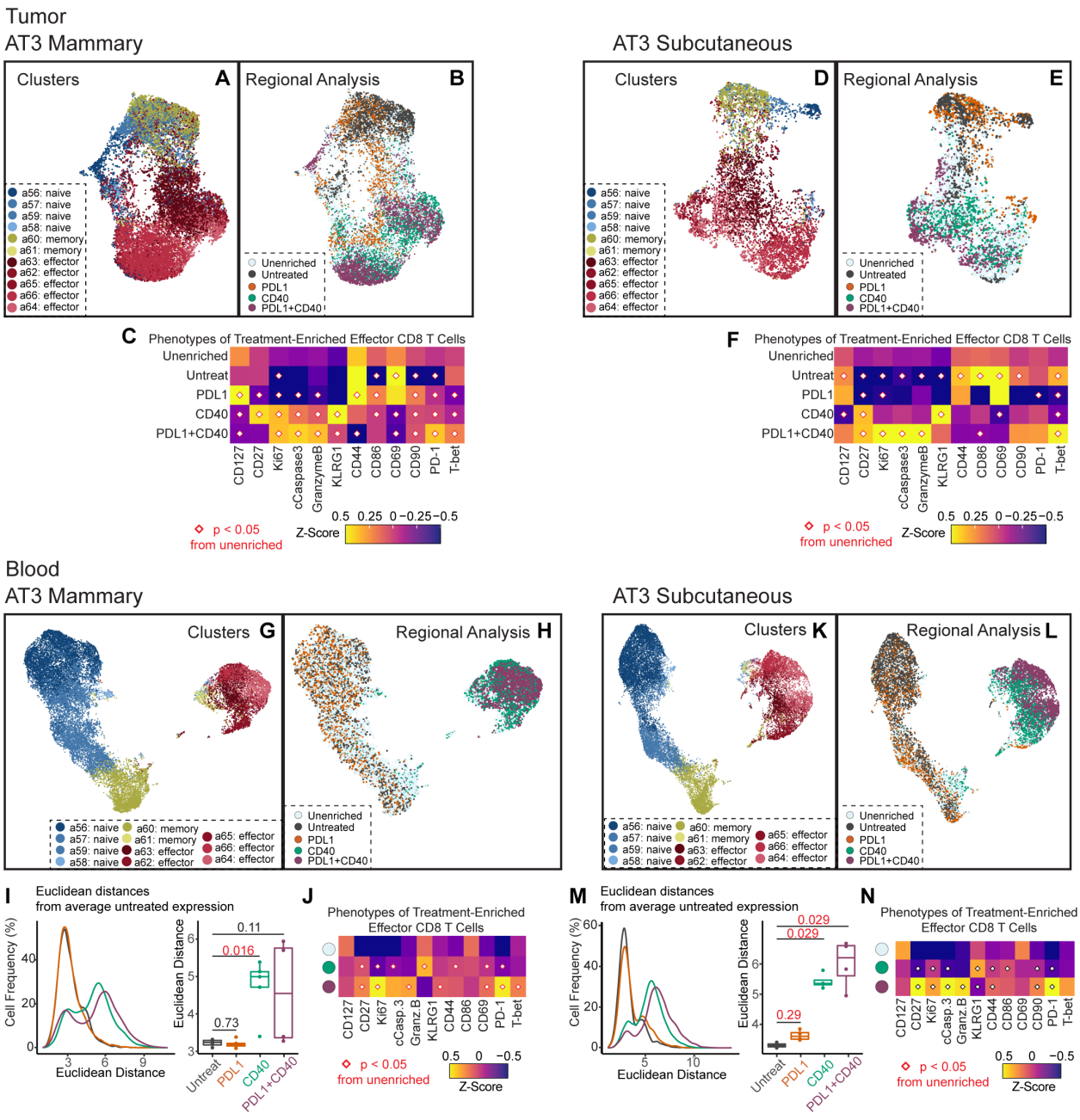

Figure 3.14: CD8⁺ T cells acquire different phenotypic states based on immunotherapy in AT3 cancer models.

A-F, UMAPs of tumor CD8⁺ T cells colored by cluster (**A** and **D**) or Regional Enrichment Analysis (**B** and **E**), and relative memory or activation marker expressions for each enrichment category on effector CD8⁺ T cells (**C** and **F**) for mammary or subcutaneous AT3. **G-J**, UMAPs of blood CD8⁺ T cells colored by cluster (**G** and **K**) or Regional Enrichment Analysis (**H** and **L**), Euclidean distance between blood CD8⁺ T cell expression profiles across treatments (**I** and **M**), and relative memory or activation marker expressions for each enrichment category on effector CD8⁺ T cells (**J** and **N**) for mammary or subcutaneous AT3; $p < 0.05$, by Wilcoxon rank-sum test in **I** and **M** or by SAM in **C,F, J**, and **N**.

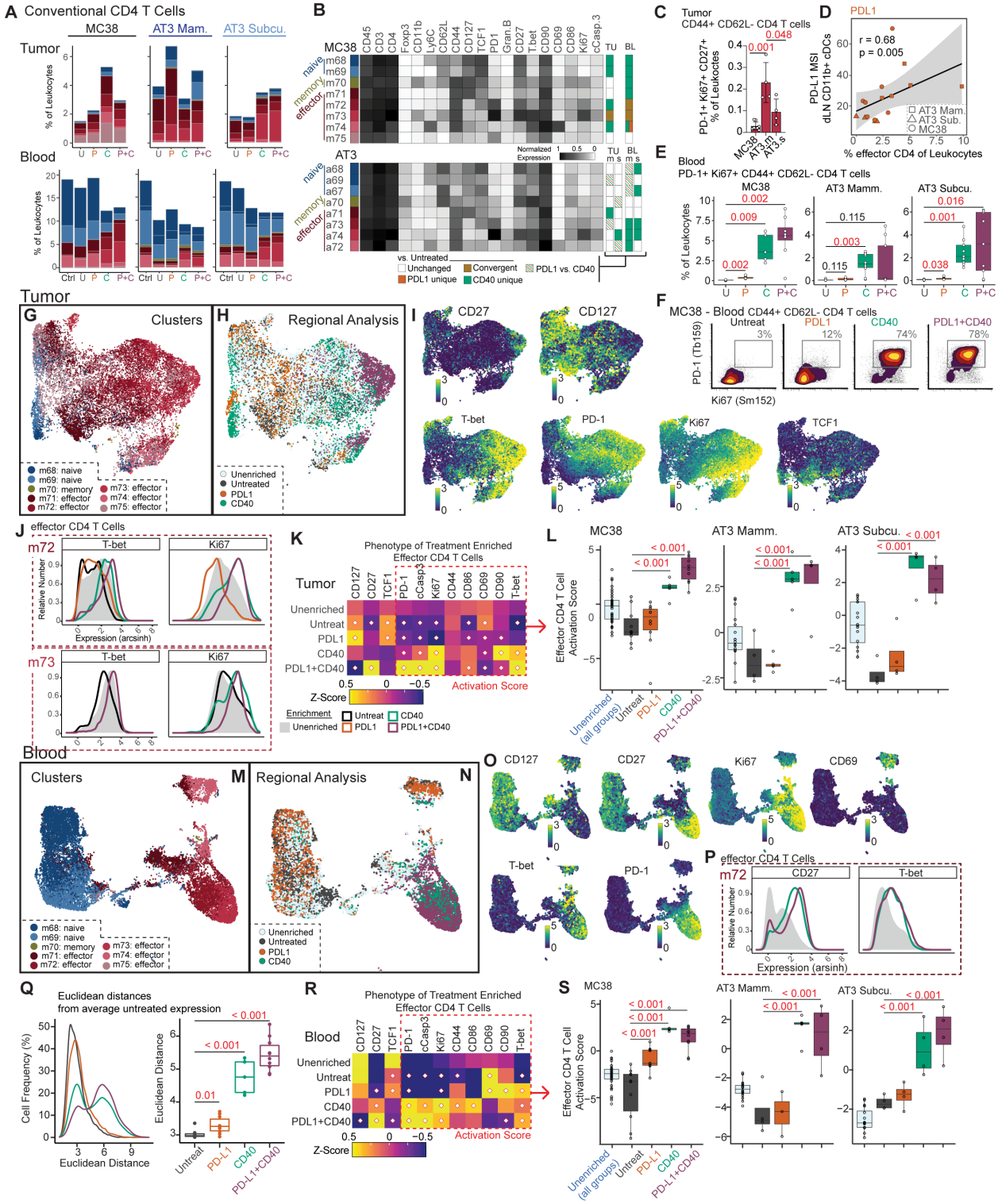

Figure 3.15: CD40 drives greater systemic activation of effector CD4$^+$ T cells than checkpoint blockade.

A, CD4$^+$ T cell cluster frequencies as a percent of total leukocytes for the tumor and blood with treatment across models. **B**, Cluster protein expression identities across naïve, memory, and

effector subsets. Significant clusters are indicated on the right, color by uniqueness or convergence between monotherapies as described in Figure 3.5. **C**, Frequency of effector $CD4^+$ T cells with a cluster m73/a74 phenotype; p values calculated by two-tailed t-test. **D**, Correlation between total tumor effector $CD4^+$ frequency and PD-L1 median signal intensity on $CD11b^+$ cDC2s in the dLN, after PD-L1 blockade across models; spearman. **E-F**, Frequency (**E**) and representative density plots (**F**) of Ki67 and PD-1 expression on effector $CD4^+$ T cells in the blood. **G**, UMAP of single $CD4^+$ T cells in MC38 tumor colored by cluster, subsetted to consistent numbers of total cells per treatment condition to represent internal composition. **H**, Regional Enrichment Analysis on MC38 tumor $CD4^+$ T cells. **I**, UMAPs of $CD4^+$ T cells in the MC38 tumor colored by protein expression intensity. **J-K**, Enriched region protein expression differences on intratumoral effector $CD4^+$ clusters m72 and m73 (**J**) and across all effector $CD4^+$ T cells (**K**); $p < 0.05$, SAM. **L**, Tumor effector $CD4^+$ T cell activation scores as the sum of activation marker Z-scores across treatment enriched regions, across models; p values calculated by Wilcoxon rank-sum test. **N-)**, Blood $CD4^+$ T cell UMAP and Regional Enrichment Analysis colored by cluster (**M**), enrichment category (**N**), or protein expression (**O**). **P**, Enriched region protein expression differences on blood effector $CD4^+$ clusters m72; $p < 0.05$, SAM. **Q**, Euclidean distance between blood $CD4^+$ T cell protein expression profiles across treatments. **R**, Enriched region protein expression differences on effector $CD4^+$ T cells in the blood, across models; $p < 0.05$, SAM. **S**, Blood effector $CD4^+$ T cell activation scores as the sum of activation marker Z-scores across treatment enriched regions; p values calculated by Wilcoxon rank-sum test.

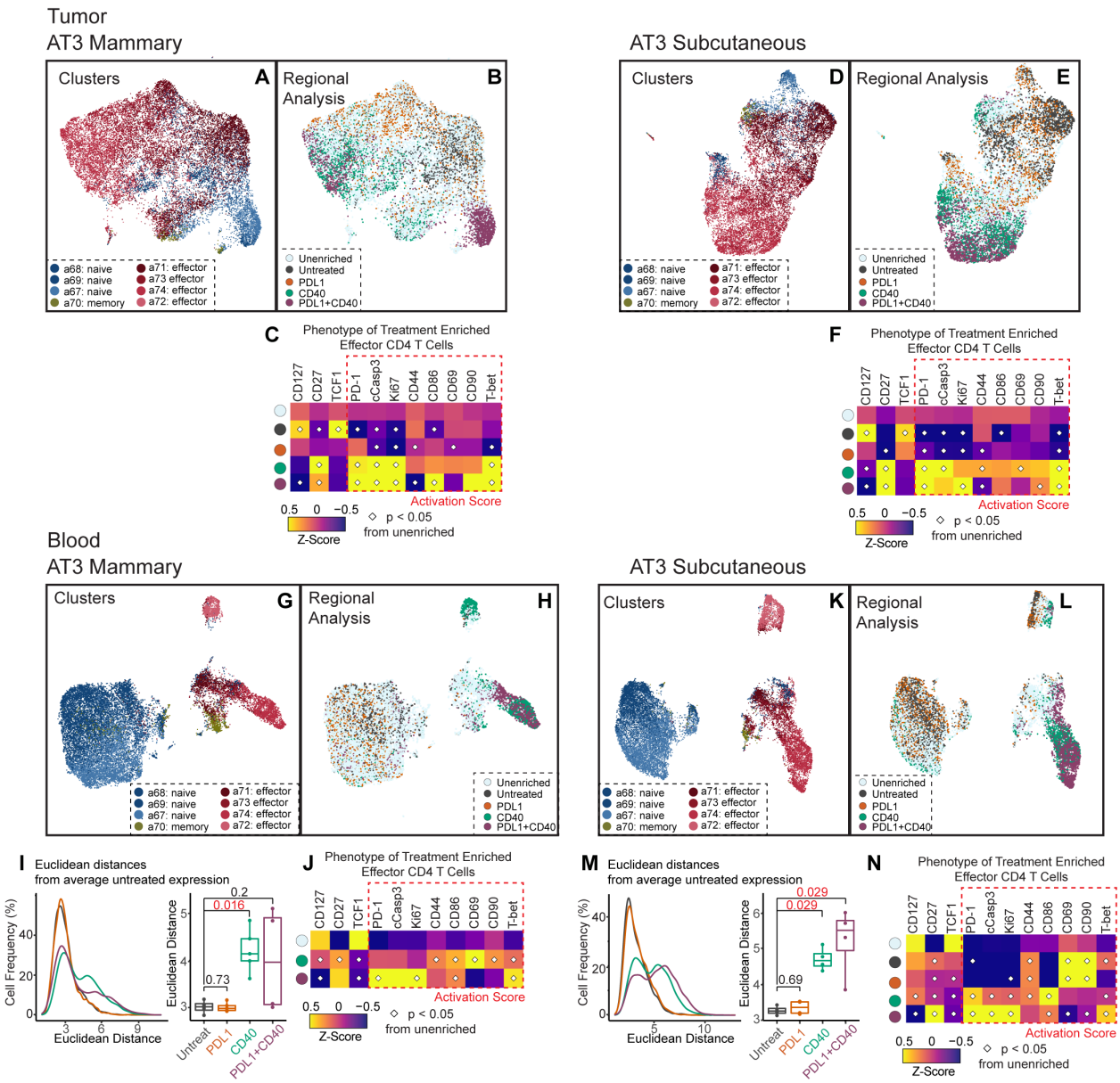

Figure 3.16: CD4⁺ T cells acquire different phenotypic states based on immunotherapy in AT3 cancer models.

A-F, UMAPs of tumor CD4⁺ T cells colored by cluster (**A** and **D**) or Regional Enrichment Analysis (**B** and **E**), and relative memory or activation marker expressions for each enrichment category on effector CD4⁺ T cells (**C** and **F**) for mammary or subcutaneous AT3. **G-J**, UMAPs of blood CD4⁺ T cells colored by cluster (**G** and **K**) or Regional Enrichment Analysis (**H** and **L**), Euclidean distance between blood CD4⁺ T cell expression profiles across treatments (**I** and **M**), and relative memory or activation marker expressions for each enrichment category on effector CD4⁺ T cells (**J** and **N**) for mammary or subcutaneous AT3; p <0.05, by Wilcoxon rank-sum test in **I** and **M** or by SAM in **C,F, J**, and **N**.

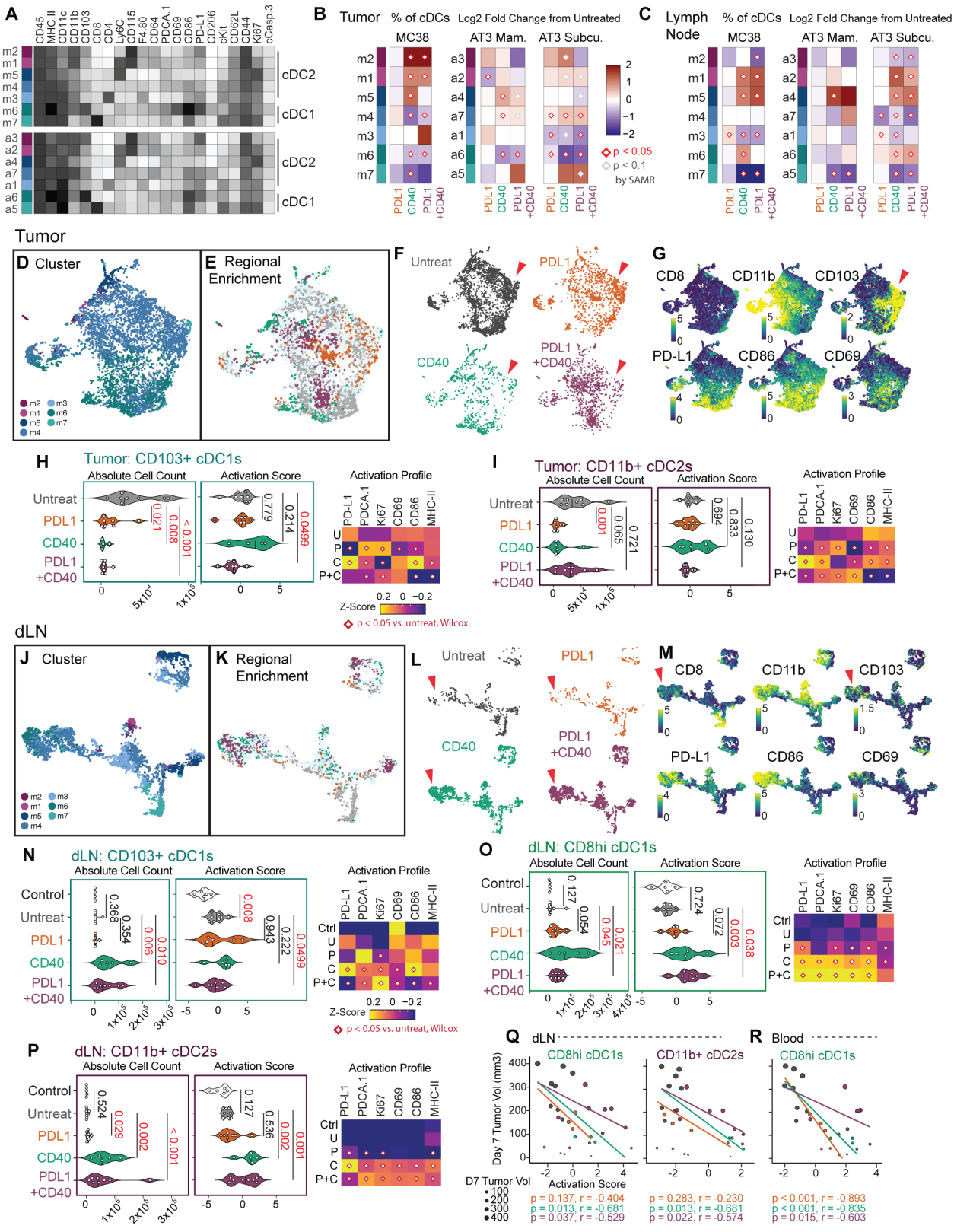

Figure 3.17: CD40 agonism drives activation and accumulation of conventional dendritic cells in the periphery.

A, Conventional dendritic cell cluster expression profiles for MC38 (top) and AT3 (bottom). **B-C**, Heatmaps of compositional cDC cluster frequencies across models in the tumor (**B**) and dLN (**C**); $p < 0.05$, SAM. **D-G**, UMAP and Regional Enrichment Analysis for cDCs in the tumor, colored by cluster (**D**), Regional Enrichment (**E**), treatment condition (**F**), and protein expression (**G**). $CD103^+$ subsets highlighted with a red arrow. **H-I**, Absolute cell counts, activation scores and heatmap of relative activation marker expression on $CD103^+$ cDC1s (**H**) and $CD11b^+$ cDC2s (**I**) in the tumor; p values calculated by Wilcoxon rank-sum test. **J-M**, UMAP and Regional Enrichment Analysis for cDCs in the dLN, colored by cluster (**J**), Regional Enrichment (**K**), treatment condition (**L**), and protein expression (**M**). $CD103^+$ subsets highlighted with a red arrow. **N-P**, Absolute cell counts, activation scores and heatmap of relative activation marker expression on $CD103^+$ cDC1s (**N**), $CD8^+$ cDC1s (**O**) and $CD11b^+$ cDC2s (**P**) in the dLN; p values calculated by Wilcoxon rank-sum test. **Q**-**R**, Correlation between treatment efficacy and activation scores on dLN $CD8^+$ cDC1s and $CD11b^+$ cDC2s (**Q**), and blood $CD8^+$ cDC1s (**R**) in MC38; $p < 0.05$, spearman.

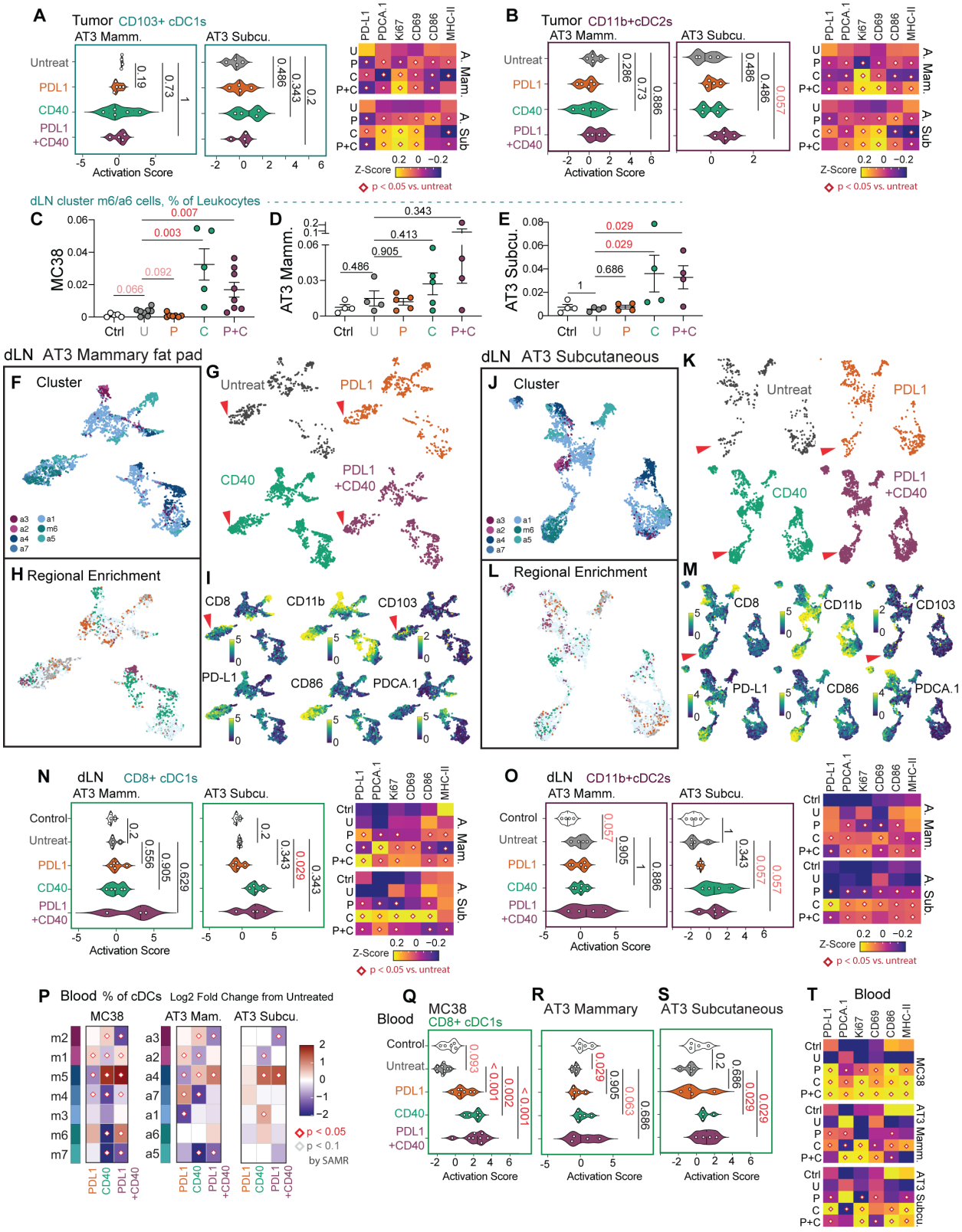

Figure 3.18: CD40 can stimulate previously inactive cDC1s and cDC2s in the periphery.
A-B, activation scores and heatmap of relative activation marker expression on CD103^{+} cDC1s

(**A**) and CD11b$^+$ cDC2s (**B**) in the tumor of AT3 models; p values calculated by Wilcoxon rank-sum test. **C-D**, Frequency of cells falling into the CD103$^+$ cluster m6 for MC38 (**C**) or cluster a6 for mammary AT3 (**D**) or subcutaneous AT3 (**E**); p values calculated by Wilcoxon rank-sum test. **F-M**, UMAP and Regional Enrichment Analysis for cDCs in the dLN of mammary and subcutaneous AT3 tumor-bearing animals, colored by cluster (**F** and **J**), treatment condition (**G** and **K**), Regional Enrichment (**H** and **L**) and protein expression (**I** and **M**), CD103$^+$ subsets highlighted with a red arrow. **N-O**, activation scores and heatmap of relative activation marker expression on CD8$^+$ cDC1s (**N**) and CD11b$^+$ cDC2s (**O**) in the dLN of AT3 models; p values calculated by Wilcoxon rank-sum test. **P**, Heatmaps of compositional cDC cluster frequencies across models in the blood; $p < 0.05$, SAM. **Q-S**, Activation scores on CD8$^+$ cDC1s in the blood in MC38 (**Q**), mammary AT3 (**R**) or subcutaneous AT3 (**S**) tumor-bearing animals; p values calculated by Wilcoxon rank-sum test. **T**, Heatmap of relative activation marker expression on CD8$^+$ cDC1s in the blood, corresponding with **Q-S**; $p < 0.05$, SAM.

Table 3.1: Antibody panel used for mass cytometry experiments.

MAIN

Channel	Metal	Protein	Concentration (ug/ml)	Clone	Vendor	Catalogue #	Lot #
89	Y	Ter119	3	TER119	Biolegend	116202	B250339
113	In	IgM	3	RMM-1	Biolegend	406502	B256697
115	In	CD45	6	30-F11	Biolegend	103102	B253429
139	La	Ly6G	1.5	1A8	Biolegend	127602	B265459
140	Ce	KLRG1	0.75	2F1	BD	562190	8113778
141	Pr	GranzymeB	3	QA16A02	BioLegend	372202	--
142	Nd	CD49b	0.1875	HMα2	Biolegend	103501	--
143	Nd	CD11c	0.75	N418	Biolegend	117302	B191075
144	Nd	CD206	1.5	C068C2	Biolegend	141702	--
145	Nd	CD27	0.75	LG.3A10	Biolegend	124202	B233065
146	Nd	CD138	0.185	281-2	Biolegend	142502	B233106
147	Sm	PD-L1	1.5	GEN	Genentech	N/A	N/A
148	Nd	CD103	3	2E7	Biolegend	121402	B249116
149	Sm	SiglecF	1.5	E50-2440	BD	552125	7264727
150	Nd	PDCA-1	1.5	129c1	Biolegend	127102	B188381
151	Eu	Ly6C	0.75	HK1.4	Biolegend	128002	B253176
152	Sm	Ki67	6	SolA15	BD	556003	6280947
153	Eu	CD11b	0.75	M1/70	Biolegend	101202	B261558
154	Sm	cKit	1.5	2B8	Biolegend	105802	B241900
155	Gd	CD8	3	53-6.7	Biolegend	100702	B237234
156	Gd	CD4	0.75	RM4-5	Biolegend	100506	B251707
157	Gd	CD3	0.75	17A2	Biolegend	100202	B241388
158	Gd	B220	1.5	RA3-6B2	Biolegend	103202	B170375
159	Tb	PD-1	0.75	29F.1A12	Biolegend	135202	B196019
160	Gd	NK1.1	1.5	PK136	Biolegend	108702	B187819
161	Dy	T-bet	6	O4-46	BD	561263	3032551
162	Dy	TCRgd	1.5	GL3	Biolegend	118101	--
163	Dy	CD62L	3	95218	R&D	MAB5761	--
164	Dy	TCF1	1.5	C63D9	CellSignal	2203BF	--
165	Ho	CD69	0.75	Polyclonal	R&D	AF2386	UIU011808A
166	Er	FcER1a	1.5	MAR-1	Biolegend	134321	B243579
167	Er	Foxp3	3	NRRF-30	eBioscience	14-4771-80	1972297
168	Er	CD86	0.1875	GL-1	Biolegend	105002	B244244
169	Tm	F4/80	1.5	BM8	Biolegend	123102	B226029
170	Er	CD115	1.5	AFS98	Biolegend	135521	--
171	Yb	CD64	6	X54-5/7.1	Biolegend	139302	B270355
172	Yb	cCaspase3	1	5A1E	Fluidigm	3172023A	0391807
173	Yb	CD19	0.75	6D5	Biolegend	115502	B166684
174	Yb	CD127	4	A7R34	BioLegend	135002	B168578
175	Lu	CD44	0.375	IM7	Biolegend	103002	B246298
176	Yb	CD90	0.75	G7	Biolegend	105202	B187334
209	Bi	MHC II	0.1875	M5/114.15.2	Biolegend	107602	B141287

Other Substitutes

Channel	Metal	Protein	Concentration (ug/ml)	Clone	Vendor	Catalogue #	Lot #
113	In	Ter119	3	TER119	Biolegend	116202	B250339
166	Er	CD127	4	A7R34	BioLegend	135002	B168578

3.5 Materials and Methods

Animals:

All mice were housed in an American Association for the Accreditation of Laboratory Animal Care–accredited animal facility and maintained in specific pathogen-free conditions. Animal experiments were approved and conducted in accordance with Institutional Animal Care & Use Program protocol number AN157618. Wild-type female C57BL/6 mice between 8-10 weeks old were purchased from The Charles River Laboratory and housed at our facility. MC38 ($1X10^5$ cells / 100 µl) colon cancer cells or AT3 ($5x10^5$ cells / 100 µl) breast cancer cells were transplanted into the subcutaneous region of the flank. AT3 ($5x10^5$ cells / 100 µl) breast cancer cells were also independently transplanted into the fourth mammary fat pad. Tumors were considered established for treatment when they reached ~150 mm^3 in volume. Animals were housed under standard SPF conditions with typical light/dark cycles and standard chow.

Cell Lines:

MC38 cells were gifted from Dr. Jane Grogan (Genentech). AT3 cells were gifted from Dr. Ross Levine (MSKCC). MC38 cells were cultured in RPMI-1640, and AT3 cells were cultured in DMEM, all supplemented with 10% fetal calf serum, 2 mM L-glutamine,100 U/ml penicillin and 100 mg/ml penicillin/streptomycin.

Treatments:

For immunotherapy studies, *in vivo* antibody treatments were given i.p. for a 7 day period starting when tumors reached ~150 mm^3 in volume: 200 ug of anti-PD-L1 (9708-6E11, Genentech) on day 0, 3 and 6, and 200 ug of agonistic anti-CD40 (FGK4.5, BioXCell) on day 0. Antibodies

were delivered in 100 µl volume in sterile PBS, containing either monotherapy or their combination. Tumor volumes were measured and calculated regularly using the modified ellipsoid formula ½ x (length x width^2).

Cytokine Quantification:

For *in vivo* circulating plasma cytokines, mice were bled via the retroorbital vein using heparinized capillary tubes. Blood was then centrifuged at 1000 x g for 10 minutes and the supernatant plasma was removed for analysis. Plasma samples were sent to Eve Technologies (Calgary, AB), and analyzed using a multiplex cytokine array.

Mass Cytometry Antibodies:

All mass cytometry antibodies and concentrations used for analysis can be found in Table 3.1. Primary conjugates of mass cytometry antibodies were prepared using the MaxPAR antibody conjugation kit (Fluidigm) according to the manufacturer's recommended protocol. Following labeling, antibodies were diluted in Candor PBS Antibody Stabilization solution (Candor Bioscience GmbH, Wangen, Germany) supplemented with 0.02% NaN3 in PBS to between 0.1 and 0.3 mg/ml and stored long-term at 4° C. Each antibody clone and lot was titrated to optimal staining concentrations using primary mouse samples.

Cell Preparation:

All tissue preparations were performed simultaneously from each individual mouse, as previously reported[46]. After euthanasia by $C0_2$ inhalation, peripheral blood was collected via the posterior vena cava prior to perfusion of the animal and transferred into sodium heparin-coated

vacuum tubes prior to dilution in PBS with 5 mM EDTA and 0.5% BSA (PBS/EDTA/BSA). Spleens and lymph nodes were homogenized in PBS/EDTA at 4° C. Bone marrow was flushed from femur and re-suspended in PBS/EDTA at 4° C. Tumors were finely minced and digested in RPMI-1640 with 4 mg/ml collagenase IV, and 0.1 mg/ml DNase I. After digestion, re-suspended cells were quenched with PBS/EDTA at 4° C. All tissues were washed with PBS/EDTA and re-suspended 1:1 with PBS/EDTA and 100 mM cisplatin (Enzo Life Sciences, Farmingdale, NY) for 60 s before quenching 1:1 with PBS/EDTA/BSA to determine viability as previously described[83]. Cells were centrifuged at 500 x g for 5 min at 4° C and re-suspended in PBS/EDTA/BSA at a density between 1-10 x 106 cells/ml. Suspensions were fixed for 10 min at room temperature (RT) using 1.6% paraformaldehyde in PBS and frozen at -80° C.

Mass-Tag Cellular Barcoding:

Mass-tag cellular barcoding was performed as previously described[114]. Briefly, 1 x 10^6 cells from each animal were barcoded with distinct combinations of stable Pd isotopes in 0.02% saponin in PBS. Samples from any given tissue from each mouse per experiment group were barcoded together. Cells were washed once with cell staining media (PBS with 0.5% BSA and 0.02% NaN3), and once with 1X PBS, and pooled into a single FACS tube (BD Biosciences). After data collection, each condition was deconvoluted using a single-cell debarcoding algorithm[114].

Mass Cytometry Staining and Measurement:

Cells were resuspended in cell staining media (PBS with 0.5% BSA and 0.02% NaN3) and metal-labeled antibodies against CD16 and CD32 were added at 20 mg/ml for 5 min at RT on a

shaker to block Fc receptors. Surface marker antibodies were then added, yielding 500 µl final reaction volumes and stained for 30 min at RT on a shaker. Following staining, cells were washed 2 times with cell staining media, then permeabilized with methanol for at 10 min at 4° C. Cells were then washed twice in cell staining media to remove remaining methanol and stained with intracellular antibodies in 500 ml for 30 min at RT on a shaker. Cells were washed twice in cell staining media and then stained with 1ml of 1:4000 191/193Ir DNA intercalator (Fluidigm) diluted in PBS with 1.6% paraformaldehyde overnight. Cells were then washed once with cell staining media and then two times with double-deionized (dd) H_20. Care was taken to assure buffers preceding analysis were not contaminated with metals in the mass range above 100 Da. Mass cytometry samples were diluted in dd H_20 containing bead standards (see below) to approximately 10^6 cells per ml and then analyzed on a CyTOF 2 mass cytometer (Fluidigm) equilibrated with dd H_20. We analyzed 1-5 x 10^5 cells per animal, per tissue, per time point, consistent with generally accepted practices in the field.

Mass Cytometry Bead Standard Data Normalization:

Data normalization was performed as previously described[46]. Briefly, just before analysis, the stained and intercalated cell pellet was resuspended in freshly prepared dd H_20 containing the bead standard at a concentration ranging between 1 and 2 x 10^4 beads/ml. The mixture of beads and cells were filtered through a filter cap FACS tubes (BD Biosciences) before analysis. All mass cytometry files were normalized together using the mass cytometry data normalization algorithm[115], which uses the intensity values of a sliding window of these bead standards to correct for instrument fluctuations over time and between samples.

Mass Cytometry Gating Strategy:

After normalization and debarcoding of files, singlets were gated by Event Length and DNA. Live cells were identified by Cisplatin negative cells. All positive and negative populations and antibody staining concentrations were determined by titration on positive and negative control cell populations.

Systemic Immune Clustering:

As previously described[46,83], $CD45^+$ Ter119- live immune cells from each tissue for all animals were clustered together and then deconvolved into their respective samples. Clustering was set to a pre-defined number of 100 clusters for MC38 (clusters m), and separately 100 clusters for AT3 tumor models (clusters a). Separate clustering was performed because the experiments were conducted at different times for MC38 and AT3. To clean potentially redundant clusters, and pair datasets between models, we performed nearest neighbor calculations and combined any clusters that were more similar within a dataset than between datasets, indicating redundant or non-visually discriminate clusters. Once cleaned, clusters in the AT3 datasets were matched to their most similar MC38 dataset cluster, again by nearest neighbor analysis. There were clusters, or immune cell states, with no close association between datasets. The result was a total of 79 clusters for both MC38 and AT3 datasets.

A force-directed cluster map was generated based on MC38 clusters using the scaffold map R package available at github.com/SpitzerLab/statisticalScaffold. Scaffold analysis combines unsupervised clustering to identify immune cell subsets with dimensionality reduction using a force-directed graph to visualize the organization of immune cells within a tissue. Regions of the graph are easy to identify due to the incorporation of canonical immune cell types defined

manually as ‘landmarks’ in the graph. Each cluster was colored corresponding to its most similar immune landmark.

Convergent and Divergent Analysis:

For convergent analysis, clusters were compared between untreated and each monotherapy as well as between monotherapies to identify significant differences using the Significance Analysis of Microarrays algorithm[116] (using a q-value cutoff of 0.05). Significantly changed clusters were then binned into monotherapy unique, significant from untreated in one monotherapy but not the other, convergent similar, with significant changes in the same direction with both monotherapies but to significantly different magnitudes, and lastly convergent same, with significant change from control to the same magnitude. Analysis was performed separately for each organ, in each model.

For emergent analysis, significantly changed clusters were identified in combination therapy animals compared to untreated animals. Referencing the previously calculated changes with each monotherapy, clusters were then binned as emergent, antagonistic, or mimetic. Emergence was classified as novel, only significant with combination therapy, cooperative, significantly greater than changes induced by both monotherapies, or augmentative, significantly greater than a change induce by one monotherapy. Antagonism was classified as a compromise, an intermediate change between monotherapies, nullify, significant changes by both monotherapies no longer reach significance, or antagonize PD-L1 blockade or CD40 agonism therapies, changes induced by a specific monotherapy no longer reach significance. Lastly, mimicry was classified as specific to one monotherapy, resulting in the same significant change as PD-L1 or CD40, or convergent, significantly changed to the same magnitude as monotherapies.

Systemic Correlation Networks:

Systemic correlation networks were generated by first identifying which clusters were significantly different from control, or untreated tumor-bearing animals using the Significance Analysis of Microarrays algorithm[116] (using a q-value cutoff of 0.05). The log2 fold change was then calculated for each significantly altered cluster, and these values for each cluster were correlated across tissues by nonparametric Spearman's rank correlation. Values correlated included untreated and the treatment group of interest, resulting in associations in the change from baseline and not necessarily overall abundance (likewise for comparisons in untreated animals from control). Significant correlations with $p < 0.05$ were plotted in circular networks using igraph in R, with red lines denoting changes in the same direction and blue lines denoting changes in opposing directions.

Regional Enrichment Analysis:

For T cell Regional Enrichment Analysis, immune cells were subsetted to a consistent number of cells in each treatment condition (5,000 per condition for most cases, 1,800 for AT3 tumor analyses with lower T cell infiltration). UMAP dimensionality reduction was performed in R to visualize cells by cluster, condition, and protein expression. Independent from UMPA, nearest neighbor analysis was performed to identify the 15 nearest single cells in each dataset. Each single cell was then classified by the treatment identity of its neighbors, either significantly enriched for one treatment condition or unenriched. The enrichment cutoff, or number of neighbors of a specific condition to be called enriched, was defined as $p < 0.05$ chance of random sampling from a set of 15 giving a cutoff of 7. We increased the cutoff to 8 of 15 neighbors to maximize differences by treatment and minimized enrichment by independent animal. UMAPs were then colored by this

treatment enrichment classification.

Dendritic cell Regional Enrichment Analysis was performed similarly, except we did not subset to the same number of cells per condition due to the paucity of DCs in specific treatment conditions. We only subsetted to correct for the N per treatment group. The enrichment cutoff here was independently calculated per treatment condition, depending on the frequency of that condition in the dataset.

Differences in protein expression intensities between enrichment groups were calculated using Significance Analysis of Microarrays, comparing each enrichment category to unenriched protein expression intensities. Results for specific clusters were plotted as histograms, with the unenriched protein expression in gray and significant deviations in enrichment regions overlayed and colored accordingly. Results across all effector clusters were plotted as expression Z-scores.

Quantification and statistical analysis:

Comparison of cluster frequencies and protein expression intensities in enriched zones were performed using Significance Analysis of Microarrays as described above and in Bair and Tibshirani, 2004 and Bruggner et al., 2014. Features with $p < 0.05$ were considered statistically significant. Correlation analyses were performed using Spearman correlation, with Benjamini-Hochberg correction in cases of multiple comparisons. All comparisons were made using two-sided t tests in Prism or by two-sided Wilcoxon rank-sum test in R, with Benjamini-Hochberg correction in cases of multiple comparisons, as noted in the figure legends. All tests with $p < 0.05$ were considered statistically significant. N = 3 to 8 independent mice for each experimental condition.

Data availability:

All mass cytometry data are publicly available by request to the senior author without restrictions.

Code availability:

The Regional Enrichment Analysis package is available by request to the senior author without restrictions.

Chapter 4 Closing and Future Directions

Collectively, this series of studies holistically interrogates the systemic nature of tumor-induced immune disruption across diverse cancer contexts, which bears out consequences on *de novo* functional capacity and reversibility that have implications for top immunotherapeutic strategies. My doctoral research shows that:

1) Cancer cell type and anatomical location each contribute to shaping the immune macroenvironment in cancer; interestingly, metastases induce a much quieter systemic immune impact than the primary tumor.
2) Secondary viral or bacterial challenges exposed weakened adaptive immune responses in tumor-burdened animals, which can be overcome by strong stimulation of antigen-presenting cells, namely conventional dendritic cells.
3) Successful resection of primary tumor burden normalizes the systemic immune landscape, providing opportunity for outgrowth in cases with previously undetected disseminated disease.
4) Systemic immune remodeling is indicative of peripheral immune engagement capable of mounting productive antitumor responses with PD-L1 blockade, whereas agonism of CD40 is sufficient to induce antitumor immunity even in previously immunologically quiet systemic contexts.

Altogether, this body of work reveals that the immune macroenvironment in cancer is a powerful tool to determine which immune intervention strategy best serves each context, and to understand why therapies fail so that we may design more inclusive next generation immunotherapeutics.

Several open questions remain following these studies, including what specific aspects of the peripheral immune response are most informative in designing treatment strategies. The studies largely investigated mouse models of cancer, with individual findings associated with observations in human patients. It is imperative that the field of cancer immunology amass a collection of patient peripheral immune profiling to tease apart which active immune programs are taking place and how immune interventions modulate these responses across diverse patient contexts. Machine learning is a powerful tool that can be exploited to root out a collection of peripheral immune signatures that predict optimal immune perturbation or identify gaps in our arsenal of immune modulations. There is also opportunity to use regular patient peripheral immune profiling to identify when therapeutic resistance begins to develop, and how to change strategy to maintain efficacy. These characterizations can be used to answer important mechanistic questions that include how disease stage and metastasis, cancer cell type, and anatomical location each contribute to overall remodeling of systemic immunity.

We and several others have demonstrated the importance of cDC function in driving successful *de novo* antitumor immune responses[52,53,132]. Even checkpoint blockade, originally believed to de-restrict effector T cells in the TME, has been shown to rely on cDC interactions with PD-1 expressing T cells in the dLN. An important next step is to understand when cDC function needs to be supported by removing checkpoints versus initiated by strong stimuli such as CD40 agonism. There is already some indication in the literature that too strong of an immune stimulation, when unwarranted, can actually abrogate antitumor immunity. As CD40 agonism is highly non-specific, more targeted alternatives for manipulating cDC behaviors should be sought. Furthermore, it will be important to define what preexisting peripheral immune responses need to exist for PD-L1 blockade to be efficacious. Although our data and recent literature support cDC

activation in the tumor dLN as the critical driver, there are a variety of other peripheral immune changes that may support a beneficial outcome. Along these lines, it is not clear how strong of a T cell response is actually required for productive tumor clearance; is it much weaker after PD-L1 blockade than CD40 agonism, yet both can be efficacious. There are additional implications for *de novo* immune responses to other immune challenges that may arise concurrent with tumor burden, such as weaker viral or bacterial adaptive responses demonstrated in my studies, that warrant future work on how to support unrelated immune activities in cancer patients.

An area not fully addressed here, but important for future follow-up is the long-term consequences of extensive systemic immune remodeling, whether by natural tumor burden or by immunotherapeutic interventions. We show that tumor resection at mid-stage disease is sufficient to reverse the majority of peripheral changes, but this plasticity may be lost at some point during tumor progression. Even with mid-stage disease, there were small but persistent changes in peripheral myeloid subsets after two weeks. It remains an open question whether patients who have survived cancer have lasting bias or disruption in immune responses. Extending this to more direct perturbations, chemotherapy has been shown to drive lasting changes in $CD4^+$ T cells in breast cancer patients that likely skews normal immune responses[31]. Lasting consequences of immunotherapies are also a real possibility, especially with the extent of systemic immune disruption driven by CD40 agonism. There are obvious autoimmune comorbidities with strong immune stimulation, but more subtle changes in the overall composition of the immune system or future response biases remain to be thoroughly characterized.

There is much more work to be done to fully engage the immune system against cancer, but we are making great strides in understanding the breadth of cancer evasion tactics and how we can systematically circumvent each one.

References

1. Burnet, F. M. The Concept of Immunological Surveillance. in *Progress in experimental tumor research. Fortschritte der experimentellen Tumorforschung. Progres de la recherche experimentale des tumeurs* vol. 13 1–27 (Karger Publishers, 1970).
2. Shankaran, V. *et al.* IFNγ and lymphocytes prevent primary tumour development and shape tumour immunogenicity. *Nature* **410**, 1107–1111 (2001).
3. Ruffell, B., Affara, N. I. & Coussens, L. M. Differential macrophage programming in the tumor microenvironment. *Trends Immunol.* **33**, 119–126 (2012).
4. Kumar, V., Patel, S., Tcyganov, E. & Gabrilovich, D. I. The Nature of Myeloid-Derived Suppressor Cells in the Tumor Microenvironment. *Trends in Immunology* vol. 37 208–220 (2016).
5. Nagarsheth, N., Wicha, M. S. & Zou, W. Chemokines in the cancer microenvironment and their relevance in cancer immunotherapy. *Nature Reviews Immunology* (2017) doi:10.1038/nri.2017.49.
6. Kitamura, T. *et al.* Monocytes differentiate to immune suppressive precursors of metastasis-associated macrophages in mouse models of metastatic breast cancer. *Front. Immunol.* **8**, (2018).
7. Cassetta, L. & Pollard, J. W. Targeting macrophages: Therapeutic approaches in cancer. *Nat. Rev. Drug Discov.* **17**, 887–904 (2018).
8. Wagner, J. *et al.* A Single-Cell Atlas of the Tumor and Immune Ecosystem of Human Breast Cancer. *Cell* **177**, 1–16 (2019).
9. Azizi, E. *et al.* Single-Cell Map of Diverse Immune Phenotypes in the Breast Tumor Microenvironment. *Cell* **174**, 1293–1308 (2018).

10. Lavin, Y. *et al.* Innate Immune Landscape in Early Lung Adenocarcinoma by Paired Single-Cell Analyses. *Cell* **169**, (2017).

11. Vesely, M. D. & Schreiber, R. D. Cancer Immunoediting: antigens, mechanisms and implications to cancer immunotherapy. doi:10.1111/nyas.12105.

12. O'Donnell, J. S., Teng, M. W. L. & Smyth, M. J. Cancer immunoediting and resistance to T cell-based immunotherapy. *Nat. Rev. Clin. Oncol.* **16**, 151–167 (2019).

13. Yarmarkovich, M. *et al.* Immunogenicity and Immune Silence in Human Cancer. *Front. Immunol.* **11**, 69 (2020).

14. Casbon, A.-J. *et al.* Invasive breast cancer reprograms early myeloid differentiation in the bone marrow to generate immunosuppressive neutrophils. *Proc. Natl. Acad. Sci. U. S. A.* **112**, E566-75 (2015).

15. Diaz-Montero, C. M. *et al.* Increased circulating myeloid-derived suppressor cells correlate with clinical cancer stage, metastatic tumor burden, and doxorubicin-cyclophosphamide chemotherapy. *Cancer Immunol. Immunother.* **58**, 49–59 (2009).

16. Talmadge, J. E. & Gabrilovich, D. I. History of myeloid-derived suppressor cells. *Nat. Rev. Cancer* **13**, 739–752 (2013).

17. Veglia, F., Perego, M. & Gabrilovich, D. Myeloid-derived suppressor cells coming of age review-article. *Nature Immunology* vol. 19 (2018).

18. Ma, P. *et al.* Circulating Myeloid Derived Suppressor Cells (MDSC) That Accumulate in Premalignancy Share Phenotypic and Functional Characteristics With MDSC in Cancer. *Front. Immunol.* **10**, 1401 (2019).

19. Toor, S. M. *et al.* Myeloid Cells in Circulation and Tumor Microenvironment of Colorectal Cancer Patients with Early and Advanced Disease Stages. *J. Immunol. Res.*

2020, (2020).

20. Meyer, M. A. *et al.* Breast and pancreatic cancer interrupt IRF8-dependent dendritic cell development to overcome immune surveillance. *Nat. Commun.* **9**, 1–19 (2018).
21. Mastelic-Gavillet, B. *et al.* Quantitative and qualitative impairments in dendritic cell subsets of patients with ovarian or prostate cancer. *Eur. J. Cancer* **135**, 173–182 (2020).
22. Santegoets, S. J. *et al.* Myeloid derived suppressor and dendritic cell subsets are related to clinical outcome in prostate cancer patients treated with prostate GVAX and ipilimumab. *J. Immunother. Cancer* **2**, 31 (2014).
23. Almand, B. *et al.* Clinical Significance of Defective Dendritic Cell Differentiation in Cancer. *Clin. Cancer Res.* **6**, (2000).
24. Van Cruijsen, H. *et al.* Sunitinib-induced myeloid lineage redistribution in renal cell cancer patients: CD1c+ dendritic cell frequency predicts progression-free survival. *Clin. Cancer Res.* **14**, 5884–5892 (2008).
25. Failli, A., Legitimo, A., Orsini, G., Romanini, A. & Consolini, R. Numerical defect of circulating dendritic cell subsets and defective dendritic cell generation from monocytes of patients with advanced melanoma. *Cancer Lett.* **337**, 184–192 (2013).
26. Lin, J. H. *et al.* Type 1 conventional dendritic cells are systemically dysregulated early in pancreatic carcinogenesis. *J. Exp. Med.* **217**, (2020).
27. Tabarkiewicz, J., Rybojad, P., Jablonka, A. & Rolinski, J. CD1c+ and CD303+ dendritic cells in peripheral blood, lymph nodes and tumor tissue of patients with non-small cell lung cancer - PubMed. *Oncol. Rep.* **19**, 237–243 (2008).
28. Ménétrier-Caux, C., Ray-Coquard, I., Blay, J. Y. & Caux, C. Lymphopenia in Cancer Patients and its Effects on Response to Immunotherapy: An opportunity for combination

with Cytokines? *Journal for ImmunoTherapy of Cancer* vol. 7 1–15 (2019).

29. Cader, F. Z. *et al.* A peripheral immune signature of responsiveness to PD-1 blockade in patients with classical Hodgkin lymphoma. *Nat. Med.* **26**, 1468–1479 (2020).
30. Shaked, Y. The pro-tumorigenic host response to cancer therapies. *Nature Reviews Cancer* vol. 19 667–685 (2019).
31. Gustafson, C. E. *et al.* Immune cell repertoires in breast cancer patients after adjuvant chemotherapy. (2020) doi:10.1172/jci.insight.134569.
32. Talebian Yazdi, M. *et al.* Standard radiotherapy but not chemotherapy impairs systemic immunity in non-small cell lung cancer. *Oncoimmunology* **5**, e1255393 (2016).
33. van Meir, H. *et al.* Impact of (chemo)radiotherapy on immune cell composition and function in cervical cancer patients. *Oncoimmunology* **6**, e1267095 (2017).
34. Wesolowski, R. *et al.* Circulating myeloid-derived suppressor cells increase in patients undergoing neo-adjuvant chemotherapy for breast cancer. *Cancer Immunol. Immunother.* **66**, 1437–1447 (2017).
35. Larsson, A. M., Roxå, A., Leandersson, K. & Bergenfelz, C. Impact of systemic therapy on circulating leukocyte populations in patients with metastatic breast cancer. *Sci. Rep.* **9**, (2019).
36. Valdés-Ferrada, J. *et al.* Peripheral Blood Classical Monocytes and Plasma Interleukin 10 Are Associated to Neoadjuvant Chemotherapy Response in Breast Cancer Patients. *Front. Immunol.* | *www.frontiersin.org* **11**, (2020).
37. Axelrod, M. L. *et al.* Changes in peripheral and local tumor immunity after neoadjuvant chemotherapy reshape clinical outcomes in patients with breast cancer. *Clin. Cancer Res.* clincanres.3685.2019 (2020) doi:10.1158/1078-0432.ccr-19-3685.

38. Yu, W. Di, Sun, G., Li, J., Xu, J. & Wang, X. Mechanisms and therapeutic potentials of cancer immunotherapy in combination with radiotherapy and/or chemotherapy. *Cancer Letters* vol. 452 66–70 (2019).

39. Luo, Q., Zhang, L., Luo, C. & Jiang, M. Emerging strategies in cancer therapy combining chemotherapy with immunotherapy. *Cancer Letters* vol. 454 191–203 (2019).

40. Bailly, C., Thuru, X. & Quesnel, B. Combined cytotoxic chemotherapy and immunotherapy of cancer: modern times. *NAR Cancer* **2**, (2020).

41. Tohme, S., Simmons, R. L. & Tsung, A. Surgery for cancer: A trigger for metastases. *Cancer Research* vol. 77 1548–1552 (2017).

42. Krall, J. A. *et al.* The systemic response to surgery triggers the outgrowth of distant immune-controlled tumors in mouse models of dormancy. *Sci. Transl. Med.* **10**, eaan3464 (2018).

43. Bosiljcic, M. *et al.* Targeting myeloid-derived suppressor cells in combination with primary mammary tumor resection reduces metastatic growth in the lungs. *Breast Cancer Res.* **21**, (2019).

44. Kallis, M. P. *et al.* Pharmacological prevention of surgery-accelerated metastasis in an animal model of osteosarcoma. *J. Transl. Med.* **18**, (2020).

45. Mathios, D. *et al.* Anti – PD-1 antitumor immunity is enhanced by local and abrogated by systemic chemotherapy in GBM. *Sci. Transl. Med.* **8**, 1–12 (2016).

46. Spitzer, M. H. *et al.* Systemic Immunity Is Required for Effective Cancer Immunotherapy. *Cell* **168**, 487-502.e15 (2017).

47. Fransen, M. F. & Van Hall, T. Tumor-draining lymph nodes are pivotal in PD-1/PD-L1 checkpoint therapy. *JCI Insight* **3**, e124507 (2018).

48. Spitzer, M. H. *et al.* Systemic Immunity Is Required for Effective Cancer Immunotherapy. *Cell* **168**, 487–502 (2017).

49. Lau, J. *et al.* Tumour and host cell PD-L1 is required to mediate suppression of anti-tumour immunity in mice. *Nat. Commun.* **8**, (2017).

50. Lin, H. *et al.* Host expression of PD-L1 determines efficacy of PD-L1 pathway blockade–mediated tumor regression. *J. Clin. Invest.* **128**, 805–815 (2018).

51. Strauss, L. *et al.* Targeted deletion of PD-1 in myeloid cells induces antitumor immunity. *Sci. Immunol.* **5**, eaay1863 (2020).

52. Oh, S. A. *et al.* PD-L1 expression by dendritic cells is a key regulator of T-cell immunity in cancer. *Nat. Cancer* (2020) doi:10.1038/s43018-020-0075-x.

53. Dammeijer, F. *et al.* The PD-1 / PD-L1-Checkpoint Restrains T cell Immunity in Tumor-Draining Lymph Nodes. *Cancer Cell* **38**, 1–16 (2020).

54. Chamoto, K. *et al.* Mitochondrial activation chemicals synergize with surface receptor PD-1 blockade for T cell-dependent antitumor activity. *PNAS* **114**, E761–E770 (2017).

55. Philip, M. *et al.* Chromatin states define tumour-specific T cell dysfunction and reprogramming. *Nature* **545**, 452–456 (2017).

56. Scott, A. C. *et al.* TOX is a critical regulator of tumour-specific T cell differentiation. *Nature* **571**, 270–274 (2019).

57. Khan, O. *et al.* TOX transcriptionally and epigenetically programs CD8+ T cell exhaustion. *Nature* **571**, 211–218 (2019).

58. Yu, Y.-R. *et al.* Disturbed mitochondrial dynamics in CD8+ TILs reinforce T cell exhaustion. *Nat. Immunol.* 1–12 (2020) doi:10.1038/s41590-020-0793-3.

59. Sade-Feldman, M. *et al.* Defining T Cell States Associated with Response to Checkpoint

Immunotherapy in Melanoma. *Cell* **175**, 998-1013.e20 (2018).

60. Yost, K. E. *et al.* Clonal replacement of tumor-specific T cells following PD-1 blockade. *Nat. Med.* **25**, 1251–1259 (2019).

61. Wu, T. D. *et al.* Peripheral T cell expansion predicts tumour infiltration and clinical response. *Nature* (2020) doi:10.1038/s41586-020-2056-8.

62. Valpione, S. *et al.* Immune awakening revealed by peripheral T cell dynamics after one cycle of immunotherapy. *Nat. Cancer* **1**, 210–221 (2020).

63. Kamphorst, A. O. *et al.* Rescue of exhausted CD8 T cells by PD-1-targeted therapies is CD28-dependent. *Science (80-.).* **355**, 1423–1427 (2017).

64. Vonderheide, R. H. CD40 Agonist Antibodies in Cancer Immunotherapy. *Annual Review of Medicine* vol. 71 47–58 (2020).

65. Li, D.-K. & Wang, W. Characteristics and clinical trial results of agonistic anti-CD40 antibodies in the treatment of malignancies (Review). *Oncol. Lett.* **20**, 1–1 (2020).

66. Morrison, A. H., Diamond, M. S., Hay, C. A., Byrne, K. T. & Vonderheide, R. H. Sufficiency of CD40 activation and immune checkpoint blockade for T cell priming and tumor immunity. *PNAS* **117**, 8022–8031 (2020).

67. O'Hara, M. H. *et al.* Abstract CT004: A Phase Ib study of CD40 agonistic monoclonal antibody APX005M together with gemcitabine (Gem) and nab-paclitaxel (NP) with or without nivolumab (Nivo) in untreated metastatic ductal pancreatic adenocarcinoma (PDAC) patients. in *Cancer Research* vol. 79 CT004–CT004 (American Association for Cancer Research (AACR), 2019).

68. Fransen, M. F. *et al.* Tumor-draining lymph nodes are pivotal in PD-1/PD-L1 checkpoint therapy. *JCI Insight* **3**, 1–7 (2018).

69. Tang, H. *et al.* PD-L1 on host cells is essential for PD-L1 blockade-mediated tumor regression. *J Clin Invest* **128**, 580–588 (2018).

70. Curiel, T. J. *et al.* Blockade of B7-H1 improves myeloid dendritic cell-mediated antitumor immunity. *Nat. Med.* **9**, 562–567 (2003).

71. McAllister, S. S. & Weinberg, R. A. The tumour-induced systemic environment as a critical regulator of cancer progression and metastasis. *Nat. Cell Biol.* **16**, 717–727 (2014).

72. Zhang, S. *et al.* The Role of Myeloid-Derived Suppressor Cells in Patients with Solid Tumors: A Meta-Analysis. *PLoS One* **11**, e0164514 (2016).

73. Barnstorf, I. *et al.* Chronic virus infection compromises memory bystander T cell function in an IL-6/ STAT1-dependent manner. *J. Exp. Med* **216**, 571–586 (2019).

74. Snell, L. M. *et al.* CD8 + T Cell Priming in Established Chronic Viral Infection Preferentially Directs Differentiation of Memory-like Cells for Sustained Immunity. *Immunity* **49**, (2018).

75. Osborne, L. C. *et al.* Virus-helminth coinfection reveals a microbiota-independent mechanism of immunomodulation. *Science (80-.).* **345**, 578–582 (2014).

76. Danna, E. A. *et al.* Surgical Removal of Primary Tumor Reverses Tumor-Induced Immunosuppression Despite the Presence of Metastatic Disease. *Cancer Res.* **64**, 2205–2211 (2004).

77. Ghochikyan, A. *et al.* Primary 4T1 tumor resection provides critical “window of opportunity” for immunotherapy. *Clin Exp Metastasis* **31**, 185–198 (2014).

78. Mosely, S. I. S. *et al.* Rational Selection of Syngeneic Preclinical Tumor Models for Immunotherapeutic Drug Discovery. *Cancer Immunol Res* **5**, 29–41 (2017).

79. Westcott, P. M. K. *et al.* The mutational landscapes of genetic and chemical models of

Kras-driven lung cancer. *Nature* **517**, 489–492 (2015).

80. Zeitouni, B. *et al.* Abstract 1840: Whole-exome somatic mutation analysis of mouse cancer models and implications for preclinical immunomodulatory drug development. in *Proceedings of the 107th Annual Meeting of the American Association for Cancer Research* (2017). doi:10.1158/1538-7445.AM2017-1840.

81. Heinzel, F. P., Sadick, M. D., Holaday, B. J., Coffman, R. L. & Locksley, R. M. Reciprocal expression of interferon gamma or interleukin 4 during the resolution or progression of murine leishmaniasis. Evidence for expansion of distinct helper T cell subsets. *J. Exp. Med.* **169**, 59–72 (1989).

82. Kather, J. N. *et al.* Topography of cancer-associated immune cells in human solid tumors. *Elife* **7**, (2018).

83. Spitzer, M. H. *et al.* An interactive reference framework for modeling a dynamic immune system. *Science (80-.).* **349**, 1259425 (2015).

84. Anz, D. *et al.* CD103 is a hallmark of tumor-infiltrating regulatory T cells. *Int. J. Cancer* **129**, 2417–2426 (2011).

85. Ross, E. A. *et al.* CD31 is required on CD4 + T cells to promote T cell survival during Salmonella infection. *J. Immunol.* **187**, 1553–1565 (2011).

86. Hänninen, A., Maksimow, M., Alam, C., Morgan, D. J. & Jalkanen, S. Ly6C supports preferential homing of central memory CD8+ T cells into lymph nodes. *Eur. J. Immunol.* **41**, 634–644 (2011).

87. Fourcade, J. *et al.* Upregulation of Tim-3 and PD-1 expression is associated with tumor antigen–specific CD8+ T cell dysfunction in melanoma patients. *J. Exp. Med.* **207**, 2175–2186 (2010).

88. Mita, Y. *et al.* Crucial role of CD69 in anti-tumor immunity through regulating the exhaustion of tumor-infiltrating T cells. *Int. Immunol.* **30**, 559–567 (2018).

89. Sun, C., Mezzadra, R. & Schumacher, T. N. Regulation and Function of the PD-L1 Checkpoint. *Immunity* **48**, 434–452 (2018).

90. Bianchini, M. *et al.* PD-L1 expression on nonclassical monocytes reveals their origin and immunoregulatory function. *Sci. Immunol.* **4**, eaar3054 (2019).

91. Busch, D. H., Pilip, I. M., Vijh, S. & Pamer, E. G. Coordinate regulation of complex T cell populations responding to bacterial infection. *Immunity* **8**, 353–362 (1998).

92. Kaech, S. M. & Ahmed, R. Memory CD8 + T cell differentiation: initial antigen encounter triggers a developmental program in naïve cells. *Nat. Immunol.* **2**, 415–422 (2001).

93. Herndler-Brandstetter, D. *et al.* KLRG1+ Effector CD8+ T Cells Lose KLRG1, Differentiate into All Memory T Cell Lineages, and Convey Enhanced Protective Immunity. *Immunity* **48**, 716–729 (2018).

94. Jung, S. *et al.* In vivo depletion of CD11c+ dendritic cells abrogates priming of CD8+ T cells by exogenous cell-associated antigens. *Immunity* **17**, 211–220 (2002).

95. Gabrilovich, D. I., Corak, J., Ciernik, I. F., Kavanaugh, D. & Carbone, D. P. Decreased antigen presentation by dendritic cells in patients with breast cancer. *Clin. Cancer Res.* **3**, 483–490 (1997).

96. Coffelt, S. B. *et al.* IL-17-producing γδ T cells and neutrophils conspire to promote breast cancer metastasis. *Nature* **522**, 345–8 (2015).

97. Wu, W.-C. *et al.* Circulating hematopoietic stem and progenitor cells are myeloid-biased in cancer patients. *Proc. Natl. Acad. Sci.* **111**, 4221–4226 (2014).

98. Apte, R. N. *et al.* Effects of micro-environment- and malignant cell-derived interleukin-1

in carcinogenesis, tumour invasiveness and tumour-host interactions. *Eur. J. Cancer* **42**, 751–759 (2006).

99. Wu, T. C. *et al.* IL1 receptor antagonist controls transcriptional signature of inflammation in patients with metastatic breast cancer. *Cancer Res.* **78**, 5243–5258 (2018).

100. Singer, C. F. *et al.* Interleukin-1alpha protein secretion in breast cancer is associated with poor differentiation and estrogen receptor alpha negativity. *Int. J. Gynecol. Cancer* **16**, 556–559 (2006).

101. Pickup, M., Novitskiy, S. & Moses, H. L. The roles of TGFβ in the tumour microenvironment. *Nat. Rev. Cancer* **13**, 788–799 (2013).

102. Mariathasan, S. *et al.* TGFβ attenuates tumour response to PD-L1 blockade by contributing to exclusion of T cells. *Nature* **554**, 544–548 (2018).

103. Suzuki, A. *et al.* IL-1 production as a regulator of G-CSF and IL-6 production in CSF-producing cell lines. *Br. J. Cancer* **65**, 515–518 (1992).

104. Mittal, R., Wagener, M., Breed, E. R., Liang, Z. & Yoseph, B. P. Phenotypic T Cell Exhaustion in a Murine Model of Bacterial Infection in the Setting of Pre-Existing Malignancy. *PLoS One* **9**, 93523 (2014).

105. Xie, J. *et al.* Pre-existing malignancy results in increased prevalence of distinct populations of CD4+ T cells during sepsis. *PLoS One* **13**, e0191065 (2018).

106. Russ, A. J. *et al.* Melanoma-induced suppression of tumor antigen-specific T cell expansion is comparable to suppression of global T cell expansion. *Cell. Immunol.* **271**, 104–109 (2011).

107. Klastersky, J. & Aoun, M. Opportunistic infections in patients with cancer. *Ann. Oncol.* **15**, iv329–iv335 (2004).

108. Baluch, A. & Pasikhova, Y. Influenza Vaccination in Oncology Patients. *Curr Infect Dis Rep* **15**, 486–490 (2013).

109. Zuckerman, N. S. *et al.* Altered local and systemic immune profiles underlie lymph node metastasis in breast cancer patients. *Int. J. Cancer* **132**, 2537–2547 (2012).

110. Wang, L. *et al.* Connecting blood and intratumoral Treg cell activity in predicting future relapse in breast cancer. *Nat. Immunol.* **20**, 1220–1230 (2019).

111. Kosaka, A., Ohkuri, T., Program, B. T. & Okada, H. Combination of an agonistic anti-CD40 monoclonal antibody and the COX-2 inhibitor celecoxib induces anti-glioma effects by promotion of type-1 immunity in myeloid cells and T-cells. *Cancer Immunol Immunother* **63**, 847–857 (2014).

112. Tseng, W. W. *et al.* Development of an orthotopic model of invasive pancreatic cancer in an immunocompetent murine host. *Clin. Cancer Res.* **16**, 3684–3695 (2010).

113. Kathryn E. Foulds, Lauren A. Zenewicz, Devon J. Shedlock, J. J. & Amy E. Troy, and H. S. Cutting Edge: CD4 and CD8 T Cells Are Intrinsically Different in Their Proliferative Responses. *J Immunol* **168**, 1528–1532 (2002).

114. Zunder, E. R. *et al.* Palladium-based Mass-Tag Cell Barcoding with a Doublet-Filtering Scheme and Single Cell Deconvolution Algorithm. *Nat. Protoc.* **10**, 316–333 (2015).

115. Finck, R. *et al.* Normalization of mass cytometry data with bead standards. *Cytom. Part A* **83 A**, 483–494 (2013).

116. Bair, E. & Tibshirani, R. Semi-Supervised Methods to Predict Patient Survival from Gene Expression Data. *PLoS Biol.* **2**, 0511–0522 (2004).

117. Dumeaux, V. *et al.* Interactions between the tumor and the blood systemic response of breast cancer patients. *PLoS Comput. Biol.* **13**, (2017).

118. Aran, D., Hu, Z. & Butte, A. J. xCell: digitally portraying the tissue cellular heterogeneity landscape. *Genome Biol.* **18**, 1–14 (2017).

119. Thorsson, V. *et al.* The Immune Landscape of Cancer. *Immunity* **48**, 812-830.e14 (2018).

120. Ik Sun Kim, Yang Gao, Thomas Welte, Hai Wang, Jun Liu, Mahnaz Janghorban, Kuanwei Sheng, Y. N., Amit Goldstein, Na Zhao, Igor Bado, Hin-Ching Lo, Michael J. Toneff, Tuan Nguyen, Wen Bu, W. J., James Arnold, Franklin Gu, Jian He, Deborah Jebakumar, Kimberly Walker, Yi Li, Qianxing Mo, T. F. & Westbrook, Chenghang Zong, Arundhati Rao, Arun Sreekumar, Jeffrey M. Rosen, X. H.-F. Z. Immuno-subtyping of breast cancer reveals distinct myeloid cell biology and immunotherapy resistance mechanisms. *Nat. Cell Biol.* **In press**, (2019).

121. Binnewies, M. *et al.* Understanding the tumor immune microenvironment (TIME) for effective therapy. *Nat. Med.* **24**, 541–550 (2018).

122. Chen, D. S. & Mellman, I. Elements of cancer immunity and the cancer-immune set point. *Nature* vol. 541 (2017).

123. Melero, I., Rouzaut, A., Motz, G. T. & Coukos, G. T-cell and NK-cell infiltration into solid tumors: A key limiting factor for efficacious cancer immunotherapy. *Cancer Discov.* **4**, 522–526 (2014).

124. Teng, M. W. L., Ngiow, S. F., Ribas, A. & Smyth, M. J. Classifying cancers based on T-cell infiltration and PD-L1. *Cancer Res.* **75**, 2139–2145 (2015).

125. Davis, A. A. & Patel, V. G. The role of PD-L1 expression as a predictive biomarker: An analysis of all US food and drug administration (FDA) approvals of immune checkpoint inhibitors. *J. Immunother. Cancer* **7**, 278 (2019).

126. Xu, Y. *et al.* The association of PD-L1 expression with the efficacy of anti-PD-1/PD-L1

immunotherapy and survival of non-small cell lung cancer patients: A meta-analysis of randomized controlled trials. *Transl. Lung Cancer Res.* **8**, 413–428 (2019).

127. Gubin, M. M. *et al.* High-Dimensional Analysis Delineates Myeloid and Lymphoid Compartment Remodeling during Successful Immune-Checkpoint Cancer Therapy. *Cell* **175**, 1–17 (2018).

128. Schietinger, A. *et al.* Tumor-Specific T Cell Dysfunction Is a Dynamic Antigen-Driven Differentiation Program Initiated Early during Tumorigenesis. *Immunity* **45**, 389–401 (2016).

129. Hogan, S. A. *et al.* Peripheral blood TCR repertoire profiling may facilitate patient stratification for immunotherapy against melanoma. *Cancer Immunol. Res.* **7**, 77–85 (2019).

130. Nabet, B. Y. *et al.* Noninvasive Early Identification of Therapeutic Benefit from Immune Checkpoint Inhibition. *Cell* **0**, (2020).

131. Li, Z. *et al.* Predictive value of postoperative peripheral CD4+ T cells percentage in stage I–III colorectal cancer: A retrospective multicenter cohort study of 1028 subjects. *Cancer Manag. Res.* **12**, 5505–5513 (2020).

132. Allen, B. M. *et al.* Systemic dysfunction and plasticity of the immune macroenvironment in cancer models. *Nat. Med.* **26**, 1125–1134 (2020).

133. Wang, L. *et al.* Breast cancer induces systemic immune changes on cytokine signaling in peripheral blood monocytes and lymphocytes. *EBioMedicine* **52**, 102631 (2020).

134. Lau, J. *et al.* Tumour and host cell PD-L1 is required to mediate suppression of anti-tumour immunity in mice. *Nat. Commun.* **8**, 14572 (2017).

135. Helmink, B. A. *et al.* B cells and tertiary lymphoid structures promote immunotherapy

response. *Nature* **577**, 549–555 (2020).

136. Haeryfar, S. M. M. & Hoskin, D. W. Thy-1: More than a Mouse Pan-T Cell Marker. *J. Immunol.* **173**, 3581–3588 (2004).

137. Vonderheide, R. H. The Immune Revolution: A Case for Priming, Not Checkpoint. *Cancer Cell* **33**, 563–569 (2018).

138. Headley, M. B. *et al.* Visualization of immediate immune responses to pioneer metastatic cells in the lung. (2016) doi:10.1038/nature16985.

139. Ruhland, M. K. *et al.* Visualizing Synaptic Transfer of Tumor Antigens among Dendritic Cells. *Cancer Cell* **37**, 786-799.e5 (2020).

140. Popovic, A., Jaffee, E. M. & Zaidi, N. Emerging strategies for combination checkpoint modulators in cancer immunotherapy. *Journal of Clinical Investigation* vol. 128 3209–3218 (2018).

141. Nakhoda, S. K. & Olszanski, A. J. Addressing Recent Failures in Immuno-Oncology Trials to Guide Novel Immunotherapeutic Treatment Strategies. *Pharmaceut. Med.* **34**, 83–91 (2020).

142. Pai, C. C. S. *et al.* Clonal Deletion of Tumor-Specific T Cells by Interferon-γ Confers Therapeutic Resistance to Combination Immune Checkpoint Blockade. *Immunity* **50**, 477-492.e8 (2019).

143. Katsurada, M. *et al.* Baseline tumor size as a predictive and prognostic factor of immune checkpoint inhibitor therapy for non-small cell lung cancer. *Anticancer Res.* **39**, 815–825 (2019).

144. Hanna, R. N. *et al.* Patrolling monocytes control tumor metastasis to the lung. *Science (80-.).* **350**, 985–990 (2015).

145. Hendriks, J., Xiao, Y. & Borst, J. CD27 Promotes Survival of Activated T Cells and Complements CD28 in Generation and Establishment of the Effector T Cell Pool. *J. Exp. Med.* **198**, 1369–1380 (2003).

146. Kaech, S. M. *et al.* Selective expression of the interleukin 7 receptor identifies effector CD8 T cells that give rise to long-lived memory cells. *Nat. Immunol.* **4**, 1191–1198 (2003).

147. Hendriks, J. *et al.* CD27 is required for generation and long-term maintenance of T cell immunity. *Nat. Immunol.* **1**, 433–440 (2000).

148. Paiardini, M. *et al.* Loss of CD127 Expression Defines an Expansion of Effector CD8 + T Cells in HIV-Infected Individuals . *J. Immunol.* **174**, 2900–2909 (2005).

149. Ahrends, T. *et al.* CD27 Agonism Plus PD-1 Blockade Recapitulates CD4+ T-cell Help in Therapeutic Anticancer Vaccination. *Cancer Res.* **76**, 2921–2931 (2016).

150. Hegde, S. *et al.* Dendritic Cell Paucity Leads to Dysfunctional Immune Surveillance in Pancreatic Cancer. *Cancer Cell* **37**, 289-307.e9 (2020).

Publishing Agreement

It is the policy of the University to encourage open access and broad distribution of all theses, dissertations, and manuscripts. The Graduate Division will facilitate the distribution of UCSF theses, dissertations, and manuscripts to the UCSF Library for open access and distribution. UCSF will make such theses, dissertations, and manuscripts accessible to the public and will take reasonable steps to preserve these works in perpetuity.

I hereby grant the non-exclusive, perpetual right to The Regents of the University of California to reproduce, publicly display, distribute, preserve, and publish copies of my thesis, dissertation, or manuscript in any form or media, now existing or later derived, including access online for teaching, research, and public service purposes.

DocuSigned by:

7412D3D922FF4DC...

Author Signature

12/8/2020

Date